Stress-Dependent Elastic Properties of Anisotropic Sedimentary Rocks: Uniaxial and Triaxial Experiments and Theoretical Modelling

Dissertation
zur Erlangung des Doktorgrades der Naturwissenschaften
im Fachbereich Geowissenschaften
Institut für Geologische Wissenschaften
Fachrichtung Geophysik
der Freien Universität Berlin

vorgelegt von

Viacheslav A. Sviridov

Berlin
2018

Ich erkläre hiermit an Eides statt, dass ich die vorliegende Dissertation selbstständig und nur unter Verwendung der angegebenen Quellen und Hilfsmittel angefertigt habe.

Berlin,

Gutachter:	Prof. Dr. Serge A. Shapiro PD Dr. Sibylle Mayr
Tag der Abgabe:	11.09.2018
Tag der Disputation:	29.11.2018

Summary

Shale is a complex medium composed of clay, other mineral phases and pore space. The combined elastic properties of these components control the effective (anisotropic) properties of the composite solid. Deformation of the compliant porosity (e.g. micro-cracks, joints, grain boundary domains, faults) impacts the relationship between effective stress and rock elasticity. This leads to nonlinear stress dependency of seismic velocities and seismic anisotropy. Such phenomenon is often observed for brittle and semi-brittle rocks like shales or other siliciclastic sediments. Description and understanding of this relationship is important for any time-lapse geophysical or geo-hazard modelling.

This thesis presents the experimental measurements and the theoretical modelling of the stress-dependent elasticity. Such a combination enables a direct comparison and validation of the theoretical approach. The porosity deformation approach is used for a physical interpretation of the stress-dependent seismic velocities. The main objective of this thesis was to validate the applicability of the theoretical approach on the experimentally obtained data. This includes analysis of the special role of the compliant porosity and its influence on the stress-dependent elasticity. For this purpose were studied various shale samples under uniaxial and triaxial stress conditions. Two of the studied samples were saturated and measured under drained loading conditions. The samples have either vertical transverse isotropy or initial horizontal transverse isotropy, and one of the samples was initially orthorhombic. These samples were loaded and their elastic properties were measured during the loading. The strain gauges measured the deformation and the piezoelements simultaneously measured the ultrasonic velocities. Thirteen conducted experiments provide a comprehensive data bank of the elastic parameters. The value of this data bank is enhanced by the mineralogical description of studied samples, including the thin section analysis and the density measurements.

The first part of the thesis introduces the theoretical background and the theoretical approaches, which were applied in the frame of this work. The second part of the thesis includes experiments under the uniaxial loading conditions and application of the theory on the obtained data sets. In this part were studied four anisotropic samples. Finally, the third part presents results of experiments under the triaxial loading conditions and an example of the application of the theory on the obtained data set. Five triaxially loaded samples include dry and saturated rocks with different initial anisotropy.

The interpretation and analysis of the laboratory measurements initiated development of additional theoretical approaches. One of them is the constant anellipticity approach and it is used for the estimation of the off-axis (under an inclination to the symmetry axis) velocity depending on the stress. Another approach is called: "orthorhombic anisotropy due to an imperfect disorder" and it is a qualitative explanation of the orthorhombic stiffness tensor observed for a visually

layered sample. Application of these approaches completed the experimentally obtained data sets.

The collection of the experimental data bank with contribution of the theoretical estimations made possible application of the porosity deformation approach. This approach formulates stress-dependence of the velocities via stress-induced deformation of the pore space. The closure of the compliant (crack-like) porosity impacts the stress sensitivity of the velocities, and the shape of this stress-dependence is nonlinear. Hereby, the physical non-linearity is assumed to be controlled by the compliant pore space deformation and the geometrical non-linearity is considered to be negligible. The key parameters within the theory are the porosity tensor and the tensor of stress sensitivity. The former is anisotropic and the latter is assumed to be isotropic (according to the latest extension of the theory).

In the frame of this study, the theoretical modelling validates the applicability of the porosity deformation approach, and developed further understanding of the key parameters, their influence on the stress-dependency and their mutual relations. It was shown, that the uniaxial stress changes the anisotropy, but does not impact the anellipticity parameter. The study demonstrates the distinct influence of stiff and compliant porosities on the stress-sensitivity of the elastic properties. Particularly, the modelling of the uniaxial experiments validate the different deformation mechanisms for the stiff and compliant porosities, depending on the direction of the stress application. The modelling of the triaxial data set approved universality of proposed theoretical description and provides an opportunity for a prediction of the stress-dependent elasticity.

Zusammenfassung

Shale ist ein komplexes Medium, es besteht aus dem Ton- und anderen Mineralen und aus dem Porenraum. Kombinierte elastische Eigenschaften von diesen Komponenten definieren die effektive (anisotropische) Eigenschaften des Kompositums. Deformation der nachgiebigen (compliant) Porosität (z. B. Mikrorisse, Korn-Korn Kontakten, Bruchstellen) beeinflusst den Zusammenhang zwischen dem effektiven Stress und der Gesteinselastizität. Dies führt zur nichtlinearer Stress-Abhängigkeit der seismischen Geschwindigkeit und Anisotropie. Solche Phänomene sind öfter beobachtet für brittle und semi-brittle Gesteine, wie Shales oder andere Siliziklastische Sedimente. Beschreibung und Verständnis von diesen Abhängigkeiten ist wichtig für 4-D geophysikalische Modellierungen.

Diese Dissertation präsentiert experimentelle Messungen und theoretische Modellierungen der stressabhängigen Elastizität. Diese Kombination ermöglicht einen direkten Vergleich und die Validierung des theoretischen Ansatzes. Der Porositätsdeformationsansatz (porosity deformation approach) ist anwendbar für die physikalische Interpretation der spannungsabhängigen seismischen Geschwindigkeiten. Das Hauptziel dieser Dissertation, ist die Anwendbarkeit des theoretischen Ansatzes auf die experimentellen Daten zu validieren. Dieses beinhaltet die Analyse der speziellen Rolle der nachgiebigen (compliant) Porosität und ihren Einfluss auf die stressabhängige Elastizität. Für diesen Zweck wurden unterschiedliche Proben unter uniaxialer oder triaxialer Belastung studiert. Zwei Proben waren gesättigt und wurden unter drainierten Bedingungen gemessen. Acht gemessene Proben hatten entweder vertikale transversale Isotropie oder horizontale transversale Isotropie, und eine Probe hatte ursprünglich orthorhombische Symmetrie. Diese Proben wurden belastet und ihre elastischen Eigenschaften wurden während der Belastung gemessen. Die Deformation wurde mithilfe von Dehnungsmessstreifen gemessen und die Ultraschallgeschwindigkeiten wurden gleichzeitig mit Piezoelementen bestimmt. Dreizehn durchgeführte Experimente setzen eine signifikante Datenbank zusammen. Die mineralogische Beschreibung der studierten Proben zusammen mit Dünnschliffanalyse und Dichtbestimmung, vervollständigen diese Datenbank.

Der erste Teil der Dissertation führt den theoretischen Hintergrund und theoretische Anwendungen ein, die in Rahmen dieser Arbeit angewendet wurden. Der zweite Teil der Dissertation beinhaltet die Experimente unter den uniaxialen Druckbedingungen und die Anwendung der Theorie auf den gewonnenen Datenbank. In diesem Teil wurden vier anisotrope Proben untersucht. Anschließend, der dritte Teil präsentiert die Experimente unter den triaxialen Druckbedingungen und die Beispiele der Anwendung der theoretischen Ansätze auf die triaxiale Daten. Fünf triaxial belastete Proben beinhalten trockene und gesättigte Gesteine mit unterschiedlichen Anisotropien.

Die Interpretation und die Analyse der Labordaten hat die Entwicklung der zusätzlichen

theoretische Ansätzen initiiert. Der „Konstant Anelliptizität“ Ansatz (constant anellipticity approach) ist für die Abschätzung der geneigten (unter dem Winkel zur Symmetrieachse) spannungsabhängigen Geschwindigkeiten geeignet. Ein anderer Ansatz heißt: „orthorhombische Anisotropie infolge einer imperfekten Fehlordnung“ und ist eine qualitative Erklärung der orthorhombischen Steifigkeits-Tensor (stiffness tensor) in einer visuell geschichteten Probe. Die Anwendung dieser Ansätze ist zur Ergänzung der experimentellen Datenbanken geeignet.

Die Zusammenfassung der experimentellen Daten und der theoretischen Abschätzung ermöglicht die Anwendung des Porositätsdeformationsansatzes (porosity deformation approach). Dieser Ansatz formuliert die Stressabhängigkeit der Ultraschallgeschwindigkeiten über die stresserzeugte Deformation des Porenraumes. Die Schließung des nachgiebigen (compliant, crack-like) Porenraumes beeinflusst die Stresssensitivität der Geschwindigkeiten am meisten, und die entsprechende Abhängigkeit ist nichtlinear. Darüber hinaus wird die physikalische Nichtlinearität als eine Funktion der Deformation des Porenraumes angenommen, und die geometrische Nichtlinearität ist vernachlässigbar. Die Schlüsselparameter der Theorie sind der Porositätstensor (porosity tensor) und der Stresssensitivitätstensor (stress-sensitivity tensor). Der erste ist anisotrop und der zweite wird als isotrop angenommen (entsprechend der aktuelle Theorie).

In Rahmen dieser Arbeit, die theoretische Modellierungen haben die Anwendbarkeit des Porositätsdeformationsansatzes (porosity deformation approach) validiert, und das weitere Verständnis der Schlüsselparameter, deren Einfluss auf die Stressabhängigkeit und deren Zusammenhang entwickelt. Es wurde gezeigt, dass die uniaxiale Spannung verändert die Anisotropie, aber verändert nicht den Anelliptizität Parameter. Die Arbeit demonstriert den separaten Einfluss der stiffen und nachgiebigen (compliant) Porositäten auf die Stress-Sensitivität der elastischen Eigenschaften. Zum Beispiel, die Modellierung der uniaxialen Experimenten validiert die unterschiedliche Mechanismen für die stiffen und nachgibiegen (compliant) Porositäten, in der Abhängigkeit von der Belastungsrichtung. Die Modellierung der triaxialen Daten hat die Universalität der theoretischen Beschreibung gezeigt und hat die Möglichkeit der spannungsabhängigen Elastizitätsvorhersage vermutet.

Contents

Part I

Introduction and theory

Chapter 1

Introduction

Seismic exploration and borehole drilling are often dealing with significant depths. One of the key factors essential for the subsurface medium is the overburden pressure. Configuration of the stress distribution can significantly vary depending on lithology, anisotropy, tectonic processes, temperature, pore pressure, and other factors. Understanding of the stress field distribution and the ability to measure, to model and maybe to predict it would be a great benefit for many engineering branches. Even though the stress field is known, its influence on the mechanical properties of the elastic medium is not trivial. In the oil and gas industry, sediment rocks and their elastic properties play a special role.

Shales are the most common rocks found in sedimentary basins (e.g., Jones and Wang, 1981) and they overlie most hydrocarbon bearing reservoirs. Shales are complex material, normally consisting of aligned minerals and the pore space filled with gas or fluids. The ambient stress field influences the shape, orientation and volumetric relation of these phases. As a result of their formation, the elastic properties of shales are anisotropic (e.g., Winterstein and Paulsson, 1990) and this inherent anisotropy must be taken into account by any kind of seismic imaging. Elastic parameters of shales are stress-dependent and this phenomenon is important for any time-lapse geophysical or geo-hazard modelling (e.g., Eaton et al., 1975; Landrø et al., 2001; Gurevich, 2004; Calvert, 2005; Sayers, 2006; Verdon et al., 2008; Herwanger and Horne, 2009; Asaka et al., 2016).

The exposure of stress on porous sedimentary rocks causes alteration of the elastic constants, such as stiffnesses or seismic velocities. Stress dependency has a non-linear form and is greatly influenced by the deformation of pore space. Pore space can be classified in to two groups, with different properties: stiff porosity and compliant porosity. Compliant porosity (e.g. microcracks, joints, grain boundary domains, faults) substantially influences the relationship between effective stress and rock elasticity (e.g., Walsh, 1965a,b). This leads to the non-linear stress dependency of seismic velocities and seismic anisotropy. This phenomenon is often observed for shales or other siliciclastic sediments.

Experimental measurements of stress-dependent seismic velocities are published in many studies (e.g., Vernik and Nur, 1992; Vernik and Liu, 1997; Hornby, 1998; Wang, 2002a,b; Dewhurst and Siggins, 2006; Sarout et al., 2007, 2015; Mayr et al., 2016; Sviridov et al., 2017). An empirical law which describes the stress dependency of seismic velocities was established based on the experimentally obtained, see (e.g., Prasad and Manghnani, 1997; Eberhart-Phillips et al.,

1989; Freund, 1992; Carcione and Tinivella, 2001):

$$v(P_{eff}) = A + C \cdot P_{eff} - D \cdot exp(-F \cdot P_{eff}), \tag{1.1}$$

where v is the seismic velocity, P_{eff} is the effective pressure (difference between confining pressure and pore pressure) and coefficients A, C, D, F are empirical fitting parameters depending on the physical properties of the rock.

The third order nonlinear elasticity theory proposes representation of the strain energy density E in a general anisotropic medium by (Brugger, 1964; Norris et al., 1994):

$$E = \frac{1}{2} C_{ijpq} \epsilon_{ij} \epsilon_{pq} + \frac{1}{6} C_{ijpqtm} \epsilon_{ij} \epsilon_{pq} \epsilon_{tm}, \tag{1.2}$$

where the higher-order terms in the Taylor expansion are neglected. C_{ijpq} and C_{ijpqtm} designate the components of the second-order (linear) and the third-order (nonlinear) elastic moduli, respectively. The order of an elastic constant corresponds to the power of the corresponding strain tensor components in the development of the elastic strain energy density. For further details see Truesdell (1965); Green (1973); Landau and Lifshitz (1987).

Various rock-physics models relate seismic velocities to the change of stress conditions and to the strain. A number of theoretical works have been dedicated to this effect (e.g., Mavko et al., 1995; Sayers, 1999; Winkler and McGowan, 2004; Gurevich et al., 2011; Pervukhina et al., 2011; Rasolofosaon, 2011; David and Zimmerman, 2012; Collet et al., 2014; Pride et al., 2017). One of the informative parameters for the analysis of anisotropy is the so called anellipticity (e.g., Alkhalifah and Tsvankin, 1995), which to some extent describes alteration of the off-axis velocities. Stress dependency of anellipticity was discussed for example in Prioul et al. (2004). Rasolofosaon (2011) proposes a unified phenomenological model for the mechanical behaviour of rocks, accounting for: the porous nature of rocks, Preisach nonlinear hysteretic operator (Preisach, 1935; Helbig and Rasolofosaon, 2001; Heslop et al., 2004), viscoelastic operator and anisotropy. The large number of described mechanisms is a strength of the phenomenological approach. However, at some point, the various contributions of the many physical mechanisms are summed up, making separate components difficult to distinguish from each other. The formulation of Shapiro and Kaselow (2005) proposes a theoretically based description of the stress-dependent rock elasticity in the framework of orthorhombic stiffnesses, the so-called porosity deformation approach. Recently, Shapiro (2017) expanded this description for any kind of seismically anisotropic medium in the absence of any information about the orientation or the spatial distribution of micro-cracks.

This dissertation extends our knowledge of the stress-dependent rock elasticity. The siliciclastic sedimentary rocks were particularly studied, since they are especially interesting for the seismic exploration and monitoring. The topic of the stress-dependent elasticity was decomposed in one theoretical part and two experimental parts. The theoretical background, description of used theoretical approaches and some theoretical considerations are introduced in the Part I. Experimental measurements under uniaxial loading and application of the porosity deformation approach are described in the Part II. Experimental measurements under triaxial loading and their interpretation are presented in the Part III. Total number of the studied samples equals nine. The samples have either vertical transverse isotropy or orthorhombic symmetry. The samples were loaded uniaxially or triaxially and simultaneously measured using the ultrasonic transducers and the strain gauges. Total number of the experiments equals thirteen. Obtained laboratory data

was used for the application of the porosity deformation approach and further interpretation. Due to the large data set, each experiment has an intermediate section of the discussion and the conclusions. The complete study is summarized using the general conclusions.

Chapter 2

Theory

2.1 Elastic medium

An external or internal force applied to a continuum influences its every point. Generally, external forces deform the medium resulting in change of size and shape. Internal forces, acting within the medium, resist to this deformation. When external forces are removed, the medium returns to its initial shape. If the recovered shape and volume are the same as in an initial state, then the medium is called elastic.
The Hooke's Law is the constitutive law describing the dependency of deformation on the stress. The state of the stress at an arbitrary point of the continuum depends on the orientation of the acting force. For evaluation of the stress state, the arbitrary point is imagined as an infinitesimal cube. The stress acting on each of the six sides of the cube can be resolved into the normal to the cube's face components and the within the cube's face components. A stress σ_{ij} is defined as acting on the i-plane and being oriented in the j direction. Components of the stress tensor with repeating indices, e.g., σ_{33}, are called the normal stress and the components with non-repeating indices are called the shear stress. This produces six shear and three normal stress components acting on the cube. The medium in the static equilibrium has the sum of all stress components and the total moment equal to zero. It means $\sigma_{ij} = \sigma_{ji}$. The stress tensor σ_{ij} completely describes the state of stress at any point of the continuum.

$$\sigma_{ij} = \begin{pmatrix} \sigma_{11} & \sigma_{12} & \sigma_{13} \\ \sigma_{21} & \sigma_{22} & \sigma_{23} \\ \sigma_{31} & \sigma_{32} & \sigma_{33} \end{pmatrix}, \tag{2.1}$$

with i, j = 1, 2, 3. The normal stresses directed outward from the cube's faces are called the tensional stress and are defined as a positive stress. While, the compressional stress is defined as a negative stress. According to the International System of Units (SI) stress is measured in Pascal (Pa), and a frequently used MegaPascal (MPa) is equal to one million Pascal.

In the experimental rock-physics is often used the so called hydrostatic or isostatic loading. In this stress state all normal stresses are equal to each other, i.e., $\sigma_{11} = \sigma_{22} = \sigma_{33}$ and all shear stresses are equal to zero. In this case, the stress tensor is independent of the reference coordinate system, and the stress can be considered as a scalar value, or as a pressure. This pressure is defined as P = $-\sigma_{ii}$. The term hydrostatic pressure comes from the similarity to the pressure in a fluid and to the loading technique, which is realized using the hydraulic equipment.

An elastic body under the stress changes its size and shape and these deformations are called the strain. The strain is defined as a relative (fractional) change of a dimension of a body. In the three dimensional space the strain at any random point is defined by the strain tensor ϵ_{ij}, assuming the deformations being small:

$$\epsilon_{ij} = \begin{pmatrix} \epsilon_{11} & \epsilon_{12} & \epsilon_{13} \\ \epsilon_{21} & \epsilon_{22} & \epsilon_{23} \\ \epsilon_{31} & \epsilon_{32} & \epsilon_{33} \end{pmatrix}, \tag{2.2}$$

with i, j = 1, 2, 3. The elements of the tensor with repeating indices are defined as the normal strain and the others as the shear strain. Like the stress tensor, the strain tensor has six independent components: $\epsilon_{ij} = \epsilon_{ji}$. The change of the volume is defined by the diagonal elements ϵ_{ii}.

The Hooke's Law relates the strain and the stress to each other. It is assumed that the relation has a linear form, and the corresponding medium is called a linearly elastic medium. The general form of Hook's Law is as follows:

$$\sigma_{ij} = C_{ijkl}\epsilon_{kl}, \tag{2.3}$$

with i, j, k, l = 1, 2, 3. The fourth rank tensor C_{ijkl} is called the stiffness tensor and has 81 terms. This tensor represents all elastic constants of the medium and links the deformation of the medium to the applied stress. Each component of the stress tensor σ_{ij} is linearly dependent on the every component of the strain tensor ϵ_{kl} and vice versa. This results in the nine relations, where each relation has one component of the stress and nine components of the strain. Due to the fact that the stress tensor is symmetrical, only six of the equations are independent. The same is valid for the strain. For certain problems it is more convenient to express the strain as a linear combination of the stresses:

$$\epsilon_{ij} = \sum_{k=1}^{3}\sum_{l=1}^{3} S_{ijkl}\sigma_{kl}, \tag{2.4}$$

with i, j, k, l = 1, 2, 3. Here, the S_{ijkl} denotes the compliance tensor. The tensor of elastic compliances is then deduced by explicit inversion of the stiffness tensor expressed with respect to all three sets of base tensors:

$$C_{ijkl}S_{klmn} = I_{ijmn}, \tag{2.5}$$

For the sake of simplicity, the stiffness tensor C_{ijkl}, which is a 3 x 3 x 3 x 3 tensor is often displayed using the so called Voigt notation. In this case the stiffness tensor is represented by a 6 x 6 stiffness matrix C_{IJ}. Voigt notation proposes that each pair of indices ij(kl) is replaced by just one index I(J):

ij(kl)	I(J)
11	1
22	2
33	3
23,32	4
13,31	5
12,21	6

Table 2.1: *Voigt notation: indices replacement (Kaselow, 2004).*

The most general form of the stiffness tensor has 81 entries. Due to the symmetry of stress and strain the number of independent terms reduces to 36: $C_{ijkl} = C_{jikl} = C_{ijlk} = C_{jilk}$. An additional restriction comes due to the unique strain energy potential, which requires: $C_{ijkl} = C_{klij}$. Thus, the number of independent terms in the stiffness tensor is equal to 21. This is the most general case and the medium described by 21 independent elastic constants is called the triclinic medium. The intrinsic symmetry of the medium reduces number of the independent stiffnesses in the tensor. The orthorhombic medium can be described by 9 independent constants, the transversely isotropic by 5 independent constants and the isotropic medium by 2 independent constants.

2.2 Anisotropy parameters of the VTI medium

Thomsen's (Thomsen, 1986) and Tsvankin's (Tsvankin, 1996) anisotropy parameters for a VTI medium can be expressed as:

$$
\begin{aligned}
C_{11} &= C_{22} = \rho v_{11}^2 = \rho v_{22}^2 && (2.6)\\
C_{33} &= \rho v_{33}^2 && (2.7)\\
C_{44} &= C_{55} = \rho v_{31}^2 = \rho v_{13}^2 && (2.8)\\
C_{66} &= \rho v_{12}^2 = \rho v_{21}^2 && (2.9)\\
C_{12} &= C_{11} - 2C_{66} && (2.10)\\
& && (2.11)
\end{aligned}
$$

The element C_{13}^{θ} of the stiffness tensor, can be calculated using the qP phase velocity under arbitrary inclination angle $v_q(\theta)$ to the symmetry axis:

$$C_{13}^{\theta} = \sqrt{\pm \frac{(2\rho v_q^2(\theta) - A)^2 \mp B^2}{4sin^2(\theta)cos^2(\theta)}} - C_{44} \quad (2.12)$$

$$A = (C_{11} + C_{44})sin^2(\theta) + (C_{33} + C_{44})cos^2(\theta) \quad (2.13)$$

$$B = (C_{11} - C_{44})sin^2(\theta) - (C_{33} - C_{44})cos^2(\theta), \quad (2.14)$$

where the plus sign in front of the fracture and the minus sign in front of term B correspond to the qP wave,
the minus sign in front of the fracture and the plus sign in front of term B correspond to the qS wave,
$v_q(\theta)$ denotes the off-axis velocity propagated under the angle θ to the symmetry axis.

$$
\begin{aligned}
\varepsilon &= \frac{C_{11} - C_{33}}{2C_{33}} && (2.15)\\
\gamma &= \frac{C_{66} - C_{44}}{2C_{44}} && (2.16)\\
\delta &= \frac{(C_{13} + C_{44})^2 - (C_{33} - C_{44})^2}{2C_{33}(C_{33} - C_{44})} && (2.17)\\
\eta &= \frac{\varepsilon - \delta}{1 + 2\delta} && (2.18)
\end{aligned}
$$

2.3 Anisotropy parameters of the orthorhombic medium

According to (e.g., Tsvankin, 1997) stiffness tensor and the anisotropy parameters of an orthorhombic medium can be calculated using the following equations set:

$$
\begin{aligned}
C_{11} &= \rho v_{11}^2 && (2.19)\\
C_{22} &= \rho v_{22}^2 && (2.20)\\
C_{33} &= \rho v_{33}^2 && (2.21)\\
C_{44} &= \rho v_{32}^2 = \rho v_{23}^2 && (2.22)\\
C_{55} &= \rho v_{13}^2 = \rho v_{31}^2 && (2.23)\\
C_{66} &= \rho v_{12}^2 = \rho v_{21}^2 && (2.24)\\
& && (2.25)
\end{aligned}
$$

The elements of the stiffness tensor C_{13}^{θ}, C_{23}^{θ} and C_{12}^{θ} can be calculated using the qP phase velocities under arbitrary inclination angle to the symmetry axes, $v_{qp44}(\theta)$, $v_{qp55}(\theta)$ and $v_{qp66}(\theta)$:

$$
\begin{aligned}
C_{13}^{\theta} &= \sqrt{\frac{(2\rho v_{qp44}^2(\theta) + A_{13})^2 - (B_{13})^2}{4sin^2(\theta)cos^2(\theta)}} - C_{55} && (2.26)\\
A_{13} &= -(C_{11} + C_{55})\, sin^2(\theta) - (C_{33} + C_{55})\, cos^2(\theta) && (2.27)\\
B_{13} &= (C_{11} - C_{55})\, sin^2(\theta) - (C_{33} - C_{55})\, cos^2(\theta) && (2.28)\\
C_{23}^{\theta} &= \sqrt{\frac{(2\rho v_{qp55}^2(\theta) + A_{23})^2 - (B_{23})^2}{4sin^2(\theta)cos^2(\theta)}} - C_{44} && (2.29)\\
A_{23} &= -(C_{22} + C_{44})\, sin^2(\theta) - (C_{33} + C_{44})\, cos^2(\theta) && (2.30)\\
B_{23} &= (C_{22} - C_{44})\, sin^2(\theta) - (C_{33} - C_{44})\, cos^2(\theta) && (2.31)\\
C_{12}^{\theta} &= \sqrt{\frac{(2\rho v_{qp66}^2(\theta) + A_{12})^2 - (B_{12})^2}{4sin^2(\theta)cos^2(\theta)}} - C_{66} && (2.32)\\
A_{12} &= -(C_{11} + C_{66})\, sin^2(\theta) - (C_{22} + C_{66})\, cos^2(\theta) && (2.33)\\
B_{12} &= (C_{11} - C_{66})\, sin^2(\theta) - (C_{22} - C_{66})\, cos^2(\theta) && (2.34)\\
& && (2.35)
\end{aligned}
$$

$$
\begin{aligned}
\epsilon^1 &= \frac{C_{22} - C_{33}}{2C_{33}} && (2.36)\\
\epsilon^2 &= \frac{C_{11} - C_{33}}{2C_{33}} && (2.37)\\
\gamma^1 &= \frac{C_{66} - C_{55}}{2C_{55}} && (2.38)\\
\gamma^2 &= \frac{C_{66} - C_{44}}{2C_{44}} && (2.39)\\
\delta^1 &= \frac{(C_{23} + C_{44})^2 - (C_{33} - C_{44})^2}{2C_{33}(C_{33} - C_{44})} && (2.40)\\
\delta^2 &= \frac{(C_{13} + C_{55})^2 - (C_{33} - C_{55})^2}{2C_{33}(C_{33} - C_{55})} && (2.41)\\
\delta^3 &= \frac{(C_{12} + C_{66})^2 - (C_{11} - C_{66})^2}{2C_{11}(C_{11} - C_{66})} && (2.42)\\
& && (2.43)
\end{aligned}
$$

$$\eta^1 = \frac{\varepsilon^{(1)} - \delta^{(1)}}{1 + 2\delta^{(1)}} \tag{2.44}$$

$$\eta^2 = \frac{\varepsilon^{(2)} - \delta^{(2)}}{1 + 2\delta^{(2)}} \tag{2.45}$$

$$\eta^3 = \frac{\varepsilon^{(1)} - \varepsilon^{(2)} - \delta^{(3)}(1 + 2\varepsilon^{(2)})}{(1 + 2\varepsilon^{(2)})(1 + 2\delta^{(3)})} \tag{2.46}$$

$$\tag{2.47}$$

2.4 Orthorhombic anisotropy due to an imperfect disorder

The velocity measurements revealed that one of the visually layered DR-samples demonstrates nine independent stiffnesses as the orthorhombic medium, see section 4.2.4. Here, we suggest a possible mechanism how the micro- and macroscopically layered sediments could behave as the seismically orthorhombic medium. Microscopic study of the sample did not reveal any significant role of the cracks in this phenomenon. Instead, was observed an alignment of the mineral grains, see Figure 2.1, a).

We consider the symmetrical distribution of the mineral grains as a possible origin of the seismic orthorhombicity. In an imaginary medium consisting of ideally symmetrically distributed grains as in Figure 2.1, b) left hand side, can be expected symmetry of the elastic properties along both axial directions. These two systems of orthogonal lines are represented by the blue dashed lines. In an imagined medium with some realistic disorganization of the grains alignment, as in Figure 2.1 b) right hand side, can be expected some symmetry in its structure. Dependent on the degree of (dis)organisation, some anisotropy of elastic parameters could still be present (due to the aligned composition). By transition from the two dimensional into the three dimensional medium the same effect takes place, see Figure 2.1, c). Analysis of the scanning electron microscope snapshots of the sample DR, repeated for the thin section parallel and perpendicular to the layering, revealed some weak order of the mineral grains distribution, see Figure 2.1, a). We consider that, to some extent, regular grain distribution in the sample is a possible reason for the weak orthorhombic symmetry of the medium. The ultrasonic measurements confirm the seismic orthorhombicity of the medium. We call it seismic anisotropy due to an imperfect grain disorder.
Measurements of the orthorhombic sample under uniaxial loading reveals that the velocities propagating in the axial direction demonstrate nonlinear stress-sensitivity, indicating the presence of compliant porosity. On the other hand, the orthorhombic symmetry does not disappear under a stress of 30 MPa, indicating at least a mixed origin for the anisotropy. Thus, orthorhombic symmetry is unlikely to be explained exclusively by the presence of the compliant crack-like porosity. Actually, a weak spatial order could be related to an increase of the compliant pore space, via spatially organised grain–grain contact areas. We believe that this topic has a large potential for future research and may have some similarities with other scientific fields, for example with the spatial order in alloys and crystals (e.g., Cadeville and Morán-López, 1987).

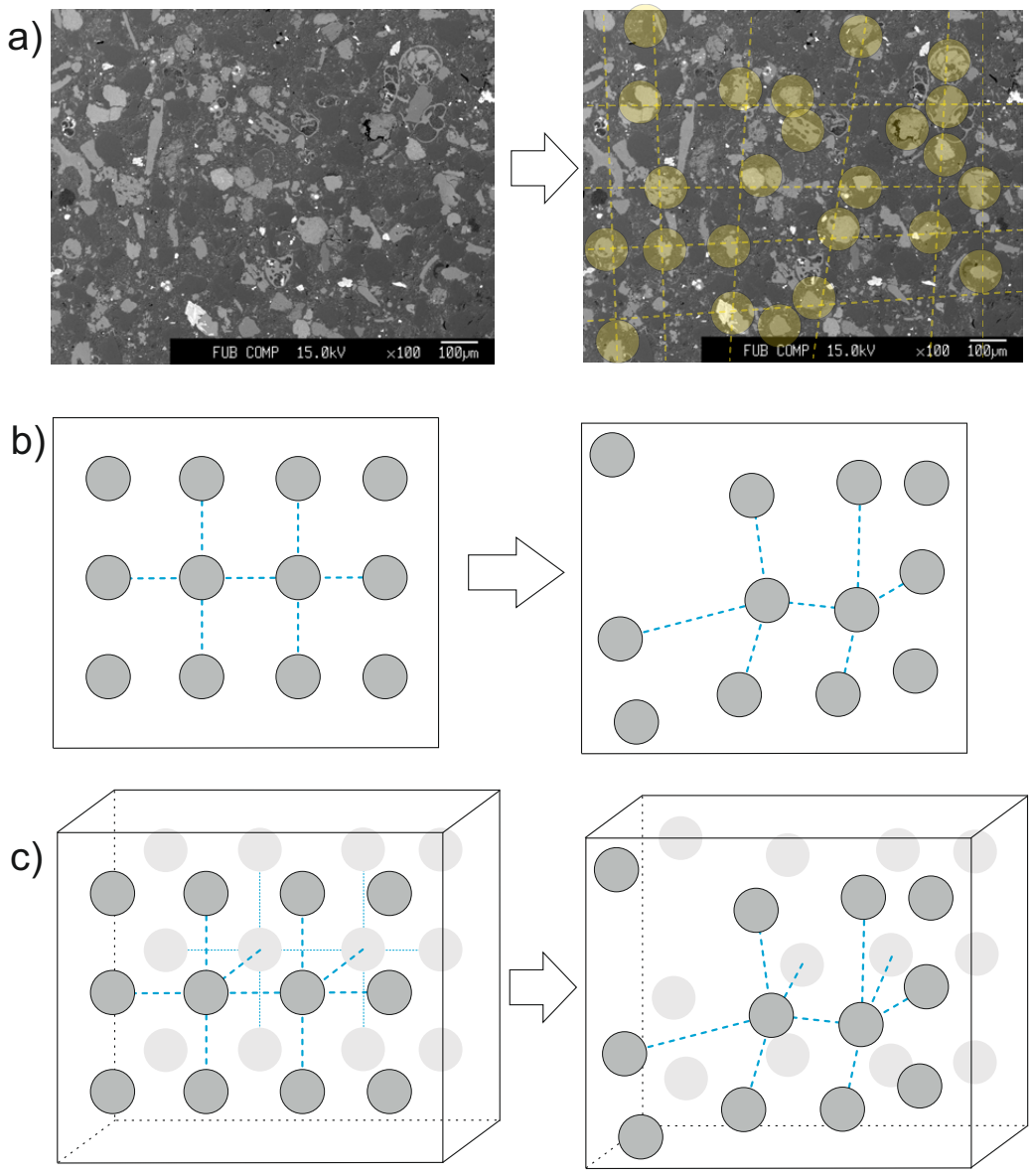

Figure 2.1: *Mineral grain distribution as the origin of the orthorhombic anisotropy. On top: indication of the grains on the SEM snapshot of the investigated marlstone sample. In the middle: regular and realistically disorganised distribution (an imperfect disorder) of the grains in 2D. On bottom: a section of the considered structure in 3D. Grey and yellow circles represent the mineral grains. Blue and yellow dashed lines indicate the symmetry planes.*

2.5 Porosity deformation approach

The theory of Shapiro and Kaselow (2005) can be cosidered as a fortunate compromise between simplicity, limited number of constants, physically reasonable formulation of each parameter, and realistic modelling. This theory proposes a description of stress-dependent rock elasticity based on proelasticity principles (e.g., Biot, 1962; Brown and Korringa, 1975), where deformation of the pore space defines the change of the elastic constants. Recently, Shapiro (2017) expanded this formalism for any kind of seismically anisotropic medium (from transversely isotropic to triclinic), without any prior information about the orientation or spatial distribution of micro-cracks. The porosity deformation approach (PDA) is a further development of the piezo-sensitivity theory Shapiro (2003) and was used for the theoretical modelling presented in this thesis.

Porosity can be classified according to its geometry. It turns out that the geometrical configuration of the pore space greatly influences physical properties of the medium (e.g., Walsh, 1965a; Jaeger and Cook, 1969). The key parameter for the pore space classification is called aspect ratio γ and represents a relation between minimum and maximum dimensions of a single pore (in 2-D it would be the height and the length). If the aspect ration is larger than 0.1, then the form of the pore space becomes similar to the sphere and such a pore is called the stiff pore. If the aspect ratio is smaller than 0.1, the pore is thin and long and is called the compliant pore. Compliant porosity is usually represented by micro-cracks, joints, grain boundary domains and faults. The stiff and the compliant porosity have a different contribution to the stress-dependent elasticity. Sphere-like stiff porosity is less stress sensitive than elongated crack-like compliant porosity. PDA proposes that stiff porosity demonstrates a linear contribution to the stress sensitivity and compliant porosity shows an exponential contribution to the stress sensitivity. This physically based assumption enables a detailed description and analysis of the stress dependent elasticity.

Below, are introduced the basic theoretical framework and equations, however for the detailed description please see Shapiro (2017). Since this dissertation is dedicated to the stress-dependent elasticity, the stress is introduced at first. The compression stress, in respect to the solid phase, is considered as negative. Effective pressure is defined as the difference between confining pressure and pore pressure. The stress dependency is modeled in terms of compliance tensors. The compliance tensor of drained rock is denoted as S^{dr}_{ijkl} and the compliance tensor of a reference rock is indicated as S^{drs}_{ijkl}, respectively. Reference rock represents a special state of the considered rock. It is called the "Swiss cheese" model and it provides the necessary a priori stress-independent information about the medium. In this "Swiss cheese" state (Shapiro, 2003) the compliant porosity is absent (or closed) and the stiff porosity is unchanged/undeformed. Compliant porosity is denoted as ϕ^c_{ik} and stiff porosity as ϕ^s_{ik}, while compliant and stiff porosities of the unloaded rock are denoted as ϕ^{c0}_{ik} and ϕ^{s0}_{ik}. A key parameter in the theory is called the stress sensitivity tensor and it is denoted as θ^c. Basically, it describes change of the compliance tensor in relation to the porosity tensor, see equation 2.55. The bulk compressibility of the reference rock C^{drs} is introduced as a normalizing factor making the tensor θ^c dimensionless.

$$\theta^c_{ijklmn} = \frac{1}{C^{drs}} \frac{\partial S^{dr}_{ijkl}}{\partial \phi^c_{mn}}, \tag{2.48}$$

Stress-dependent elasticity of drained rocks can be written in form of equation 2.49 (equation (79) in Shapiro (2017)).

$$S^{dr}_{ijkl} = S^{drs}_{ijkl} + K^{(1)}_{ijkl}\sigma_1 + K^{(2)}_{ijkl}\sigma_2 + K^{(3)}_{ijkl}\sigma_3 + \delta_{ik}B_{jl}e^{F_c(\sigma_j+\sigma_l)/2} + \delta_{il}B_{jk}e^{F_c(\sigma_j+\sigma_k)/2} + \delta_{jk}B_{il}e^{F_c(\sigma_i+\sigma_l)/2} + \delta_{jl}B_{ik}e^{F_c(\sigma_i+\sigma_k)/2}, \quad (2.49)$$

where $K^{(I)}_{ijkl}$ describes the contribution of stiff porosity; δ_{ik} is the Kronecker delta; $B_{ik} = F_c\phi^{c0}_{ik}/4$ and $F_c = C^{drs}\theta^c$ describes the contribution of compliant porosity.

PDA for a vertical transversely isotropic medium under uniaxial load

The PDA was applied to the experimentally obtained data sets. For the modelling was used a set of equations obtained from equation 2.49. If the medium has a vertical transversely isotropic (VTI) symmetry and the stress is applied uniaxially along the symmetry axis x_3, then equations set has the following form:

$$\begin{aligned}
S^{dr}_{11} &= S^{dr}_{22} = S^{dr}_{1111} = S^{drs}_{1111} + K^{(3)}_{1111}\sigma_3 + 4B_{11},\\
S^{dr}_{33} &= S^{dr}_{3333} = S^{drs}_{3333} + K^{(3)}_{3333}\sigma_3 + 4B_{33}e^{F_c\sigma_3},\\
S^{dr}_{44} &= S^{dr}_{55} = 4S^{dr}_{1313} = 4S^{drs}_{1313} + 4K^{(3)}_{1313}\sigma_3 + 4B_{33}e^{F_c\sigma_3} + 4B_{11},\\
S^{dr}_{66} &= 4S^{dr}_{1212} = 4S^{drs}_{1212} + 4K^{(3)}_{1212}\sigma_3 + 4B_{22} + 4B_{11},\\
S^{dr}_{13} &= S^{dr}_{23} = S^{dr}_{1133} = S^{drs}_{1133} + K^{(3)}_{1133}\sigma_3,
\end{aligned} \quad (2.50)$$

PDA for a vertical transversely isotropic medium under uniaxial load, after Ciz and Shapiro (2008)

Just for the two VTI samples, BaZ and DH06 was applied a slightly different formulation of the equations set, see equation 2.51. This has the following explanation. First, the influence of the stiff porosity is negligible. Second, these particular modelling results were already published , see Sviridov et al. (2017). The medium has a vertical transversely isotropic (VTI) symmetry and the stress is applied uniaxially along the symmetry axis x_3.

$$\begin{aligned}
S^{dr}_{11} &= S^{dr}_{22} = const,\\
S^{dr}_{33} &= S^{sc}_{33} + K_3\sigma_3 + D_{333}e^{-\Gamma_3\sigma_3},\\
S^{dr}_{44} &= S^{sc}_{44} + K_4\sigma_3 + D_{144} + D_{244} + D_{344}e^{-\Gamma_3\sigma_3},\\
S^{dr}_{66} &= const,\\
S^{dr}_{13} &= const,
\end{aligned} \quad (2.51)$$

PDA for a vertical transversely isotropic medium under triaxial load

For the modelling was used a set of equations obtained from equation 2.49. If the medium has a vertical transversely isotropic (VTI) symmetry and the hydrostatic stress is applied, then equations set has the following form:

$$
\begin{aligned}
&S_{11}^{dr} = S_{22}^{dr} = S_{1111}^{dr} = S_{1111}^{drs} + K_{1111}^{(1)}\sigma_1 + K_{1111}^{(2)}\sigma_2 + K_{1111}^{(3)}\sigma_3 + 4B_{11}e^{F_c\sigma_1},\\
&S_{33}^{dr} = S_{3333}^{dr} = S_{3333}^{drs} + K_{3333}^{(1)}\sigma_1 + K_{3333}^{(2)}\sigma_2 + K_{3333}^{(3)}\sigma_3 + 4B_{33}e^{F_c\sigma_3},\\
&S_{44}^{dr} = S_{55}^{dr} = 4S_{1313}^{dr} = 4S_{1313}^{drs} + 4K_{1313}^{(1)}\sigma_1 + 4K_{1313}^{(2)}\sigma_2 + 4K_{1313}^{(3)}\sigma_3 + 4B_{33}e^{F_c\sigma_3} + 4B_{11}e^{F_c\sigma_1},\\
&S_{66}^{dr} = 4S_{1212}^{dr} = 4S_{1212}^{drs} + 4K_{1212}^{(1)}\sigma_1 + 4K_{1212}^{(2)}\sigma_2 + 4K_{1212}^{(3)}\sigma_3 + 4B_{22}e^{F_c\sigma_2} + 4B_{11}e^{F_c\sigma_1},\\
&S_{13}^{dr} = S_{23}^{dr} = S_{1133}^{dr} = S_{1133}^{drs} + K_{1133}^{(1)}\sigma_1 + K_{1133}^{(2)}\sigma_2 + K_{1133}^{(3)}\sigma_3,
\end{aligned}
\tag{2.52}
$$

PDA for an orthorhombic medium under uniaxial load

If the medium has an orthorhombic symmetry and the stress is applied uniaxially along the symmetry axis x_1, then equations take the following form:

$$
\begin{aligned}
&S_{11}^{dr} = S_{1111}^{dr} = S_{1111}^{drs} + K_{1111}^{(1)}\sigma_1 + 4B_{11}e^{F_c\sigma_1},\\
&S_{22}^{dr} = S_{2222}^{dr} = S_{2222}^{drs} + K_{2222}^{(1)}\sigma_1 + 4B_{22},\\
&S_{33}^{dr} = S_{3333}^{dr} = S_{3333}^{drs} + K_{3333}^{(1)}\sigma_1 + 4B_{33},\\
&S_{44}^{dr} = 4S_{2323}^{dr} = 4S_{2323}^{drs} + 4K_{2323}^{(1)}\sigma_1 + 4B_{33} + 4B_{22},\\
&S_{55}^{dr} = 4S_{1313}^{dr} = 4S_{1313}^{drs} + 4K_{1313}^{(1)}\sigma_1 + 4B_{33} + 4B_{11}e^{F_c\sigma_1},\\
&S_{66}^{dr} = 4S_{1212}^{dr} = 4S_{1212}^{drs} + 4K_{1212}^{(1)}\sigma_1 + 4B_{22} + 4B_{11}e^{F_c\sigma_1},\\
&S_{13}^{dr} = S_{1133}^{dr} = S_{1133}^{drs} + K_{1133}^{(1)}\sigma_1,\\
&S_{23}^{dr} = S_{2233}^{dr} = S_{2233}^{drs} + K_{2233}^{(1)}\sigma_1,\\
&S_{12}^{dr} = S_{1122}^{dr} = S_{1122}^{drs} + K_{1122}^{(1)}\sigma_1,
\end{aligned}
\tag{2.53}
$$

In the case of uniaxial loading along the symmetry axis, x_1, the coefficients B_{22} and B_{33} are included (subsumed) in the fitting coefficient of the reference state parameter S_{ijkl}^{drs}. This is explained by the absence of stress in the direction of the symmetry axes x_2 and x_3 and the corresponding stress-independence of B_{22} and B_{33}.

Parameters of the PDA

The PDA provides an instrument for estimating the individual influence of stiff and compliant pore space. For this purpose, elastic medium is modeled twice: first taking into account the stiff porosity and second without taking into account the stiff porosity. Equation (2.49) is used for both modellings. If the stiff porosity is assumed to be negligible, then the term $K_{ijkl}^{(I)}$ equals to zero. Results of the two modelling steps can be compared to estimate the contribution of stiff porosity.

Initial compliant pore space (corresponding components of generalized compliant porosity) can be estimated using the PDA with equation 2.54:

$$
\phi_{ik}^{c0} = \frac{4B_{ik}}{F_c} \tag{2.54}
$$

The tensor of the stress sensitivity θ_i^c and the generalized porosity ϕ_{ik}^{c0} mainly control the nonlinear moduli of the stress-dependent elastic parameters. The stress sensitivity tensor is assumed to be symmetric and

independent of any spatial rotation and of any plane reflection (i.e., it is assumed to be isotropic), for more details see Shapiro (2017). This quantity is defined by the equation 2.55:

$$\theta_i^c = \frac{F_c}{C^{sc}}, \tag{2.55}$$

where C^{sc} is the bulk compressibility of the Swiss cheese model and corresponds to:

$$C^{sc} = S_{11}^{sc} + S_{22}^{sc} + S_{33}^{sc} + 2(S_{12}^{sc} + S_{13}^{sc} + S_{23}^{sc}). \tag{2.56}$$

For modelling of the samples BaZ and DH06, is used an optimization algorithm for the porosity deformation approach, called the universal exponent approach (UNE). This algorithm is to some extend similar to the algorithm proposed by Ciz and Shapiro (2008). The algorithm consists of three steps:

1. In the first modelling step, coefficient F_c is fitted separately for each compliance (for example F_c^{11} for S_{11}^{dr} and F_c^{55} for S_{55}^{dr}).
2. Calculation of F_c^{une} as average of all F_c, which were calculated in step 1 ($F_c^{une} = average(F_c^{11}, F_c^{22}, ..., F_c^{66})$).
3. Second modelling step, implementing F_c^{une} instead of the initial F_c.

The optimization algorithm is suitable for the formulation of the theory after Ciz and Shapiro (2008).

2.6 Constant anellipticity approach

Measurements of the off-axis elastic waves propagated under an oblique angle to the symmetry axis is a non-trivial task. In the case of stress-dependent measurements, this becomes a complex matter. These technical difficulties can lead to the incomplete data sets for the laboratory measurements. Here, is proposed a theoretical approach for the estimation of the stress-dependent off-axis velocities, which is called the constant anellipticity approach (CAN).
Alternative approaches based on the cracks averaging effects are available, see for example Pervukhina et al. (2011). An advantage of the CAN approach is the following: it is based on the PDA theory and it is geometry-assumptions independent.

The basic assumption of the CAN is that the anellipticity parameter η_0' remains constant as stress is applied. The constant anellipticity is a result of isotropic, nonlinear, third-order elasticity tensor in the nonlinear elasticity theory (Rasolofosaon, 1998). In the PDA approach, this is a consequence of the assumption of an isotropic piezosensitivity tensor. The isotropic piezosensitivity is directly related to the third-order elasticity tensor (Shapiro and Kaselow, 2005), Ciz and Shapiro (2008) and Shapiro (2017)). Following Curie's principle (Curie, 1894) the observable effects are at least as symmetric as their causes, which means that if the stress induced third-order elasticity tensor is isotropic, then the load will not influence the anellipticity. The anellipticity depends then exclusively on the "Swiss cheese" component. In other words, stress-induced part of the anisotropy is approximately elliptical. Some observations and discussions of this phenomenon can be found in Prioul et al. (2004). Following Thomsen (1986) η_0' is defined as the difference between ε_0 and δ_0, for definitions see Appendix 2.2:

$$\eta_0' = \varepsilon_0 - \delta_0 \tag{2.57}$$

The CAN approach assumes that stress application is only allowed parallel to the symmetry axes. Hence, uniaxial, hydrostatical or triaxial loading can be applied. The strain-energy requirements (stability conditions) were applied for controlling results of the method (e.g., Auld, 1990). The rock samples considered in this thesis satisfy these requirements. In the sense of obtained results, the CAN approach is to some extent consistent with the algorithm devised by Muir and Dellinger (1985) and Fomel (2004). However, in contrast to these algorithms CAN describes the stress dependency of the off-axis velocities.

Input data

The following data are required for the application of the CAN: three independent diagonal elements of the stiffness tensor, C_{11}, C_{33}, C_{44}, and the initial off-axis velocity at zero stress, quasi P-wave $P_{44}(0)$. The off-axis velocity in unloaded state, $P_{44}(0)$, can be either measured or estimated theoretically. Here, is considered an empirical approach derived by Ryan-Grigor (1998) to estimate δ_0 and then extract $P_{44}(0)$, see equation 2.58.

$$\delta = \frac{[1 + (3.87\frac{V_p}{V_s} - 5.54)]^2 - [(\frac{V_p}{V_s})^2 - 1]^2}{2(\frac{V_p}{V_s})^2[(\frac{V_p}{V_s})^2 - 1]}, \tag{2.58}$$

where V_p and V_s are axially propagated P- and S-waves, respectively.

In the case of triaxial loading of the sample HR1-VTI, was used an alternative empirical approach (Horne (2013), equation 14) for estimation of $P_{44}(0)$:

$$C_{13} = 0.9213(C_{33} - \frac{4}{3}C_{44}) - 1.2711, \tag{2.59}$$

where C_{13}, C_{33} and C_{44} are the stiffnesses.

Algorithm

The CAN algorithm consists of three steps:

1. In an unloaded state are calculated:
   - ε_0 and δ_0
   - η_0' according to equation 2.57
2. Stress dependent $\delta(\sigma) = \varepsilon(\sigma) - \eta_0'$
3. Stress dependent $C_{13}(\sigma)$ and $P_{44}(\sigma)$ are obtained from $\delta(\sigma)$

The index $_0$ denotes unloaded state and (σ) indicates stress. The complete set of equations and definitions are given in the Appendix 2.2.

Output data

The output parameters are provided as functions of the stress: (estimated) independent non-diagonal element of the stiffness tensor $C_{13}(\sigma)$ and the off-axis velocity $P_{44}(\sigma)$.

2.7 Symmetry axes notation

Here, is used the notation given by Cheadle et al. (1991). Two different experimental set-ups were used; one for the vertical transversely isotropic (VTI) medium and one for the orthorhombic medium. The internal rock coordinate system remains unchanged for both experimental set-ups, which means that the symmetry axis x_3 is always parallel to the rotational symmetry of the rock. Due to the two different initial symmetries of the measured samples the direction of the symmetry axis x_3 is changing in the global coordinate system. Here, are introduced both coordinate systems with corresponding illustrations.

Notation for VTI medium

The differential axial loading was applied parallel to the rotation axis of a cylindrical sample x_3 (see Figure 2.2). The numeric index consisting of two digits labels the direction of propagation and polarization of ultrasonic waves. The first digit labels the direction of the propagation and the second digit shows the polarization. Axial P- and S- waves are denoted as V_{33} and V_{31}, respectively. The radial P- and S- waves polarized parallel to the bedding are displayed as V_{11} and V_{21}, respectively.

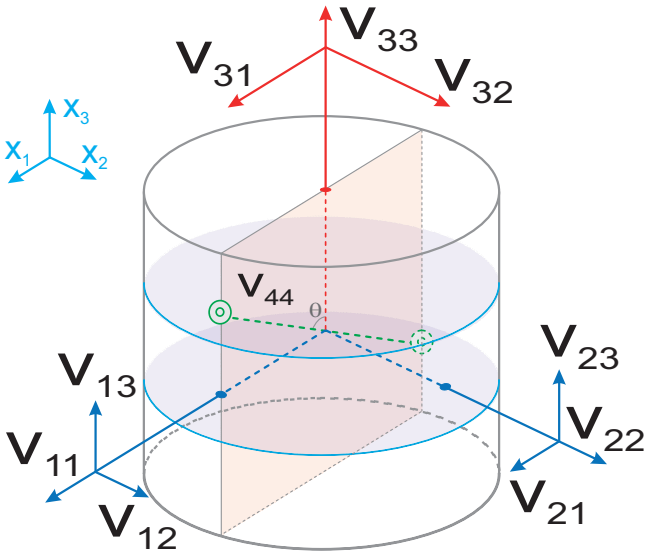

Figure 2.2: *Notation of the elastic waves for a VTI medium. Layering is indicated by blue circles. Differential axial loading was performed along the x_3 direction. The main directions of wave propagation lie along the three symmetry axes. Velocity notations are defined by indices, where the first index denotes the direction of wave propagation and the second index labels the polarization.*

Notation for orthorhombic medium

The elastic orthorhombic medium is produced by the application of an uniaxial loading on the initially horizontal transversely isotropic (HTI) sample. The symmetry axis x_3 was supposed to lie along the rotation axis of the tilted medium for both experimental set-ups. Since the VTI and HTI rotation axes are perpendicular to each other, this causes change of the notation. Vertical direction becomes x_1 instead of x_3 (see Figure 2.3). Nine required elastic wave velocities were measured in the following directions: V_{11}, V_{12} and V_{13} P- and S- waves in the axial (loading) direction, polarized perpendicular and parallel to the bedding plane, respectively; V_{22} and V_{23} P- and S- waves propagated in the radial direction perpendicular to the bedding and polarized parallel to the bedding plane; V_{33} and V_{31} P- and S- waves propagated in the radial direction parallel to the bedding and polarized parallel to the bedding plane; V_{66} the off-axis quasi P-wave velocity measured in symmetry plane 32 at an angle of $45°$ to two other symmetry planes (and to the bedding).

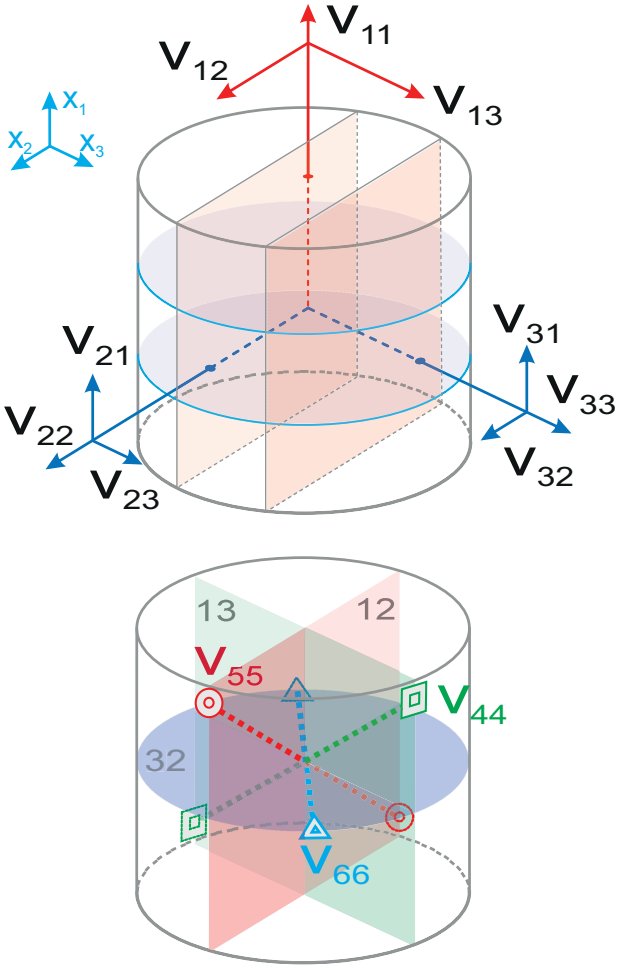

Figure 2.3: *Notation of the elastic waves for an orthorhombic medium. Layering is indicated by the red colour. The axial loading was applied along the x_1 direction. Top: directions of the wave propagation parallel to the three symmetry planes. Velocity notations are defined by indices, where the first digit denotes the direction of wave propagation and the second digit labels the wave polarization. Bottom: directions of wave propagation for the off-axis velocities. The direction of the wave propagation of V_{66} is under 45° to the two vertical symmetry planes* 13 *and* 12.

Part II

Uniaxial loading

Chapter 3

Experimental methodology: uniaxial loading

This Part is dedicated to the dependence of the shale rock's elastic parameters on the uniaxial loading. Firstly, the corresponding laboratory measurements were performed and then the porosity deformation approach (PDA) was applied to obtained experimental data. The PDA aims at describing and explaining the experimentally observed behaviour. The applicability of the theory was examined by comparison of the laboratory observations and the theoretically modeled data. The modelling enables physically based interpretation, description and analysis of the theoretical expectations against the experimental observations.
In the beginning are introduced the laboratory experiments, including the ultrasonic measurements and deformation measurements under uniaxial loading. Particularly, are described the studied samples, the laboratory equipment as well as the experimental procedure. The PDA is introduced in Part I. Subsequently is applied the theoretical modelling, using obtained experimental data. Finally the experimental and the theoretical data are compared for the mutual analysis and interpretation.

3.1 Stress distribution in the uniaxially loaded sample

The aim of the numerical modelling was a better understanding of the stress distribution in the core sample under uniaxial loading conditions and an estimation of the stress-induced anisotropy. Modelling was performed in COMSOL Multiphysics v3.5a, based on the finite element method.
The study of the uniaxial loading on induced anisotropy, was particularly focused on the question: does the uniaxial loading produce additional horizontally oriented anisotropy planes? This would turn an initially isotropic medium into a vertical transversely isotropic (VTI) medium, or would turn an initially horizontal transversely isotropic (HTI) medium into a seismically orthorhombic medium (see Figure 3.2).

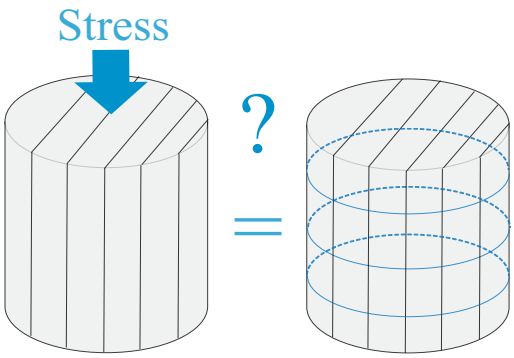

Figure 3.1: *Left: the HTI sample before the loading. Right: the HTI sample after the loading plus induced symmetry planes, which turn the initially HTI medium into a seismically orthorhombic medium.*

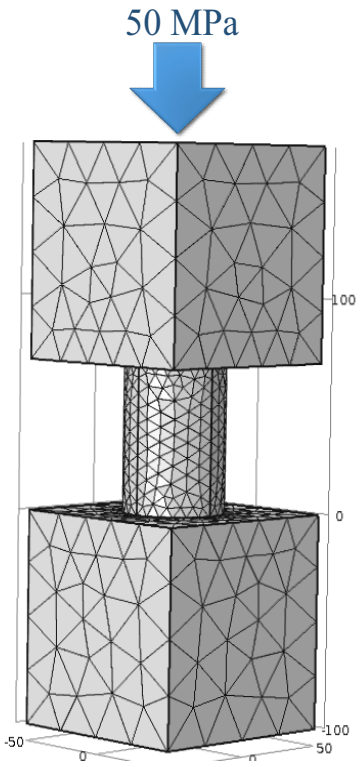

Figure 3.2: *The model set-up with variable mesh size. Core sample is placed between the two steel plates. Uniaxial loading is equal to 100 kN or 50 MPa.*

At first, was modeled the stress distribution in an isotropic sample. This model has a variable height of the sample, but a constant diameter: the height variate from 20 mm to 70 mm and the diameter equals 50 mm. Afterwards, was modeled the stress distribution in an anisotropic sample. Modelling results for the isotropic and moderately anisotropic samples are comparable. The second goal of the modelling was the design of the real experiments. The following key features were studied: optimal core sample geometry in regard to the size of the ultrasonic transducers; stability of the sample; placement of the lateral transducers.

Model setup

Modelling was performed in 3-D. The model includes a core sample and two steel plates, representing the measuring cell, see Figure 3.2. Stiffness parameters for the anisotropic shale sample were taken from Hornby (1998). Isotropic stiffness parameters were calculated as averaged anisotropic parameters. Steel plates and the core sample have variable mesh size. The boundary between the steel plate and the sample is coincident, there is no displacement of core sample relative to the press plates. The applied uniaxial load is equal to 100 kN or 50 MPa. The modelling results are presented on the example of isotropic sample with 50 mm diameter and 60 mm height (as the simple and the representative example).

Modelling results demonstrate the stress distribution in the sample. The stress distribution itself can be displayed in several ways. The direct way to present stress is to show separately the components of the stress: the vertical component and the horizontal component. Another way is to present stresses as the summation over all components (kind of an equivalent stress). Von Mises stress is defined as the difference between the main stress components, plus a sum of additional components of stress with

corresponding coefficients (Mises, 1913).

$$\sigma_v = \sqrt{\frac{1}{2}[(\sigma_{11} - \sigma_{22})^2 + (\sigma_{22} - \sigma_{33})^2 + (\sigma_{33} - \sigma_{11})^2 + 6(\sigma_{12}^2 + \sigma_{23}^2 + \sigma_{31}^2)]}, \tag{3.1}$$

where σ_v is Von Mises stress; $\sigma_{11}, \sigma_{22}, \sigma_{33}$ are the stresses in the main directions; $\sigma_{12}, \sigma_{23}, \sigma_{31}$ are the stresses in the diagonal directions. Von Mises stress formulation is suitable for the investigation of the stability and of the yielding.

Results

The modelling results are presented in two variants: as the description of the separate stress components and as the description of the von Mises stress, see Figure 3.3.

Description of the separate vertical and horizontal stress components. Due to the cylindrical form of the sample there are only two independent stress components along the symmetry axes directions: the vertical component and the horizontal component. The vertical stress component has a much larger magnitude in comparison to the horizontal one. The vertical stress component is mainly concentrated in the central area of the sample and demonstrates a smaller magnitude along the free surfaces of the sample. A significant stress concentration is observed at the corners of the sample.

The tensile horizontal stress component is concentrated along the adjacent zone of the steel plate - sample surface boundary. The greater the distance from this boundary area the smaller the horizontal stress component. Some stress concentration is observed at the corners of the sample.

The Von Mises stress shows the inhomogeneous stress distribution in the sample and demonstrates a similar distribution as the vertical component of the stress.

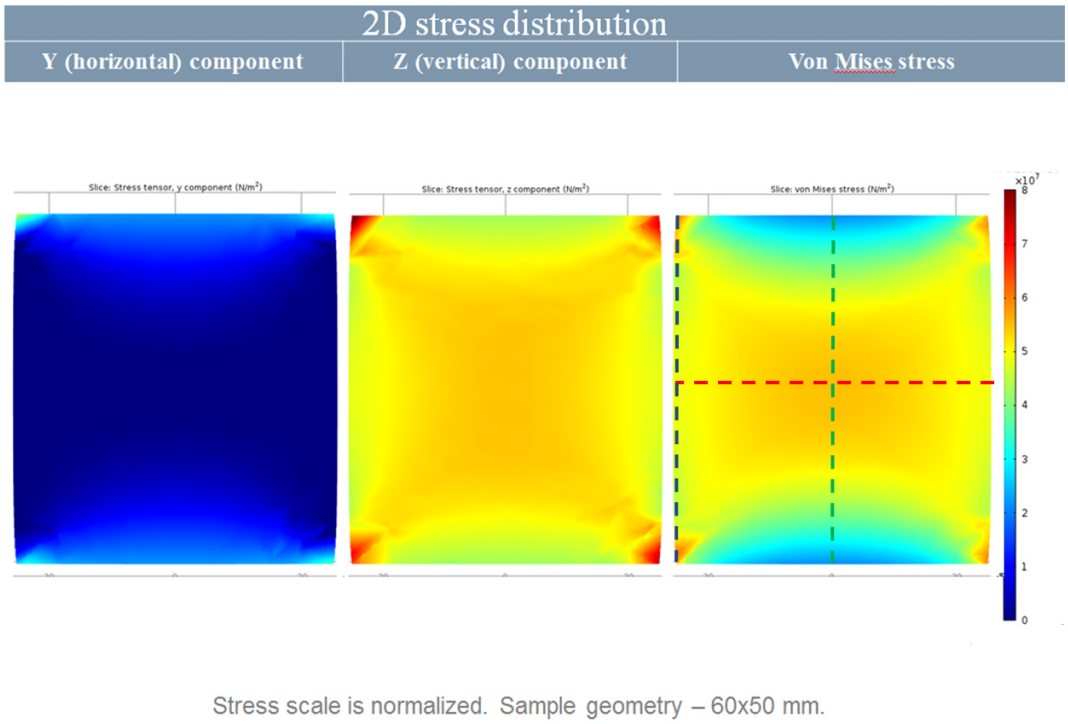

Figure 3.3: *2-D slices of the stress distribution in the uniaxially loaded sample. Left – horizontal stress component; middle – vertical stress component; right – Von Mises stress (equivalent stress). Dashed lines display the profiles for quantitative analysis.*

Profiles

The main interest for real experiments invokes the stress distribution along profiles of the ultrasonic waves travel path. Three profiles are analyzed: first profile along the vertical symmetry axis – green dashed line; second profile along the horizontal axis in the middle of the sample – red dashed line; and the third profile on the edge of the sample – blue dashed line, see Figure 3.3, on the right. For a better understanding and the quantitative analysis the stress distribution along three profiles is displayed on the combined graphic, see Figure 3.4.

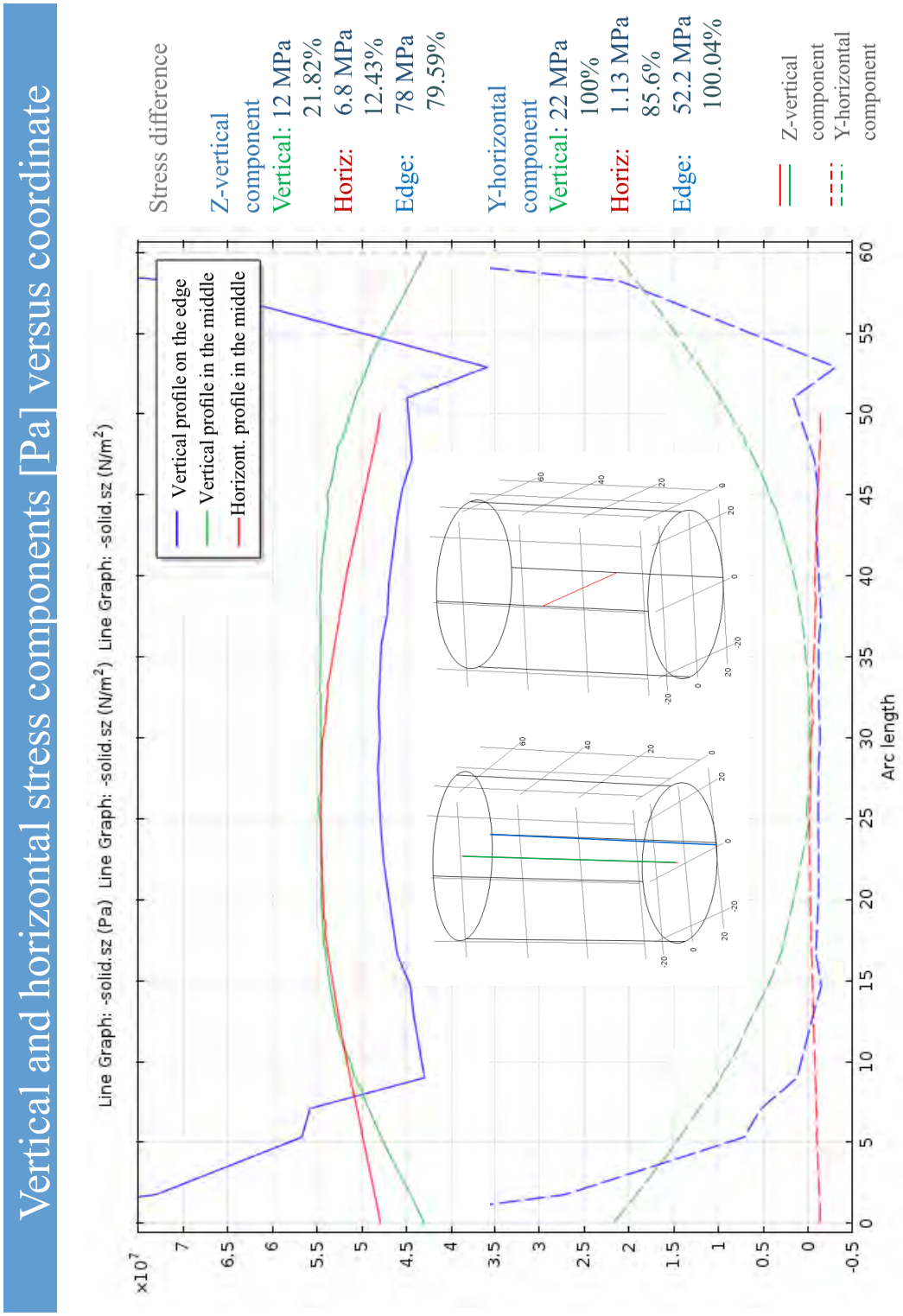

Figure 3.4: *Distribution of the vertical (top, solid lines) and the horizontal (bottom, dashed lines) stress components along three profiles.*

The vertical component of the stress. The vertical profile along the symmetry axis (solid green line) displays a maximum of 55 MPa in the middle of the sample and a parabolic shape of the stress decrease towards sample's surface with minimum of 43 MPa. The horizontal profile through the middle of the sample (solid red line) shows a maximum of 55 MPa in the middle of the sample (crossing with vertical profile) and demonstrates parabolic shape of the stress decrease towards sample's lateral surface with minimum of 48 MPa. The vertical profile along the sample's edge (solid blue line) shows a maximum of 48 MPa in the center and decreases towards the press plates. The stress concentration at the corners can be explained by the numerical effects and by the boundary conditions.

The horizontal component of the stress. The vertical profile along the symmetry axis (dashed green line) indicates a minimum of 0 MPa in the middle of the sample and a parabolic form of the stress increase towards the press-sample boundary with a maximum of 22 MPa. The stress component along the horizontal profile (dashed red line) is negligibly small. The vertical profile along the sample's edge (dashed blue line) display the minimum of 0 MPa in the middle of the sample and a significant increase towards the press-sample boundary.

Discussion

The vertical component of the stress is much larger than the horizontal component of the stress, which can be explained by the uniaxial loading along the vertical direction. The vertical component of the stress is concentrated in the center of the sample.

The horizontal component of the stress is concentrated near the press-sample boundary and is induced by friction forces. The sample expands in the radial direction and the press plates restricts the displacement of the sample's surfaces. Friction forces between the press and the sample induce the horizontal component of the stress in an uniaxially loaded sample. The horizontal component of the stress decreases with increasing distance from the press-sample boundary.

Corners of the sample. The stress values in the corners of the sample demonstrate high values and to our understanding these correspond to numerical artifacts caused by the modelling set-up, which restricts the displacement of the sample's surface relative to the press plates. Such a fixed boundary condition significantly simplified the model, in the real experiment an aluminum foil is placed between the sample and the press plates.

Conclusions

Induced Anisotropy. The stress distribution in the sample under uniaxial loading is anisotropic and inhomogeneous. In a first approximation the stress field can be separated into three layers: one layer with a high stress concentration placed in the middle of the sample and two layers with a low stress concentration near the press-sample boundary, see Figure 3.5. Therefore, an initially isotropic sample placed under uniaxial loading becomes a seismically VTI medium due to the stress-induced anisotropy planes. Following this logic, an initially HTI sample under uniaxial loading becomes a seismically orthorhombic medium due to the stress induced anisotropy planes, see Figure 3.1.

Design of the measurement cell for off-axis velocity measurements. Analysis of the induced stress field suggests the placement of the transducers at a minimum of 10 mm away from the press-sample boundary (for a sample with 60 mm height and 50 mm diameter). At this distance, the stress field is relatively homogeneous and isotropic. Furthermore, the influence of stress perturbations on the ultrasonic velocities is expected to be less significant and more predictable.

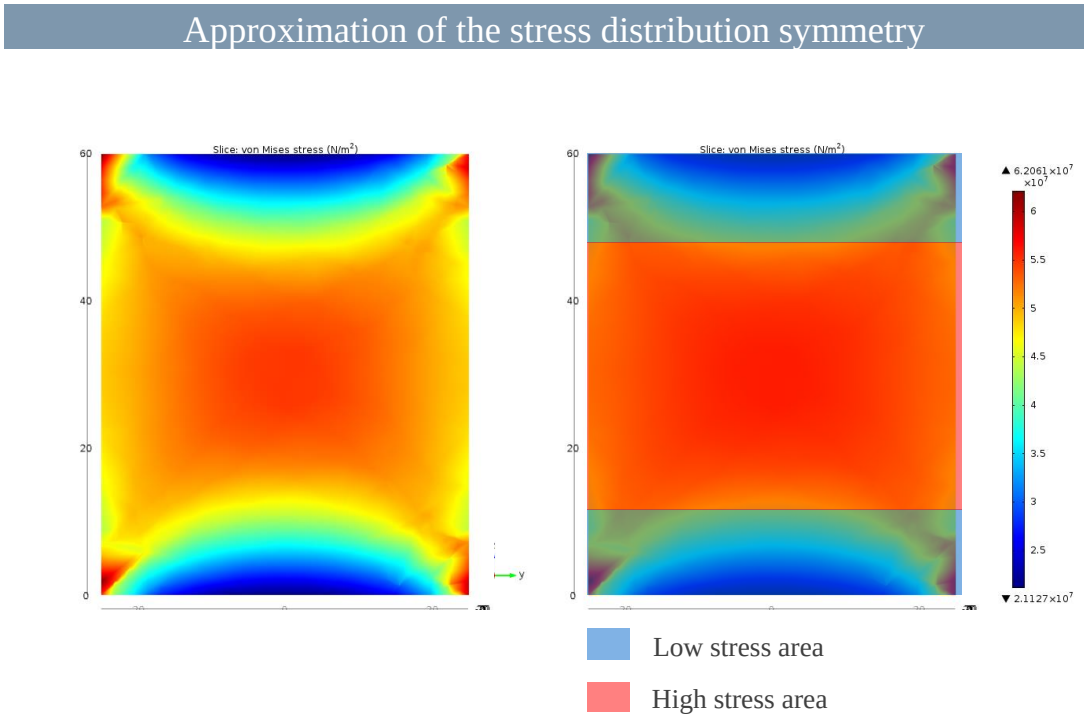

Figure 3.5: *Left – Von Mises stress (equivalent stress) distribution. Right – approximation of the complex stress field by three parallel layers.*

3.2 Experimental methodology

In this section is introduced the laboratory used for the conducted uniaxial loading experiments. Here are described the press, the ultrasonic sensors and the strain gauges. For the design of measuring cell were used the results obtained by finite elements modelling, see section 3.1.

3.2.1 Press and transducers

Used equipment includes a hydraulic uniaxial press and an aluminium measuring cell. The hydraulic press by OMCM is manually driven and is capable of loading up to 20 tons, see Figure 3.6. The original ultrasonic transducers are mounted into the upper and bottom aluminium holders, providing P- and S-waves measurements in the axial direction. An aluminum measuring cell was designed for measurements of P- and S- wave velocities in the radial and in the off-axis (inclined) directions, see Figure 3.7.
The Panametrics-NDT sensors (distributed by Olimpus) with diameter of 17.6 mm were used for measurements of ultrasonic velocities in the radial and in the off-axis directions. The sensors are attached to the surface of the sample with clamps, see Figure 3.7, bottom panel. An assembling aid is used for the positioning of the sample in the center. In order to apply a defined force was use a torque wrench.
For a better coupling between the flat surface of the sensor and the curved surface of the cylindrical sample, was designed a thin round aluminium "boot" which is put on the sensor. The "boot" fits the shape of both surfaces with its two sides and has a thickness of 0.8 mm. For a better coupling between the "boot" and the surfaces was used sugar beet molasses. To protect the sample from penetrating sugar beet molasses, the sample was painted with spar varnish (Bootslack "Le Tonkinois").

Figure 3.6: *Left: the hydraulic press with mounted measuring cell and the sample. Right: 1 – the trigger, 2 – the oscilloscope, 3 – the control device, and 4 – the generators. Photo provided by Jan Evers.*

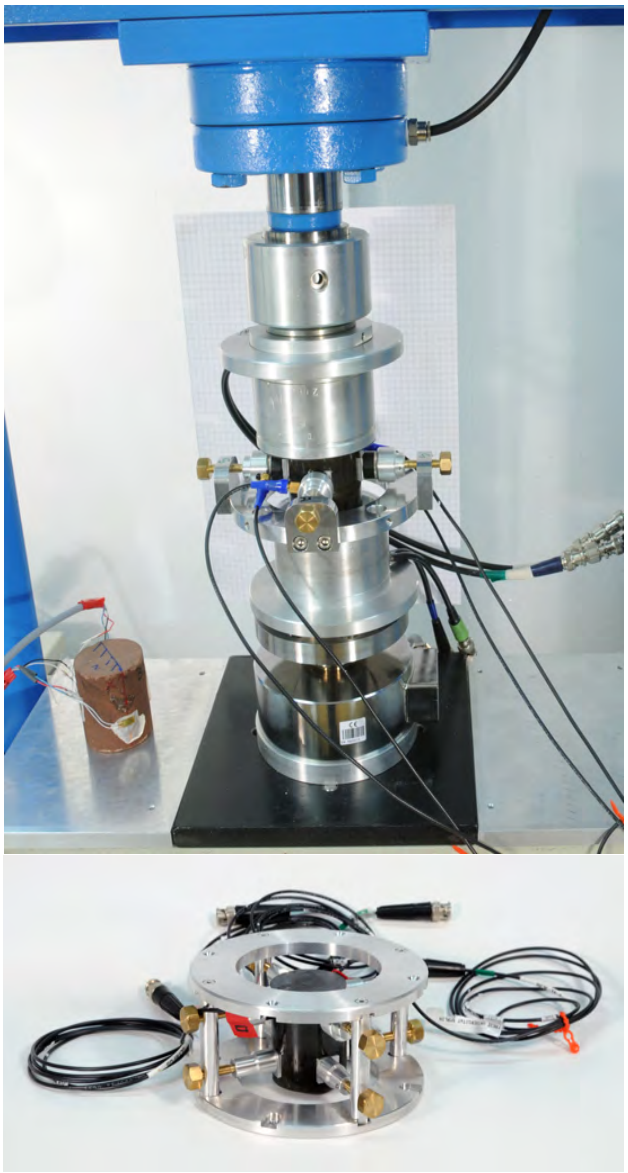

Figure 3.7: *Top: installed measuring cell. Bottom: measuring cell with sample. Photo provided by Jan Evers.*

3.2.2 Strain measurements

The samples were loaded uniaxially i.e. the loading force $\sigma_3 \neq 0$ and $\sigma_1 = \sigma_2 = 0$. The stress was applied in a quasi-static regime, using a manually operated press. The deformation measurements were realized with 4 strain gauges which were glued directly on the sample surface: two strain gauges parallel to the loading direction and two strain gauges perpendicular to the loading direction, see Figure 3.8. Strain gauges were produced by "Hottinger Baldwin Messtechnik GmbH".

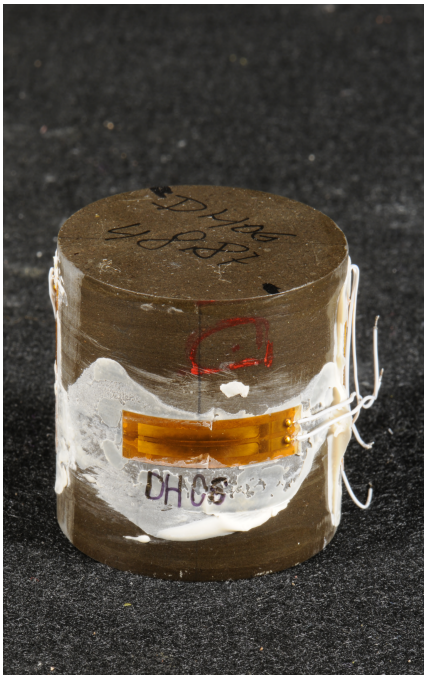

Figure 3.8: *Sample DH06 with glued strain gauges. Photo provided by Jan Evers.*

3.2.3 Measurements methodology

The single-plug measurement methodology was applied and all required seismic velocities were measured on the same sample (Wang, 2002a). Different orientations of the travel path in regard to the layering were achieved by the placement of multiple sensors in various positions. The full set of seismic velocities was determined by the pulse transmission technique at an ultrasonic frequency range of 0.4 -- 1 MHz, (e.g., Mayr and Burkhardt, 2006).

Five independent stiffnesses of the VTI samples were measured in a single experiment. Nine independent stiffnesses of the orthorhombic medium (initially HTI samples) were measured in two separate experiments. Two separate experiments was a minimal possible number to complete the measurements, because of the limited space at the sample's surface required for installation of the transducers.

3.3 Experimental procedure

3.3.1 Travel path in the off-axis direction

For the samples with diameter of 50 mm, the direction of the actual travel path in the off-axis direction lies at the angle of $64°$ ($\Theta = 64°$) in respect to the symmetry axis (vertical axis). The actual travel path was not evident due to the large transducer's size in respect to the sample's diameter. Thus, the actual

travel path was defined experimentally, using the calibration aluminum and steel samples, see Figure 3.9. The average ambient humidity rate was around 50% and the average temperature around 21° Celsius.

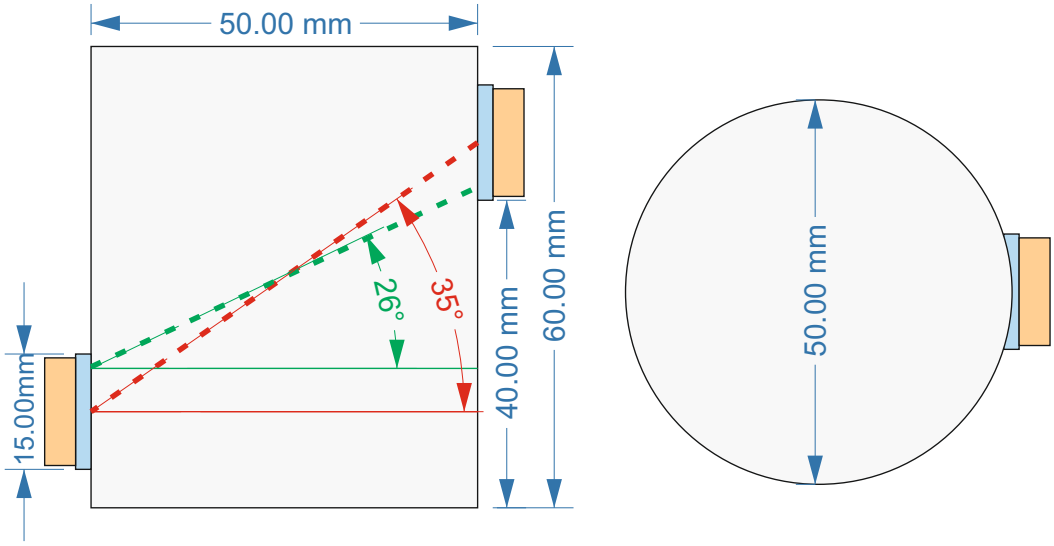

Figure 3.9: *Off-axis velocity measurements. On the left – side view; on the right – top view. Red dashed line indicates the geometrical travel path. Green dashed line displays the actual travel path. Orange boxes – sensors, blue boxes – coupling "boots".*

3.3.2 Phase or group velocity?

For measurements in the field, the first arrival is considered as the group velocity, because the emitters and receivers are much smaller than the seismic wavelengths (e.g., Helbig, 1994). Generally, in laboratory experiments (depending on the experimental set-up), the transducer diameters (centimetres size) are larger than the ultrasonic wave-lengths (millimetres size) and thus, the phase velocity and the phase attenuation are measured (e.g., Rasolofosaon, 2010). For physical considerations see Arenberg (1950) and Neighbours and Smith (1950), for numerical considerations see Dellinger and Vernik (1994).
The question of group or phase velocities in laboratory measurements was studied and discussed (e.g., Every and Sachse, 1990; Dellinger and Vernik, 1994; Wolfe, 2005). A rule of thumb proposed by Dellinger and Vernik (1994) is that the ratio of the length of the propagation path to the width of the transducer illumination needs to be $\geqslant 20$ to measure the group velocity, and $\leqslant 3$ to measure the phase velocity. If the ratio falls between or near these values, the configuration needs a separate, careful consideration (e.g., Abell et al., 2014).
Comparing the experimental set-up in presented work to that of Dellinger and Vernik (1994), the ratio of the sample height and the transducer width is equal to 3.33 and 3 correspondingly, which demonstrates that the experimental set-up in both studies is very similar. Taking all mentioned aspects into account, the measured first arrivals in presented experiments were considered as a slightly underestimated phase velocity.

3.3.3 Errors estimation

The error (accuracy + precision) for velocity measurements was estimated to be 0.5% in the axial and in the off-axis directions, and 0.3% in the radial direction. The filtering and other post-processing procedures reduce the error by 0.1-0.2%. The difference between two analogue experiments caused by positioning and coupling uncertainties was estimated to be around 1%. In total, I estimate the summarized accuracy (due to the errors in estimation of the sample's lengths and calibration of the electronics) equal to 0.3%

and the summarized precision (due to the errors in picking, positioning and coupling uncertainties) equal to 1%.

3.3.4 Loading path

The samples were loaded in a quasi-static regime. The maximal load was chosen correspondingly to the samples's consolidation. The number of the loading stages defines the sampling rate of the ultrasonic measurements and was designed to provide a necessary density of the data points. The stationarity of each loading stage was controlled by the strain gauges: the loading stage was considered to be quasi-stationary, if the deformation of the sample stopped. In time domain, duration of one loading stage was between 5 and 10 minutes. For example, the loading path of the BaZ sample was as follows: nine loading stages under loading between 1 and 31 MPa. The loading force was measured by the digital measurements cell, mounted into the press.

3.4 Rock samples characterization

This section contains the characterisation of investigated samples and a short description of applied methodologies. Density was determined either by use of Archimedes' principle or by use of the geometrical methodology. For the mineralogical description were performed Scanning Electron Microscope (SEM) and thin section analysis. Investigated samples have different grades of consolidation and were classified as shales and marlstones.

3.4.1 Scanning electron microscope (SEM)

The scanning electron microscope (SEM) is used for the imaging of the material surface at large magnifications. An electron gun placed in a vacuum chamber is used to emit electrons towards the sample. An external magnetic field focuses the emitted electrons onto the investigated area. Some of the electrons are involved in inelastic collusions, where a secondary electron is emitted from the sample. Secondary electrons are detected and used for the construction of the image. An acceleration voltage around 10-30 kV was used. Sample preparation included covering with a gold layer for improving the conductivity. Used equipment was provided by the mineralogical sciences department at the Freie Universitaet Berlin. SEM images were produced for the samples in parallel and perpendicular planes to the layering. The studied parameters potentially influence seismic anisotropy and these parameters are the following: preferred orientation of the minerals, grain packing, grain size, mineralogical content, and cementation.

3.4.2 Density and porosity

In presented thesis the density was determined by either using the Archimedes' principle or the geometrical methodology.
Archimedes' principle (also known as the law of buoyancy) is based on three measurements of the sample's weight: in dry state, in saturated state and being immersed into the fluid (e.g., Mohazzabi, 1997). Obtained weights are used for the calculation of volume, porosity and density.
The geometrical methodology consists of geometrical measurements of the sample's size and weighing of the sample. The volume of the sample is calculated from geometrical size. The density of the sample is then calculated by dividing of the mass on the volume. This methodology is applicable for the studied cylindrical samples (it is applicable for any geometrical shape, which volume can be precisely calculated using geometrical measurements).

3.4.3 Description of the sample BaZ

Based on geological information and visual inspection the sample BaZ was considered as a sample with vertical transversely isotropic (VTI) symmetry. The BaZ sample was extracted from a depth of 3777 meters (Upper Carboniferous). It is a sandy, diagenetically consolidated siltstone (personal communication, Ralf Milke, 2016), see Figure 3.10. The pores and grains both tend to be disc-shaped, with a preferred orientation of the disc planes. The grain size of non-clay minerals is around 100-150 μm, while the width of clay minerals is less than 10 μm and the length is up to 200 μm. Mineralogical composition (quantitative) was determined using electron probe microanalysis (EPMA) methodology. Thin section points count (qualitative technique, using more than 300 points) results in the following mineral content: mica (muscovite) – 33%; quartz – 29%; chlorite – 33% and porosity – 4%. The sample was stored under ambient (laboratory room) humidity conditions over years. The water saturation of the sample was determined by weighing of a dry, room-dry and fully saturated material and is equal to 24%. The porosity and the density were determined by application of the Archimedes' principle: the bulk density is equal to 2720 kg/m^3 and the porosity equals 2.8%. For immersion was used the tap water. The sample has a cylindrical form with a diameter of 50 mm and a height of 59 mm.

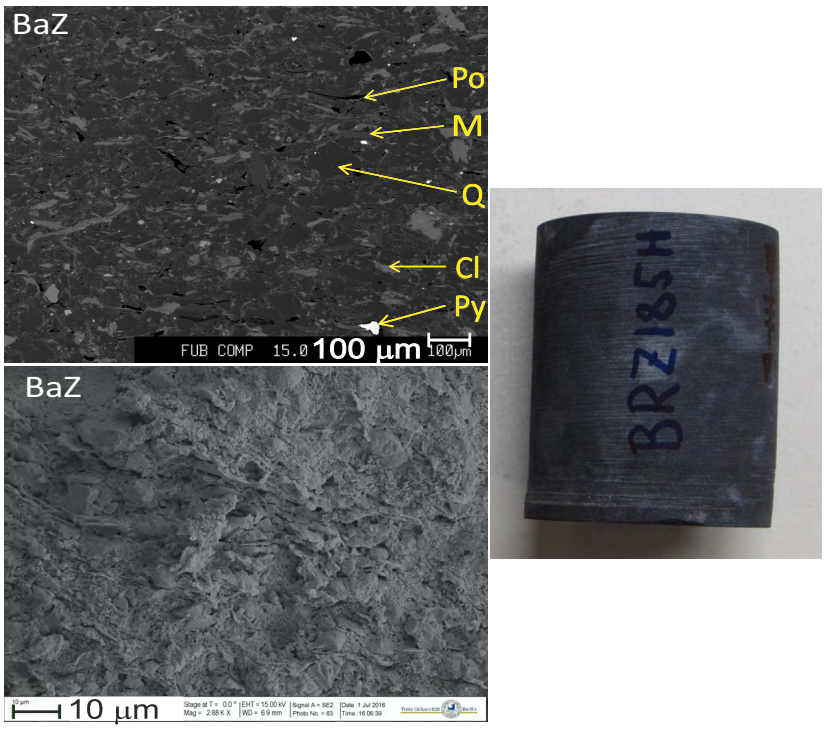

Figure 3.10: *Right: photo of the sample BaZ. Left: scanning electron microscopy (SEM) of the sample BaZ, taken for polished thin section (top) and rough surface (bottom) with 100 μm and 10 μm scale bars respectively. Where, Po -– Pore space (black); M -– Muscovite (medium grey); Q -– Quartz (dark grey); Cl -– Chlorite (light grey); Py — Pyrite (white).*

3.4.4 Description of the sample DH06

After visual inspection and based on knowledge about the formation, the investigated sample DH06 was considered as a VTI sample. It was extracted from a fresh block of the Posidonian Oil formation taken from the Dotternhausen Quarry. By means of EPMA analysis DH06 can be categorized as a clayey bituminous marl, which is supported by an inhomogeneous matrix, see Figure 3.11. Points count analysis of the thin section (using more than 300 Points) provides: quartz – 28%; calcite – 33%; mica (muscovite) – 12%; pyrite – 4% and porosity – 23%. The grain size of non-clay minerals is in the, silt up to sand range ($\approx$ 63 μm), the grain size of clay minerals is less than 10 μm. Total organic content is estimated to be in the range of 9-10 % and the maturity is expected to be low (personal communication, Annette Schmid-Röhl, 2016). Thin section analysis demonstrates that pores and grains both tend to be disc-shaped, with a preferred orientation of the disc planes. The sample is partly saturated, identical to the BaZ sample. The density and porosity measurements were performed following the Archimedes' principle: the bulk density of the sample equals to 2210 kg/m^3 and the porosity equals 12%. The sample has a cylindrical shape, the diameter is equal to 50 mm and the height is equal to 47 mm.

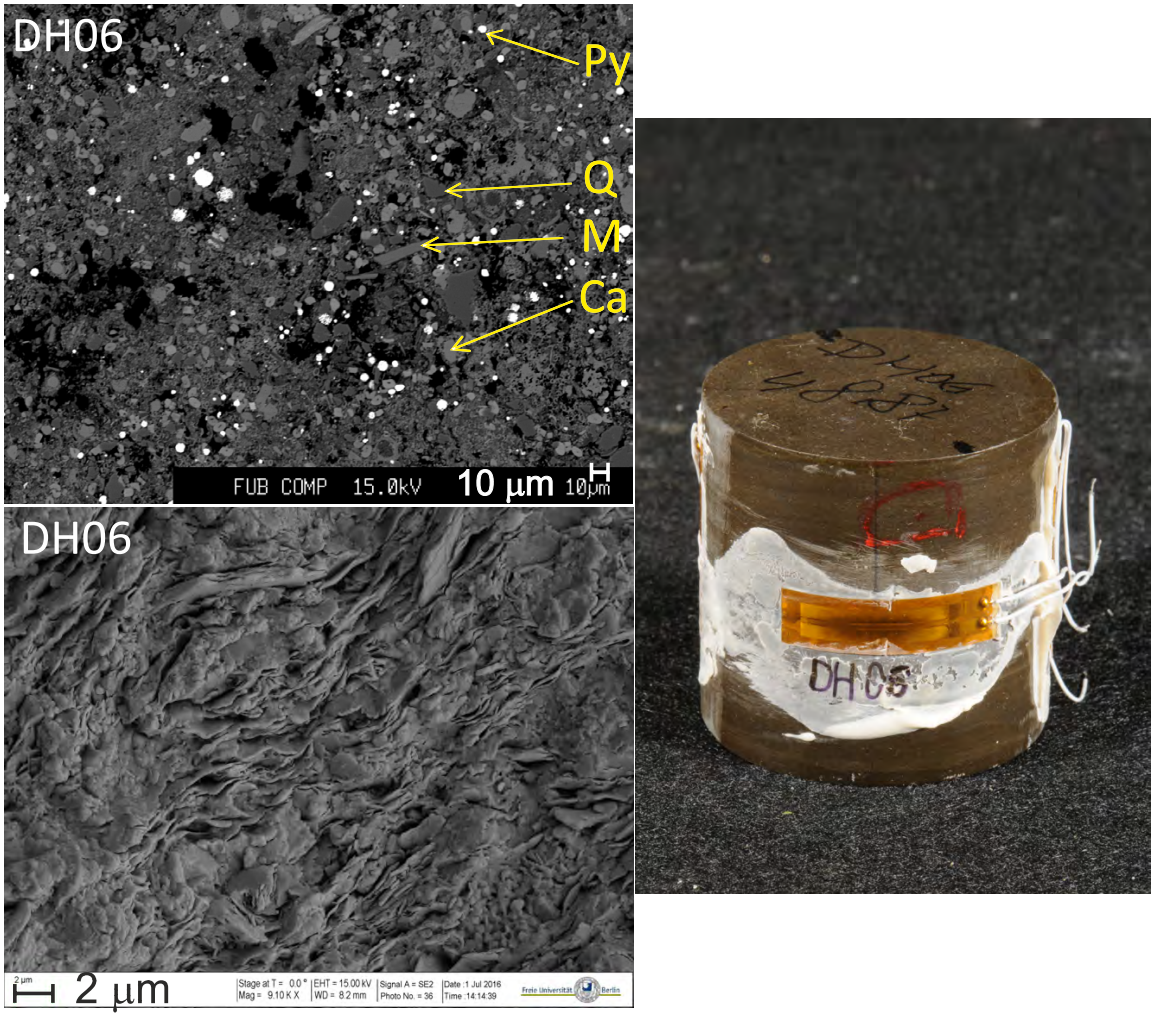

Figure 3.11: *Right: photo of the sample DH06. Left: SEM image of the sample DH06, polished thin section (top) and rough surface (bottom) with 10 µm and 2 µm scale bars respectively. Where, Po -– pore space (black); M -– Muscovite (elongated and grey); Q -– Quartz (dark grey); Ca -– Calcite (light gray); Py -– Pyrite (white).*

3.4.5 Description of the sample DR

Two studied samples were cored out from the same layered marlstone block. The block was extracted from a depth of 4410 meters and belongs to the Upper Cretaceous epoch, Turonian age of the geologic time-scale. First sample was cored perpendicularly to the layering and the second sample was cored parallel to the layering, which produces visually VTI and HTI samples. Further ultrasonic measurements verified the VTI elastic symmetry of the former and revealed an orthorhombic elastic symmetry for the latter sample. To determine the VTI symmetry of the first sample, was performed an additional measurement series including 18 measurements in 5 different directions within the symmetry plane parallel to the layering. As expected, the observed velocities show similar values: the maximal velocity deviation, compared to the measured averaged velocity, equals 0.3% and the average velocity deviation, compared to the averaged velocity, equals 0.1%. These deviations are within the measurements error and clearly indicate the VTI symmetry of the sample. Both samples belong to the same core and have a nine centimetre interval between them. Taking into account the genesis of the sediments, samples may have differences in their layering and correspondingly in their porosity structure. Both samples have similar mineralogy, the dominant non-clay grain size is around 100 μm and the most common mineral is quartz, see Figure 3.12. The width of clay minerals is less than 1 μm and the length is up to 10 μm. The primary pore space was particularly filled by a fine-grained quartz. The silicified fossils are embedded in the siliceous cement. The grains and pores both tend to be disc-shaped. Both of them have a preferred orientation of the disc planes. Mineralogical composition (qualitative) was determined using electron probe microanalysis (EPMA) methodology. Thin section point count (quantitative technique, using more than 300 points) yields following mineral content: quartz – 55%; feldspar – 32%; mica – 6%; pore space – 4%; iron carbonate – 3%. The sample had been stored under an ambient (laboratory room) humidity rate of 50% for many years. The water saturation of the sample was determined by weighing of the dry, room dry and fully saturated material and is equal to approximately 42%. The porosity and density were determined by use of the Archimedes' principle: the bulk density is equal to 2520 kg/m^3 and the porosity equals 5%. For the immersion was used the tap water. Geometrically, both samples have an identical cylindrical form with 60 mm height and 50 mm diameter.

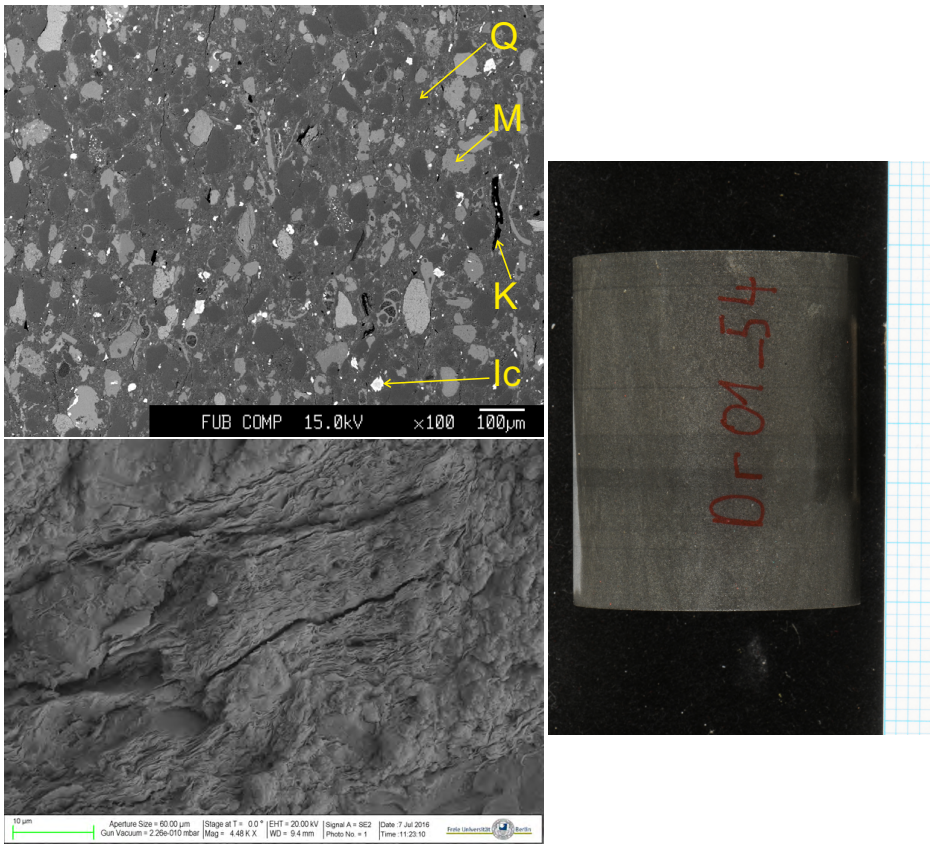

Figure 3.12: *Right: photo of the sample DR. Left: SEM image of the sample DR, polished thin section (top) and rough surface (bottom) with 100 µm and 10 µm scale bars respectively. The main minerals are indicated as: Q – quartz (medium grey), M – mica (light grey), K – kaolinite (black), Ic – iron carbonate (white).*

Chapter 4

Measurement results: uniaxial loading

4.1 Deformations

Information about the sample's deformation under stress is important for the following reasons: calculation of the true travel path of the seismic wave; mechanical hysteresis; (non)linearity of the stress-deformation relation. Deformations were measured in the axial and radial directions.

4.1.1 VTI sample BaZ

In the axial direction, a maximal strain of 0.08 % was observed. In the radial direction, measured strain is four times smaller and equals to to 0.02 % (see Figure 4.1). The absolute strain value in the axial direction is indicated by the blue curve, strain in the radial direction is displayed as a green curve. Both curves show the loading cycle starting from zero stress and the unloading cycle starting from the maximum stress value. Observed hysteresis is not significant. Both strain curves have a nearly linear shape. Using strain was calculated velocity overestimation (seismic wave travel path is changing with the sample deformation). At maximum measured 46 μm strain, the velocity overestimation is around 0.07%. This value is negligibly small and therefore the measured velocities were not recalculated. The volumetric change of the sample was calculated using the measured deformations and is equals 0.04 %. This change is related to the change of pore space.

4.1.2 VTI sample DH06

Deformations measured by the strain gauges in a stress area up to 13 MPa demonstrate the following: sample shortening in the axial direction equals to 0.13%, while sample expansion in the radial direction is around 0.01%. The corresponding velocity overestimation, caused by sample shortening, is up to 0.13% and must be considered as a significant systematic error. This effect was compensated by recalculations of the velocities. From the measured strain was computed volumetric change of the sample, which is connected to the alteration of porosity and results in 0.1 %. Strain measurements show a hysteresis effect during loading and unloading cycles, which is an indication of inelastic deformation. The shape of the deformation versus stress curve is non-linear (see Figure 4.2). This demonstrates a significant creep effect.

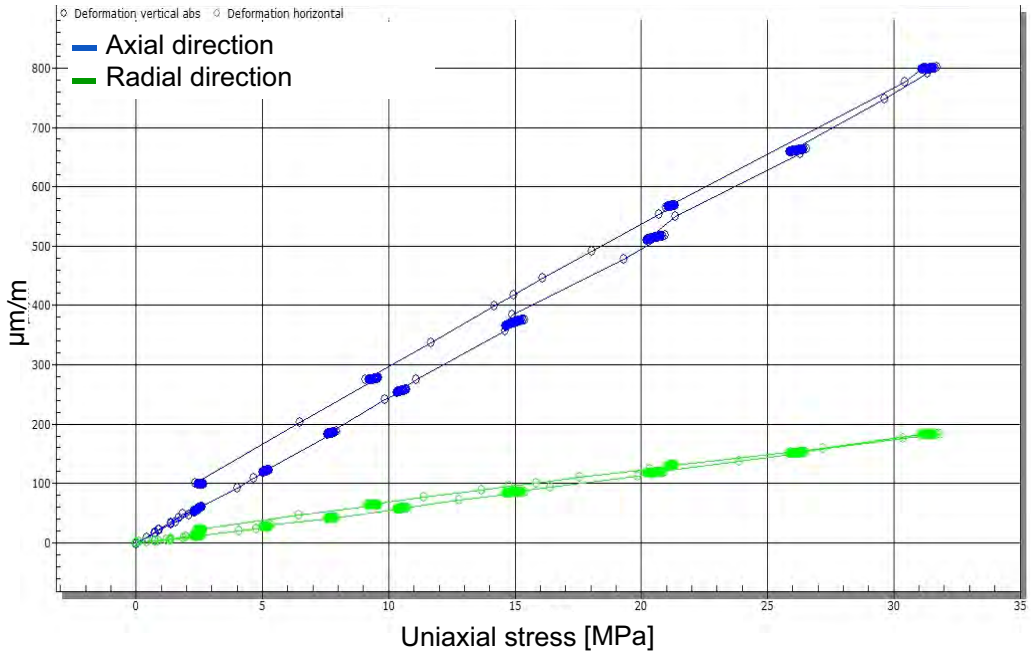

Figure 4.1: *BaZ - VTI sample. Strain as a function of stress. Blue – strain in the axial direction. Green – strain in the radial direction*

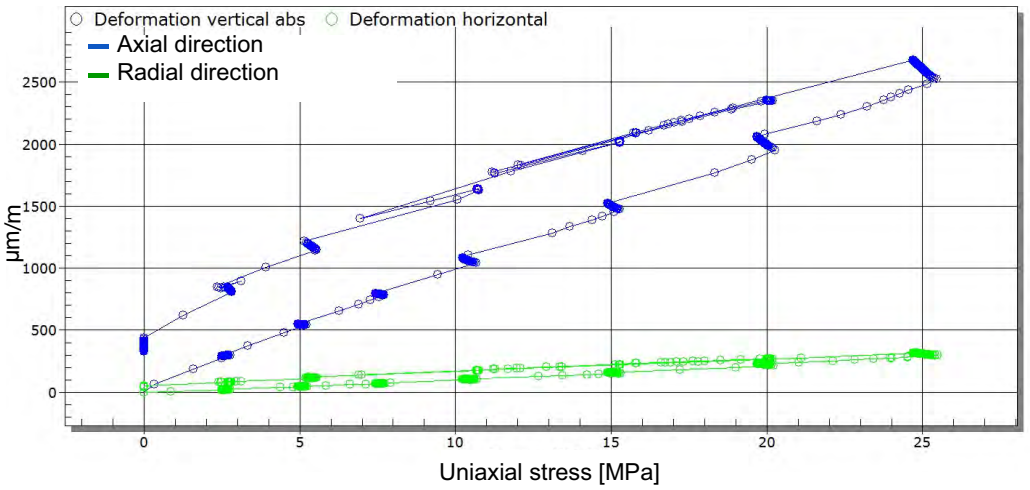

Figure 4.2: *DH06 - VTI sample. Strain as a function of stress. Blue – strain in the axial direction. Green – strain in the radial direction*

4.1.3 VTI and orthorhombic samples DR

DR-VTI: measured strain does not exceed 0.06% and therefore, the influence of sample shortening on the velocity measurements can be neglected. Using measured deformations was estimated volumetric change of the sample, which is dependent on the alteration of the pore space and is equal to 0.04%. The stress-strain curve has a nearly linear shape, see Figure 4.3, top.

DR-orthorhombic: deformation measurements provided by strain gauges result in sample shortening in axial direction of 0.06% and the sample expansion in radial direction of 0.01%. Therefore, sample deformation does not significantly influence the results of ultrasonic velocity measurements and can be neglected. The sample deformation is almost identical to the VTI sample and leads to an identical volumetric shrinkage of 0.04%. The stress-strain curve has nearly linear shape and non-significant hysteresis, see Figure 4.3, bottom.

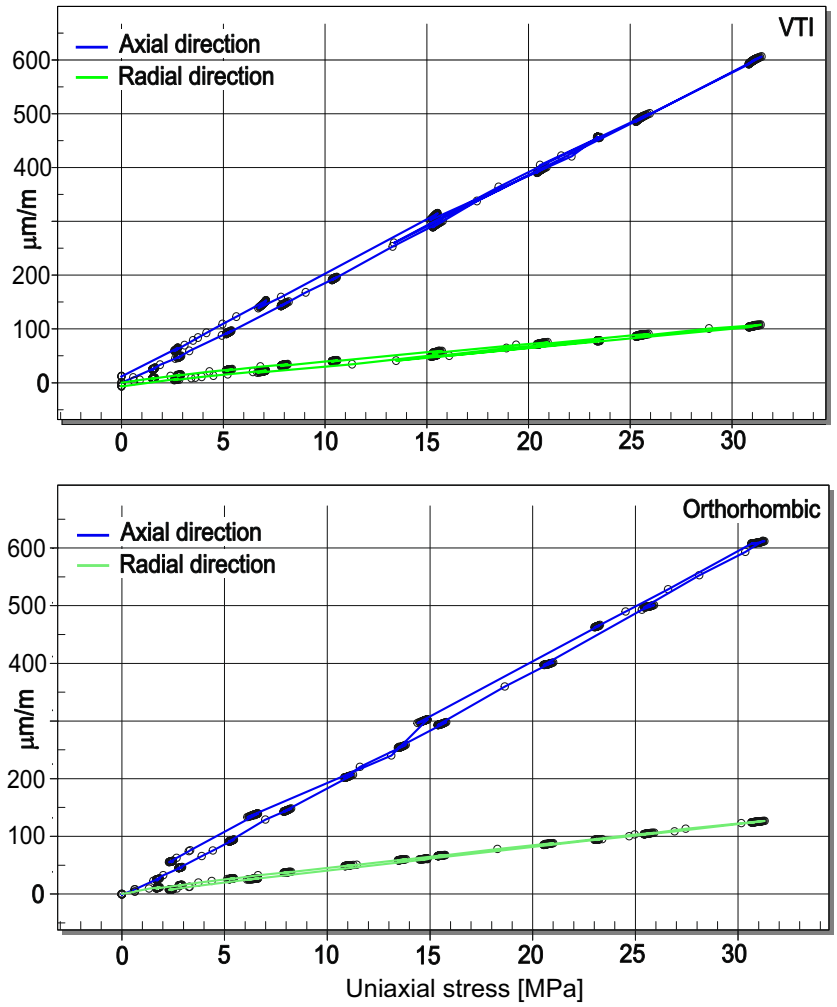

Figure 4.3: *Strain as a function of stress. Top: DR - VTI sample. Bottom: DR - orthorhombic sample. Blue line – strain in the axial direction. Green line – strain in the radial direction.*

4.2 Ultrasonic velocities

4.2.1 VTI sample BaZ

A significant velocity increase was observed in the axial direction (loading direction). The velocity of the P-wave P_{33} (propagated in the axial direction) increases by 119 m/s or 2.5%, see Figure 5.12. The velocity of the S-wave S_{31} rises significantly by 54 m/s or 1.9%. Both stress-velocity curves have a non-linear shape.

Velocity change in the radial (orthogonal to the loading) direction is not significant. The velocity of the P-wave P_{11} displays a small increase by 22 m/s or 0.4%. The velocity of the S-wave S_{21} increases slightly by 12 m/s or 0.4%, see Figure 5.12.

Off-axis quasi P-wave velocity measured at an angle of 64° to the symmetry axis P_{44} shows a small increase of about 35 m/s or 0.7%.

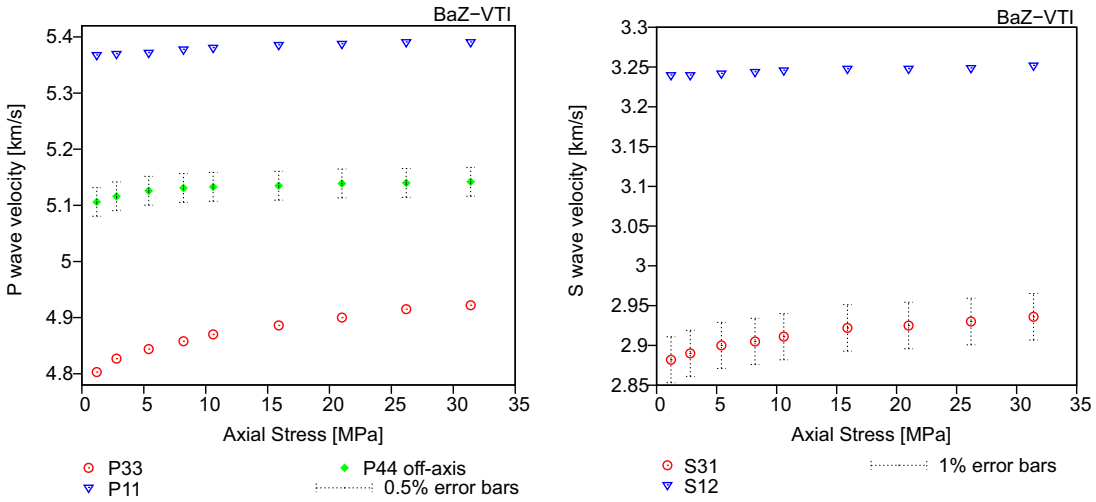

Figure 4.4: *BaZ-VTI sample. Stress dependency of ultrasonic velocities. On the left: P-wave velocities. On the right: S-wave velocities.*

Interpretation of the measured data

Anisotropy parameters ε and γ systematically decrease under uniaxial loading, while η and δ do not show any clear trends (see Figure 4.5). A rather uncommon negative δ is observed by the direct laboratory measurements. Anellipticity parameter η displays some changes, but fluctuates around a constant value. Demonstrated trends confirm (significant) influence of uniaxial stress on the elastic properties exclusively in the direction of the stress application.

4.2.2 VTI sample DH06

A significant increase of P- and S- wave velocities in the axial (loading) direction is demonstrated. P_{33} increases by 170 m/s or 5.8%, while S_{31} rises by 48 m/s or 2.5%, see Figure 4.6. The shape of the stress-dependent velocities is non-linear.

In the radial direction are observed nearly unchanged velocities. P_{11} increases by 7 m/s or 0.2 % and S_{12} rises by 17 m/s or 0.7 %. These changes cannot be considered as notable increase.

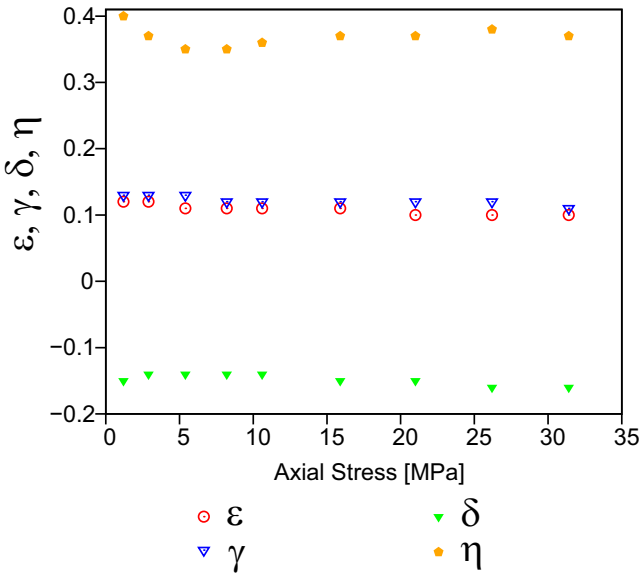

Figure 4.5: *BaZ-VTI sample. Stress dependency of anisotropy parameters.*

Off-axis quasi P-wave velocity P_{44} could not be measured directly due to the sample geometry (did not fit the measurements cell) and was estimated theoretically, using the so called constant anellipticity approach (see Section 2.6).

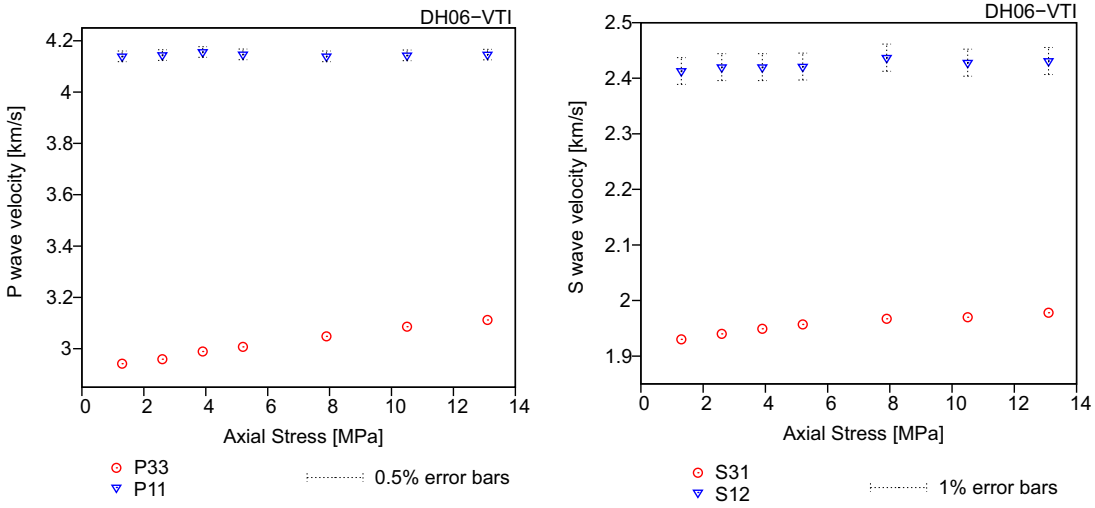

Figure 4.6: *DH06-VTI sample. Stress dependency of ultrasonic velocities. On the left: P-wave velocities. On the right: S-wave velocities.*

Interpretation of the measured data

Sample DH06 demonstrates a significant initial anisotropy: $\varepsilon = 0.49$ and $\gamma = 0.28$, see Figure 4.7. However, anisotropy parameters rapidly decrease during the uniaxial loading: ε by 21 % and γ by 9% with respect to the initial value. The rather large anisotropy and its stress sensitivity may relate to the high porosity of 12% and a substantial total organic content of 9-10 % (personal communication, Annete

Schmid-Röhl, 2016). Anisotropy parameters δ and η could not be determined directly from the experimental data due to the absence of measured off-axis velocity P_{44}. These parameters were estimated using the so called constant anellipticity approach (see section 2.6). Laboratory observations show significant change of elastic parameters exclusively in the direction of uniaxial loading.

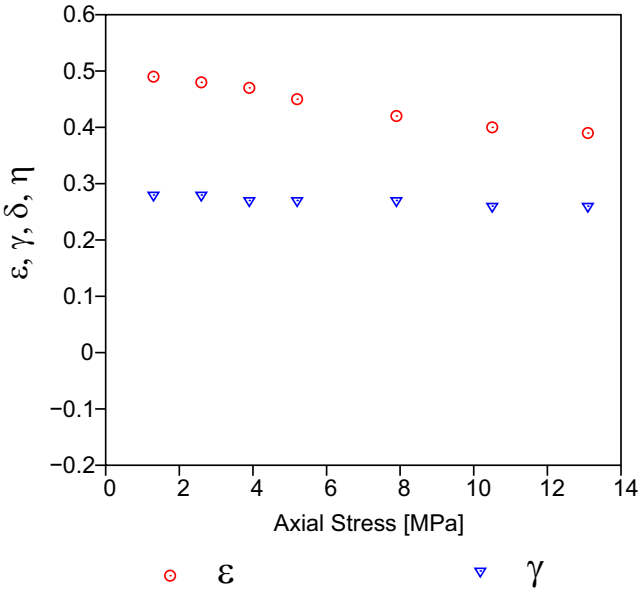

Figure 4.7: *Sample DH06 VTI. Stress dependence of anisotropy parameters.*

4.2.3 VTI sample DR

The stress-velocity curves show relatively linear trends. The maximum velocity increase is observed in the axial (loading) direction for both P_{33} and S_{31}, see Figure 4.8. P_{33} increases by 164 m/s or 3.4% and S_{33} rises by 27 m/s or 0.9%.
Stress dependency of velocities in the radial direction is rather non-significant. The P_{11} and S_{21} change lies in the error margin. The off-axis velocity P_{44} increases moderately by 55 m/s or 1.1%.

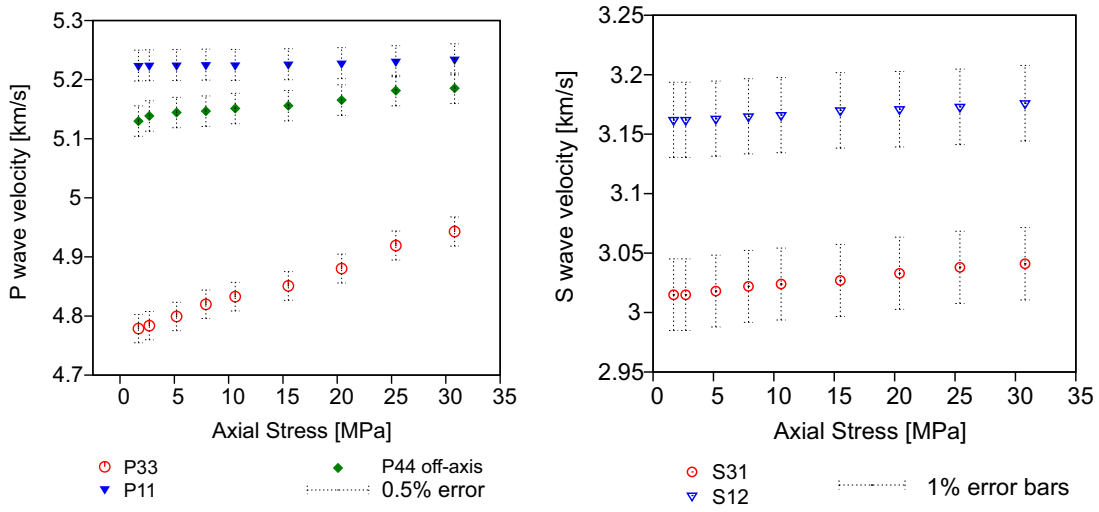

Figure 4.8: *DR-VTI sample. Stress dependency of ultrasonic velocities. On the left: P-wave velocities. On the right: S-wave velocities.*

Interpretation of the measured data

The anisotropy parameters decrease relatively to the initial value. The pre-stressed ε equals to 0.1 and decreases by 38% during loading, initial γ equals 0.05 and decreases by 9%, initial δ equals 0.08 and decreases by 9% with respect to the initial value, see (Figure 4.9). Generally, observed anisotropy is weak and the anellipticity parameter η fluctuates around zero. In other words, a nearly elliptical medium is observed.

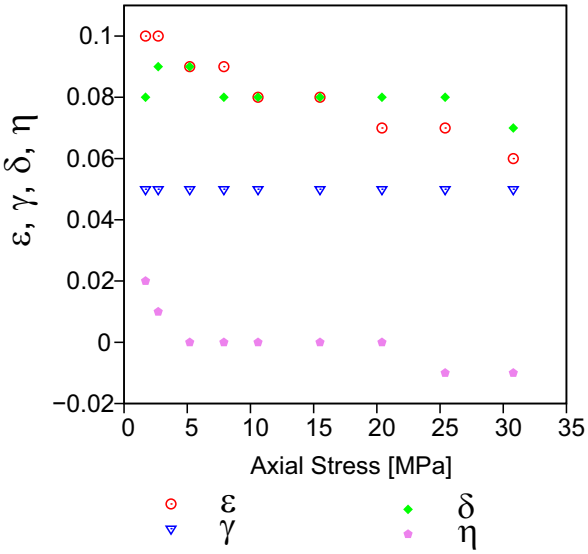

Figure 4.9: *Sample DR VTI. The dependence of the anisotropy parameters on stress.*

4.2.4 Orthorhombic sample DR

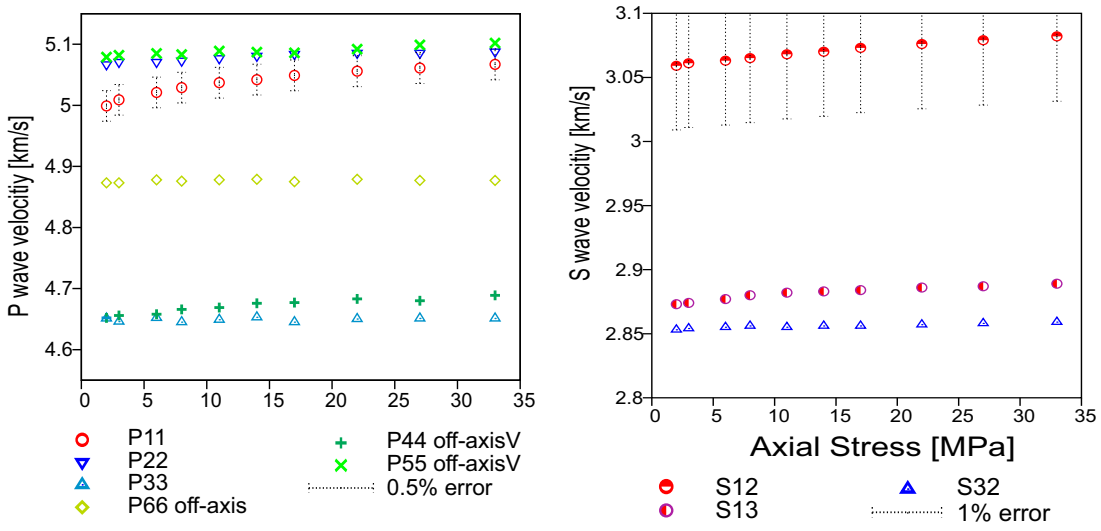

Figure 4.10: *DR-HTI sample. Stress dependency of ultrasonic velocities. On the left: P-wave velocities. On the right: S-wave velocities.*

Ultrasonic measurements demonstrate that the stress-dependent velocity change is influenced by two factors: the direction of the uniaxial stress application and the orientation of the bedding. The greatest P- and S- wave velocity increase is observed in the axial (loading) direction, see Figure 4.10. S-wave velocities in the axial direction demonstrate shear wave splitting: polarized parallel to the layering S_{12} is faster than polarized perpendicular to the layering S_{13}. An interesting observation is that velocity polarized parallel to the layering direction S_{12} is, apparently, slightly more stress sensitive than the velocity polarized perpendicular to the layering direction S_{13}.

In the radial direction, the velocity of the P-wave propagated parallel to the layering P_{22} is faster than the P-wave velocity measured perpendicular to the layering P_{33}, but both P-wave velocities do not show a significant increase during the stress application, see Figure 4.10. S-wave velocity observed in the radial direction and polarized in the axial direction S_{21} shows a similar trend as S_{12} (as theoretically expected), but shows a minor systematic shift caused by the different ray path and shale's sample inhomogeneity. The velocity of the S-wave propagated in the radial direction and polarized horizontally S_{32} is slower than S_{21} and does not demonstrate any significant stress dependence.

In an unloaded state, the velocity of the off-axis qP-wave P_{44} propagated in the direction perpendicular to the layering has the same velocity as the P_{33}. Unlike the radial velocity, P_{44} demonstrates a moderate increase during the stress application. In an unloaded state, the velocity of the off-axis qP-wave P_{55} is nearly equal to the P_{22}. During the loading P_{55} rises moderately. The velocity of the off-axis qP-wave P_{66} propagated in the radial direction under the angle of 45° to the two axial symmetry planes is almost stress-independent. In an unloaded state, P_{66} is approximately the average between P_{22} and P_{33}.

Interpretation of the measured data

The observed anisotropy parameters ε_1 and ε_2 increase during the stress application, see Figure 4.11. ε_1 (related to the two radial velocities P_{22} and P_{33}) increases by 5% with respect to the initial value. This increase displays a non-significant change of the radial velocity parallel to the layering. Anisotropy parameter ε_2 (related to P_{11} and P_{33} velocities) rises by 20% and displays a significant increase of the axially propagated velocity.
The anisotropy parameters γ_1 and γ_2 increase similarly to ε. γ_1 (related to the two differently polarized axial S-wave velocities) increases by 3%, with respect to the initial value. This indicates that the axially propagated S-wave with polarization parallel to the bedding S_{12} is slightly more stress sensitive, than S-wave propagated in the axial direction and polarized perpendicular to the bedding S_{13}. γ_2 (related to the "fast" axial S_{12} and "slow" radial S_{32} S-wave velocities) increases by 8% and indicates the stress sensitivity of the axially propagated S-wave.
The three anisotropy parameters related to the off-axis velocities δ_1, δ_2 and δ_3 do not show a distinct stress sensitivity, see Figure 4.12. Stress-dependent changes are below 0.04: δ_1 remains unchanged, δ_2 slightly increases and δ_3 slightly decreases. These non-significant changes lie within the error margins. η do not demonstrate any pronounced trends with significant amplitudes, see Figure 4.12. Measured velocities and anisotropy parameters correspond to the seismically orthorhombic medium.

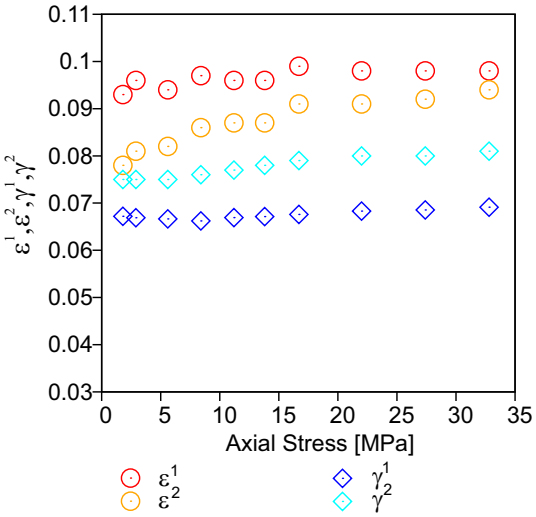

Figure 4.11: *Sample DR HTI. Stress dependency of Epsilon and Gamma parameters.*

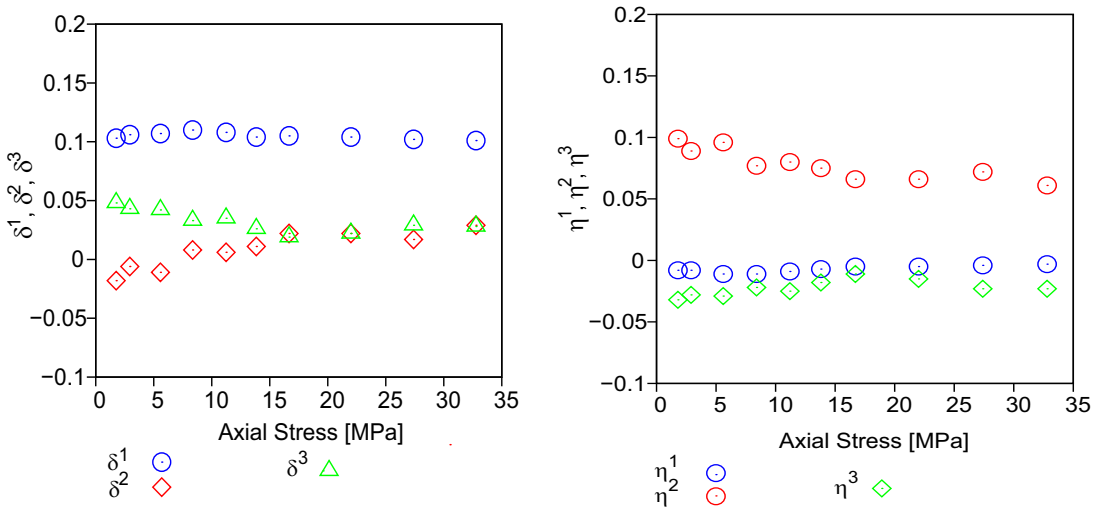

Figure 4.12: *DR-HTI sample. Stress dependency of Delta and Eta parameters.*

4.3 Application of the constant anellipticity approach

Here, is applied the constant anellipticity approach (CAN) on the laboratory data. First, is described the application on the complete data set of BaZ-VTI and the experimentally determined off-axis velocities are compared to the theoretically estimated ones. Secondly, the CAN is applied on the incomplete uniaxial data set of DH06-VTI, and on the incomplete triaxial data set of HR1-VTI. This is done in order to estimate the off-axis velocity. The estimated off-axis velocity is used to complete the experimental data set. For the theoretical background see section 4.3.

4.3.1 Complete uniaxial data set BaZ-VTI

For verification of the CAN is used a complete data set of BaZ-VTI, obtained in the laboratory. The off-axis velocity P_{44} (measured at 64° inclination to the symmetry axis) is compared with two theoretical estimations. First, the CAN was applied using one measured off-axis velocity value in the unloaded state $P(0)$ as the input data, the result is indicated as $P_{44}\ CAN\ P(0)$ (see Figure 4.13). The stress-dependent change has a similar shape for measured and modeled data with a maximum residuum of 0.2%. Secondly, the CAN was applied using empirical Ryan-Grigor formula, the output is displayed as $P_{44}\ CAN\ R.G.$. The analytically solved velocities show a systematic shift of 2.3% with respect to the measured velocities. This systematic error is a consequence of the initial velocity estimation using formula 2.58.

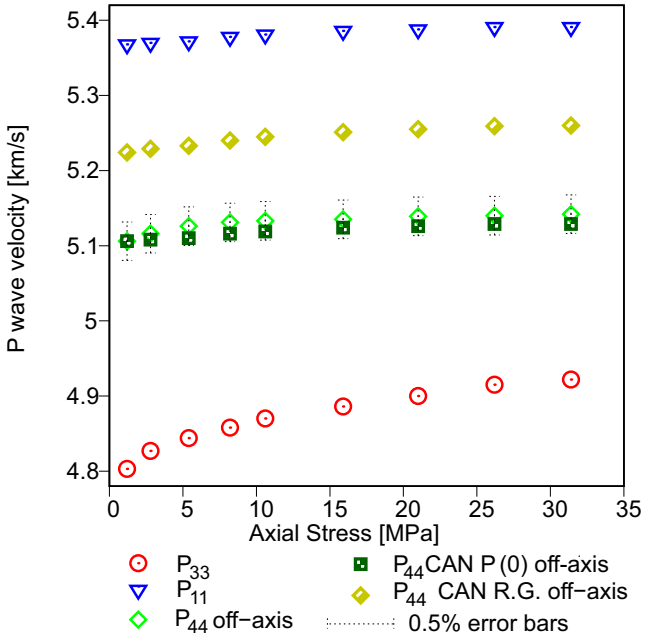

Figure 4.13: *Sample BaZ-VTI. Stress dependence of ultrasonic velocities. Application of the CAN approach. Off-axis P_{44} velocity measured at an inclination of 64° to the symmetry axis.*

Literature data

For the examination of the CAN on the literature data was chosen a data set published by Hornby (1998) (Jurassic shale). Estimated off-axis velocities show a similar trend as the measured ones and the maximal residual equals to 2.1%. Application of the formula 2.58 results in an additional shift of 1%.

4.3.2 Incomplete uniaxial data set DH06-VTI

The data set obtained in the laboratory is incomplete due to the technical difficulties. The CAN was applied to complete the data set, see Figure 4.14. The resulted curve demonstrates realistic shape and velocities and is representative for the considered sample. The completed data set was used for the further research.

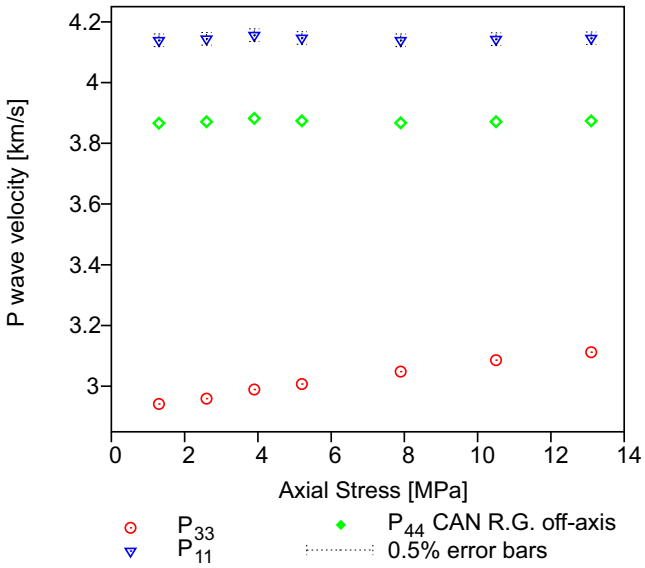

Figure 4.14: *Sample DH06-VTI. Stress dependence of ultrasonic velocities. Application of the CAN approach. Estimated off-axis P_{44} velocity measured at an inclination of 64° to the symmetry axis.*

4.3.3 Incomplete triaxial data set HR1-VTI

The triaxial data sets are incomplete due to the absence of the measured off-axis velocities. Measurement of the off-axis velocities was technically difficult, due to the experimental setup. The CAN was applied, in order to complete the data, see Figure 4.15. The estimated off-axis velocity shows realistic values and a consistent trend. Obtained information was further used for the theoretical modelling.

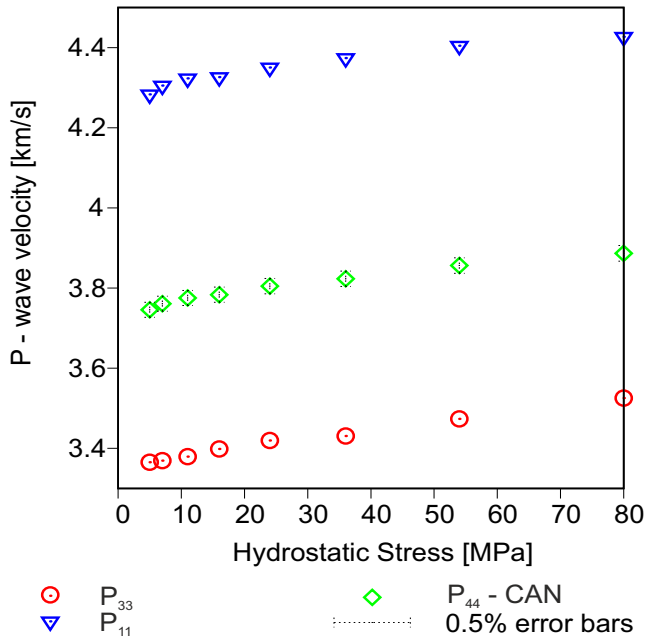

Figure 4.15: *Sample HR1-VTI. Stress dependence of ultrasonic velocities. Application of the CAN approach. Estimated off-axis P_{44} velocity measured at an inclination of 45° to the symmetry axis.*

Chapter 5

Application of the porosity deformation approach

Abstract

In this section is described application of the porosity deformation approach (PDA) to the experimentally obtained data. This enables a direct comparison of laboratory measurements with the numerical modelling for validation and further analysis. As intermediate product were obtained and compared experimentally measured and theoretically modeled compliance tensors, ultrasonic velocities and anisotropy parameters. The modelling of the orthorhombic medium is carried out using equations set 2.53 and modelling of the VTI medium performed using equations set 2.50. Theoretical background and a description of the PDA can be found in section 2.5.

For the sake of simplicity the data bank is divided in two parts and described separately. The first part includes two VTI shales: BaZ-VTI and DH06-VTI. They are compared and analyzed. Based on this the general trends are described for uniaxially loaded VTI samples. An individual influence of the mineralogical composition and genesis on the stress sensitivity is analyzed. In the second part are compared two samples with similar mineralogy but with different anisotropy: one sample has a VTI symmetry (DR-VTI) and another sample is seismically orthorhombic (DR-ORT). Their stress-dependencies are compared and the influence of uniaxially applied stress is described, taking into account orientation of the layering.

Algorithm

The porosity deformation approach is designed for the application on the complete data set of stress-dependent elastic constants. Below, is shown the algorithm of the procedure:

1. Computation of the stress-dependent compliance tensor based on measured velocities
2. Modelling of the stress-dependent compliance tensor, using PDA
3. Comparison of measured and modelled compliances and ultrasonic velocities

5.1 VTI sample BaZ

In this section the PDA is applied to the complete data set of a VTI sample under uniaxial loading. Moreover, is estimated the influence of the stiff porosity deformation on the elastic properties of the sample. For this purpose the modelling was performed two times: once with taking into account the deformation of stiff porosity, and once without (see equation 2.51). In this particular modelling the non-diagonal elements of the compliance matrix S_{13} and S_{12} are assumed to be constant, for more details see Ciz and

Shapiro (2008).

Results of both modelling steps (with and without stiff porosity) do not exhibit major differences, which implies that stiff porosity has no significant influence. In terms of compliance, obtained results demonstrate significant change of only two independent elements of the compliance tensor: S_{33}^{dr} and S_{44}^{dr}. The compliance S_{11}^{dr}, S_{66}^{dr} and S_{13}^{dr} do not show significant change, see Figure 5.1. The shape of compliance change versus uniaxial stress has a non-linear form. The UNE algorithm provides a slightly better fit of S_{44}^{dr}. The compliant porosity was estimated using equation 2.54 and results 0.02 %.

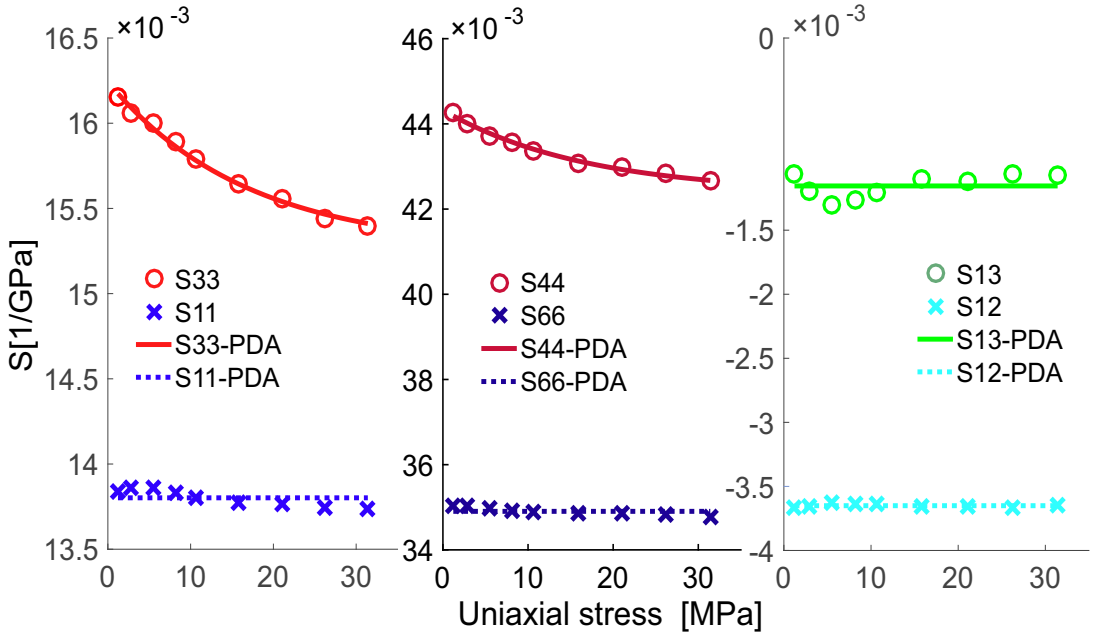

Figure 5.1: *Sample BaZ-VTI. Components of the compliance tensor versus the uniaxial stress. Points indicate experimentally determined values, lines display the data obtained by the PDA approach.*

In the final stage, the velocities were calculated from the modeled compliance tensor. Theoretically computed velocities corresponded well with the experimentally measured ones: all trends coincide and the maximal discrepancy equals 0.4 % (see Figure 5.2, 5.3).

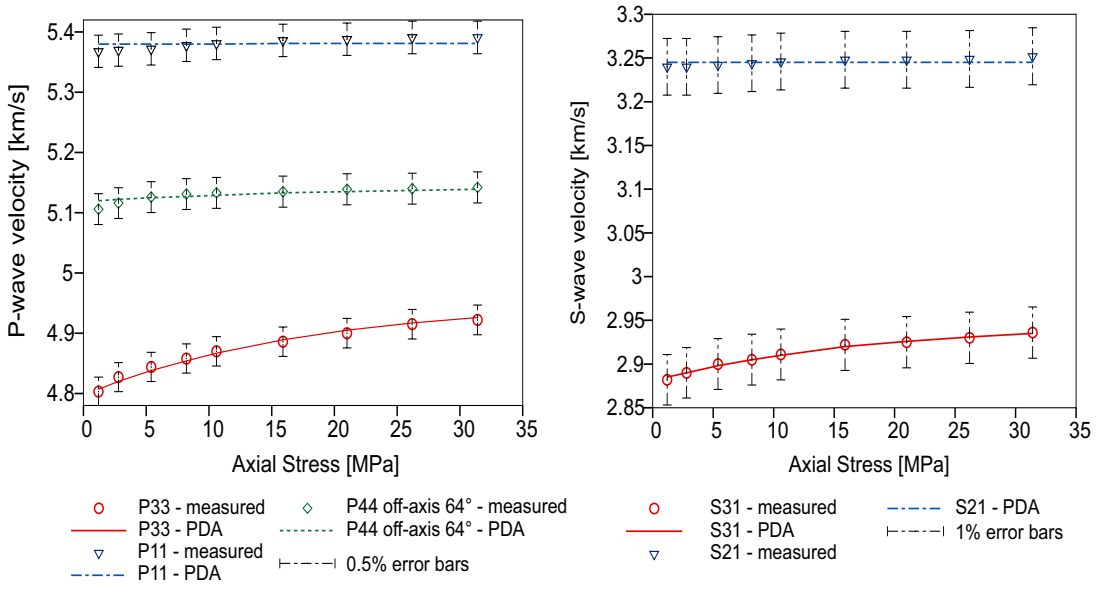

Figure 5.2: *Sample BaZ-VTI, ultrasonic velocities as function of the uniaxial stress. Points indicate experimentally observed velocities, lines represent velocities modeled with the PDA approach, see Figure 5.1.*

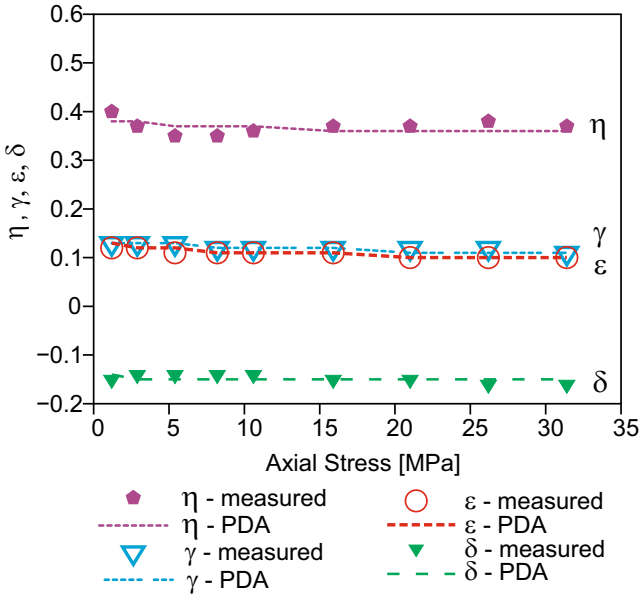

Figure 5.3: *Sample BaZ-VTI, anisotropy parameters as function of the uniaxial stress. Points indicate experimentally observed values, lines represent anisotropy parameters modeled with the PDA approach, see Figure 5.1.*

5.2 VTI sample DH06

The PDA was applied on the incomplete data set of a VTI sample DH06. In this particular case the non-diagonal elements of the compliance matrix S_{13} and S_{12} were assumed to be constant, for more details see Ciz and Shapiro (2008). The off-axis velocity P_{44} was not measured directly but estimated by use of the constant anellipticity approach (CAN), see section 2.6.

Similarly to the BaZ sample, only two independent components of the compliance matrix S_{33}^{dr} and S_{44}^{dr} show a significant decrease (see Figure 5.4), while S_{11}^{dr}, S_{66}^{dr} and S_{13}^{dr} do not demonstrate any pronounced trends. The compliant porosity was calculated using formula 2.54 and equals to 0.13 %.

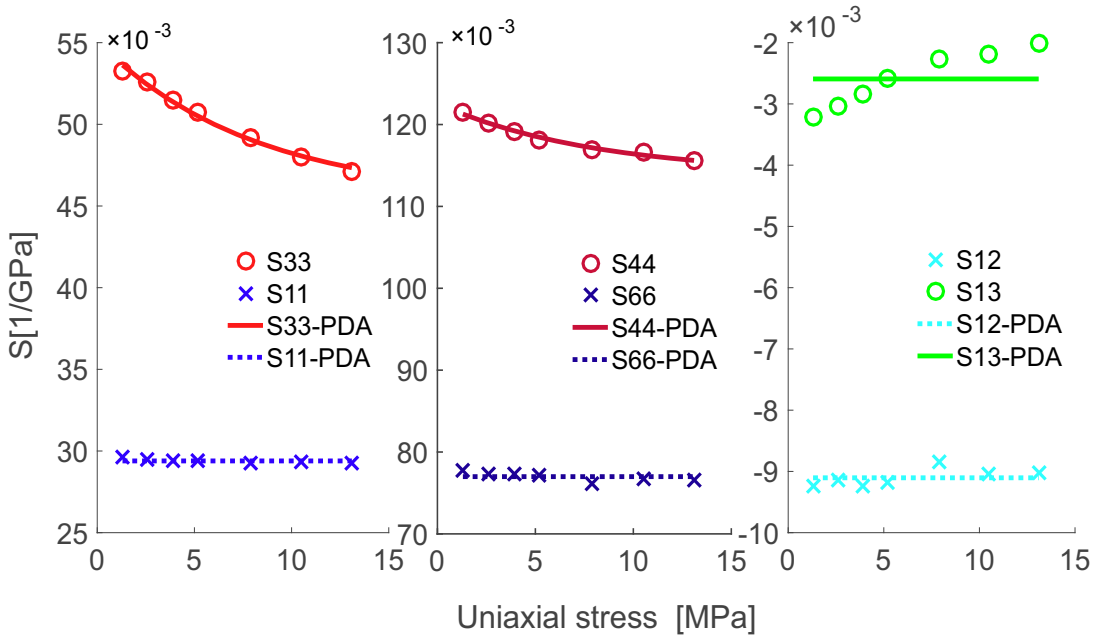

Figure 5.4: *Sample DH06-VTI. Components of the compliance tensor versus the uniaxial stress. Points indicate experimentally determined values, lines display the data obtained by the PDA approach.*

The seismic velocities were calculated from the modeled compliance tensor. Velocities obtained by PDA are in good agreement with the experimentally measured ones: all trends coincide and the maximal discrepancy is equal to 0.2 % (see Figure 5.5).

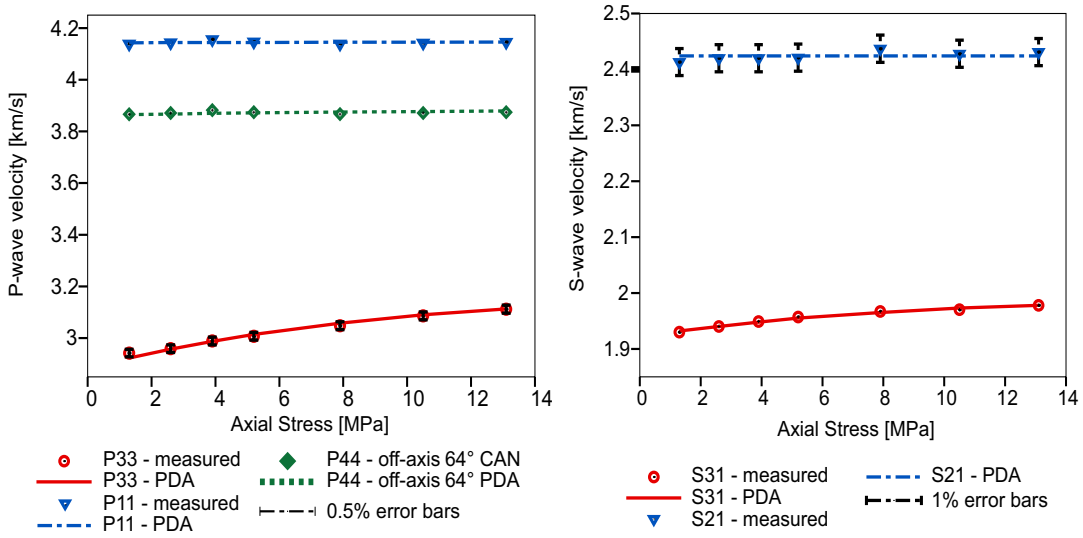

Figure 5.5: *Sample DH06-VTI. Ultrasonic velocities as function of the uniaxial stress. P44 off-axis 64° CAN was obtained using the constant anellipticity approach including Ryan Grigor's empirical formula. Points indicate experimentally observed velocities, lines represent velocities modeled with the PDA approach, see Figure 5.4.*

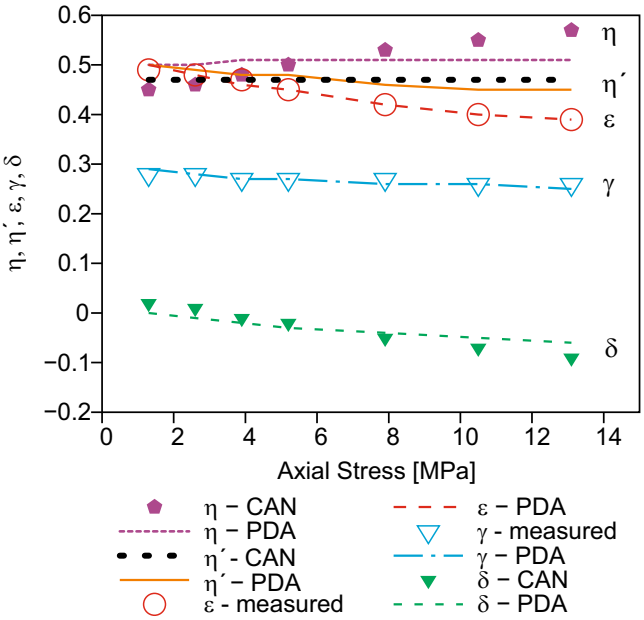

Figure 5.6: *Sample DH06-VTI, anisotropy parameters as function of the uniaxial stress. Points display experimentally observed values, lines represent anisotropy parameters modeled with the PDA approach, see Figure 5.4.*

Discussion: VTI samples BaZ and DH06

Similar trends were observed for both studied VTI shale samples:

- Strain measurements show a hysteresis effect during loading and unloading cycles,
- shapes of the stress-dependent velocities and deformations have a non-linear form,
- estimated by the PDA (see equation 2.50) influence of the stiff pore space deformation is negligibly small.

These observations can be explained by the assumption that the stress-dependent change of elastic parameters is mainly driven by the compliant pore space deformation. The observed hysteresis is possibly related to the irreversible close of a portion of the compliant pores. It is important to take into account the duration of presented experiments, which varies from 3 to 6 hours.

The non-linearity of the stress-dependent velocities and the strain is an indirect indication of the compliant porosity effects: compliant pore space closes rapidly during the first loading steps and at a certain stress level it is almost completely closed. Above this stress level only the stiff porosity can be deformed and the stress dependencies approach a linear form. Numerical modelling showed that the contribution of the linear term in equation 2.50 is negligible.

Compliant porosity estimated by the PDA (see equation 2.54) is equal to 0.02 % and 0.13 % for the BaZ and DH06 samples correspondingly, while the volumetric change of the pore space measured by strain gauges results 0.04 and 0.1 %. The numbers are close and indicate a good estimation. The change of the porosity (measured by strain gauges) was calculated with an assumption that all deformations in the sample are exclusively due to the pore space deformation. The discrepancy may be related to the measurements precision, or to the different stress distribution across the areas measured using ultrasonic experiments and across the areas measured using strain gauges.

Observations on the sample DH06 demonstrate an element of compliance tensor S_{13}^{dr}, which shows some non-significant increase. This may be caused by the fact that the off-axis velocity was not measured experimentally but estimated theoretically using the CAN approach. Measurements on the sample BaZ do not demonstrate any significant dependence of S_{13}^{dr} on the stress. Therefore, I refrain from considering S_{13}^{dr} as a significantly changed parameter for the time being, but I look forward to the next set of precise experimental data.

Conclusions: VTI samples BaZ and DH06

Under uniaxial loading conditions both VTI samples demonstrate the following trends, which may indicate a general tendency for VTI shales:

- The change of elastic constants is controlled mainly by the deformation of compliant porosity,
- the significant change is observed for only two independent elastic constants: S_{33}^{dr} and S_{44}^{dr},
- a non-significant change of the other three independent elastic constants: S_{11}^{dr}, S_{66}^{dr} and S_{13}^{dr}.

5.3 VTI sample DR

The application of the PDA approach is analyzed in terms of the compliance tensor. The modelling reveals significant change of two diagonal components of the compliance tensor: S_{33} and S_{44}, see Figure 5.7. The other three independent constants of the compliance tensor S_{11}, S_{66} and the non-diagonal S_{13} demonstrate moderate alteration. The shape of stress-compliance curve has a nearly linear form for all components of the compliance tensor, which corresponds to the observed, nearly linear stress-velocity dependencies, see Figure 5.8. The modelling coefficient K_{ijkl}^{3} plays a considerable role and contributes to the accurate modelling of the non-diagonal component S_{13} and the diagonal elements S_{11} and S_{66}, see

Table B.3. The coefficient B_{33} is very small and effectively equal to zero, which means that the compliant porosity is negligible. This indicates the influence of the stiff porosity deformation as significant and the influence of the compliant porosity deformation as insignificant.

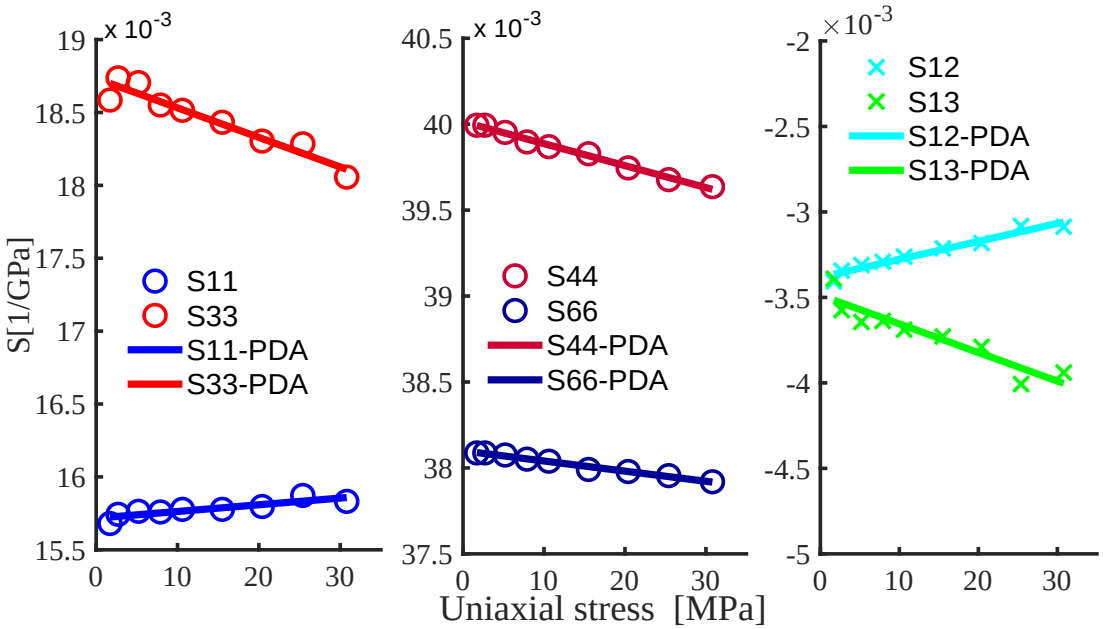

Figure 5.7: *Sample DR-VTI: components of compliance tensor versus the uniaxial stress. Experimentally determined and theoretically modeled data sets in comparison. The points indicate measured values, while the lines denote modelling results.*

The compliance tensor, modeled using the PDA, was calculated into the seismic velocities. Obtained velocities match well with the experimentally measured ones, shapes of the curves are similar. The maximal discrepancy between the modeled and measured velocity is equal to 0.1%, see Figure 5.8.

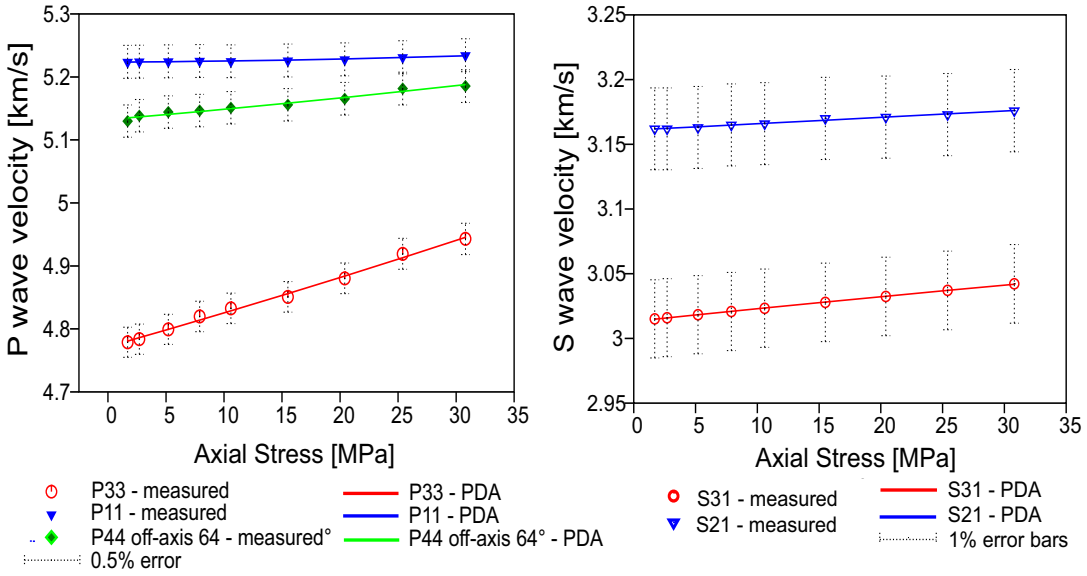

Figure 5.8: *Sample DR-VTI: measured and modeled velocities as a function of the uniaxial stress. Measured velocities are indicated by the points, while theoretical values are denoted by the solid lines. P -wave velocities on the left and S -wave velocities on the right.*

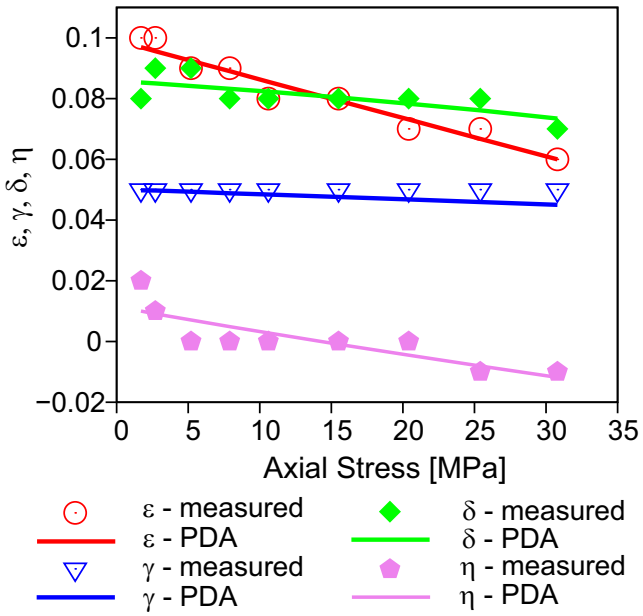

Figure 5.9: *Sample DR-VTI: measured and modeled anisotropy parameters as a function of the uniaxial stress. The points indicate measured values, while the lines represent modeled data.*

5.4 Orthorhombic sample DR

The application of the PDA resulted in a modeled compliance tensor with nine independent constants (equations set 2.53). As expected, stress-dependent compliance curves can be separated into two groups: first, with significant changes and a non-linear form, and second, with moderate changes and a nearly linear form. First group is significantly influenced by deformation of the compliant porosity and represents S_{11}, S_{55} and S_{66}, while the second group is mainly influenced by deformation of the stiff porosity and includes S_{22}, S_{33}, S_{44} and the non-diagonal S_{13}, S_{23}, S_{12} (Figure 5.10). This observation confirms theoretically proposed separation of the porosity into stiff and compliant parts and their distinct influence on the stress dependent elastic parameters.

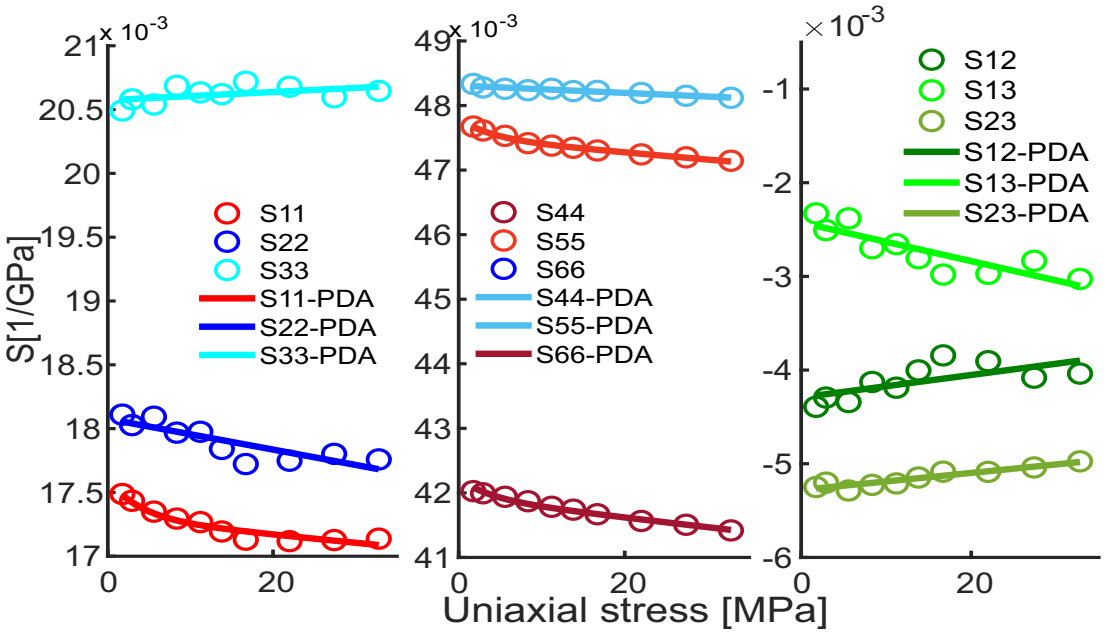

Figure 5.10: *Sample DR-ORT: components of compliance tensor versus the uniaxial stress. Measured and numerically modelled data sets in comparison. The points show experimental data, while the lines display theoretical modelling.*

Using equation 2.54 the compliant porosity ϕ_{11}^{c0} was estimated to be 0.12%, see Table B.3. After modelling of the compliance tensor were calculated the modeled velocities. Theoretically obtained velocities are in agreement with the experimentally determined ones, see Figure 5.11. The trends and shapes of the curves coincide. The largest discrepancy between the modeled and the measured velocity is equal to 0.1%.

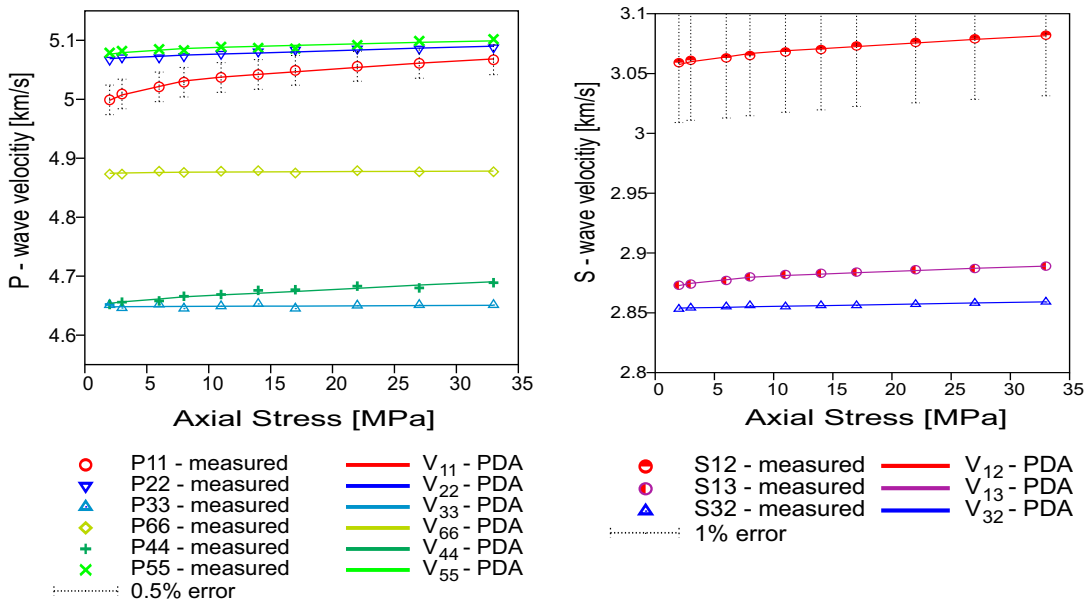

Figure 5.11: *Sample DR-ORT: measured and modeled velocities as a function of the uniaxial stress. Measured velocities are indicated by the points, while theoretical calculations are denoted by the solid lines. P -wave velocities on the left and S -wave velocities on the right.*

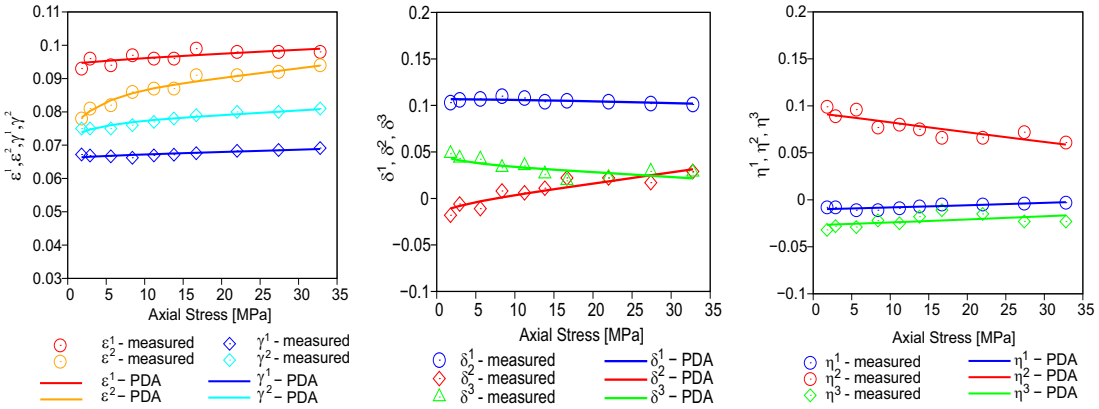

Figure 5.12: *Sample DR-ORT: measured and modeled anisotropy parameters against the uniaxial stress. Points indicate the measured values and lines represent the modeled data.*

Discussion: VTI and orthorhombic samples DR

The stress-velocity curves of the VTI sample demonstrate a linear form due to two possible reasons: a non-significant content of compliant porosity or an "insufficient" stress regime. "Insufficient" stress regime means, that the non-linearity of the curves will only appear at larger stresses. For the considered experiment, it is not possible to distinguish whether it is the first or the second case.

Another interesting observation made on the orthorhombic sample is that the stress distribution (stress-dependent velocity increase) seems to be related to the layering. For example, an axially propagated S-wave velocity: polarized parallel to the bedding V_{12}, is slightly more stress sensitive then polarized perpendicularly to the bedding V_{13}. The difference equals to 0.2%. The next example, the velocity of the radially propagated P-wave: parallel to the bedding V_{22} increases by 0.4%, while perpendicular to the bedding V_{33} does not change. The described phenomenon is notable, but not significant. A possible explanation could be related to the composite materials and the isostrain model (e.g., Nettles, 1994; Kalidindi and Franco, 1997; Kreja, 2011).

Conclusions: VTI and orthorhombic samples DR

Two samples cored from the same, visually layered marlstone block were studied. Velocity measurements revealed a VTI seismic anisotropy of one of the samples and orthorhombic seismic anisotropy of the another sample. As a possible origin of the orthorhombic symmetry was proposed the imperfect disorder (i.e., a weak spatial order) of the mineral grains. An uniaxial stress was applied in order to measure stress-dependent elasticity. Experimental data confirmed the theoretically proposed stress dependencies: the non-diagonal and particular diagonal components of the compliance tensor demonstrate linear stress dependencies, while some diagonal components show nonlinear stress dependencies. The PDA approach associate the first group to deformation of the stiff porosity and the second group to deformation of the compliant porosity. It provides an accurate fit and a theoretical description for both groups of observations.

Measurement results of the orthorhombic medium reveal a rather nonlinear stress-dependency of the ultrasonic velocities. For analysis and comparison, are used the coefficients obtained by the PDA. The coefficients K^{α}_{ijkl} describing the linear stress-dependency are related to the deformation of the stiff porosity. They have the same order for both VTI and orthorhombic samples, see Table B.3. The coefficients describing the nonlinear stress-dependency, B_{ik} and F_c, are related to the deformation of the compliant porosity and show a substantial difference for the VTI and for the orthorhombic samples. In the case of the VTI sample, the coefficient B_{33} is negligibly small (effectively equal to zero). A possible interpretation of this is the following. Firstly, the initial compliant porosity ϕ^{c0}_{33} of the VTI sample is negligible. At the same time, the coefficient F_c is assumed to be non-zero and similar for both samples (this corresponds to the isotropic piezosensitivity tensor). Multiplication of the non-zero exponential stress function and the zero coefficient B_{33} produces a zero term. This is in agreement with the linear shape of the stress-dependent compliance. In the case of the orthorhombic sample, the coefficients B_{11} and F_c demonstrate notable values, reflecting the nonlinear shape of the stress-dependency and describing the deformation of compliant porosity as significant. These differences between the B_{11} and the B_{33} coefficients indicate the content of the compliant porosity.

Another argument supporting the negligible B_{33} of the VTI medium is related to the sensitivity analysis. Sensitivity analysis uses a Jacobian matrix to estimate the confidence interval of the coefficient determination. According to this analysis, the coefficient F_c cannot be determined precisely, see Mayr et al. (2016). The linear shape of the observed stress-dependency does not provide information about the exponential function. Therefore, the numerical fitting estimates the coefficient F_c as not well restricted, but the coefficient B_{33} as very small. Physical interpretation indicate that the small B_{33} corresponds to a negligible compliant porosity. The not well restricted F_c does not contradict the assumption that F_c shows similar values for both studied samples.

5.5 Discussion

One of the important questions is related to the anisotropy of the linear and nonlinear elastic moduli. Measurements show that, apparently, the stress-sensitivity of the nonlinear moduli in rocks depends much more on the direction of observation than the stress sensitivity of the linear moduli (e.g., Rasolofosaon and Yin, 1996). On the one hand, to some extent, this is explained by the definition of the nonlinear tensor. Indeed, the absolute value of the third-order stiffnesses can be several orders of magnitude larger than the linear ones. Thus, their measurement errors can play here a significant role, and it is rather difficult to measure nonlinear stiffnesses precisely enough. However, contributions of the nonlinear tensors are multiplied by the Lagrangian strain. These products are not larger (and usually significantly smaller) than the contributions of the linear tensor. Therefore, using an isotropic approximation for the nonlinearity remains a sufficient and pragmatic option (see e.g., Prioul et al., 2004; Shapiro, 2017).
On the other hand, the linear tensor in the PDA approach is anisotropic. Moreover, Shapiro and Kaselow (2005) use an anisotropic piezosensitivity tensor (resulting also in anisotropic nonlinear tensor), under the restrictions of stress application perpendicular to the symmetry planes and the elastic symmetry being orthorhombic or higher. Whereas, Shapiro (2017) considered the linear anisotropy of the medium increased up to a triclinic (arbitrary anisotropy and no restrictions regarding the direction of the stress application). In this case, the isotropic piezosensitivity tensor seems to be sufficient for the description of the experimental results. In fact, despite the piezosensitivity tensor being isotropic, corresponding terms are multiplied by the generalized porosity tensor (see equation 79 in Shapiro (2017)). The generalized porosity tensor is usually anisotropic and impacts the nonlinear moduli. The resulting nonlinear moduli become anisotropic. This is especially the case for fractured media.

5.6 Conclusions: PDA

The application of the PDA on a set of laboratory measured data was studied. Modelling helps to describe the behavior of the stress-dependent elastic constants and to analyze the distinct influence of different porosity types. The compliant porosity demonstrates the largest impact on the stress dependency, however, for some samples the influence of the stiff porosity is also significant. A comparison of different shales demonstrates different regimes of the stress dependency, but all of them were successfully modeled using the PDA. The obtained modelling coefficients are useful for quantitative analysis of physical parameters and mechanisms. Moreover, the once obtained modelling coefficients could be used for prediction of the stress-dependency under arbitrary stress conditions.

Part III

Triaxial loading

Chapter 6

Experimental methodology: triaxial loading

This part is dedicated to the dependence of shale's elastic parameters on triaxial multi-stage loading. The loading path includes: a loading cycle, an unloading cycle and a reloading cycle. Each cycle consists of the hydrostatic (un)loading and differential axial (un)loading stages. The corresponding laboratory measurements and interpretation of obtained results were performed. The proposed multi-stage loading path is especially attractive for the application of the porosity deformation approach (PDA). The PDA could be "learned" during the modelling of the first hydrostatic loading stage and predicts elastic constants for the following uniaxial loading stage.
Here, are described laboratory experiments containing multi-stage triaxial loading of the saturated samples and simultaneous measurements of ultrasonic velocities and deformations. The studied samples are introduced as well as the used laboratory equipment and the experimental procedure. Then are presented the results of performed study and are described the observed dependencies.

6.0.1 Press and transducers

The loading of the samples was performed in the multi-stage triaxial regime. Here, are introduced the press, the ultrasonic sensors and the strain gauges. The measurement cell was developed by the third party "Gesteinslabor Jahns". The press is capable to perform triaxial loading (hydrostatical loading plus differential axial loading) with drained measurement conditions (fluid is free to move out of the sample), see Figure 6.1. Transducers provide up to 27 different seismic velocity measurements, see Figure 6.2. Configuration of the sensors is designed for the determination of the complete stiffness tensor for orthorhombic or TI media, see Figure 6.3. Loading was measured using a digital measurement cell mounted into the press. All equipment is controlled and programmed digitally.

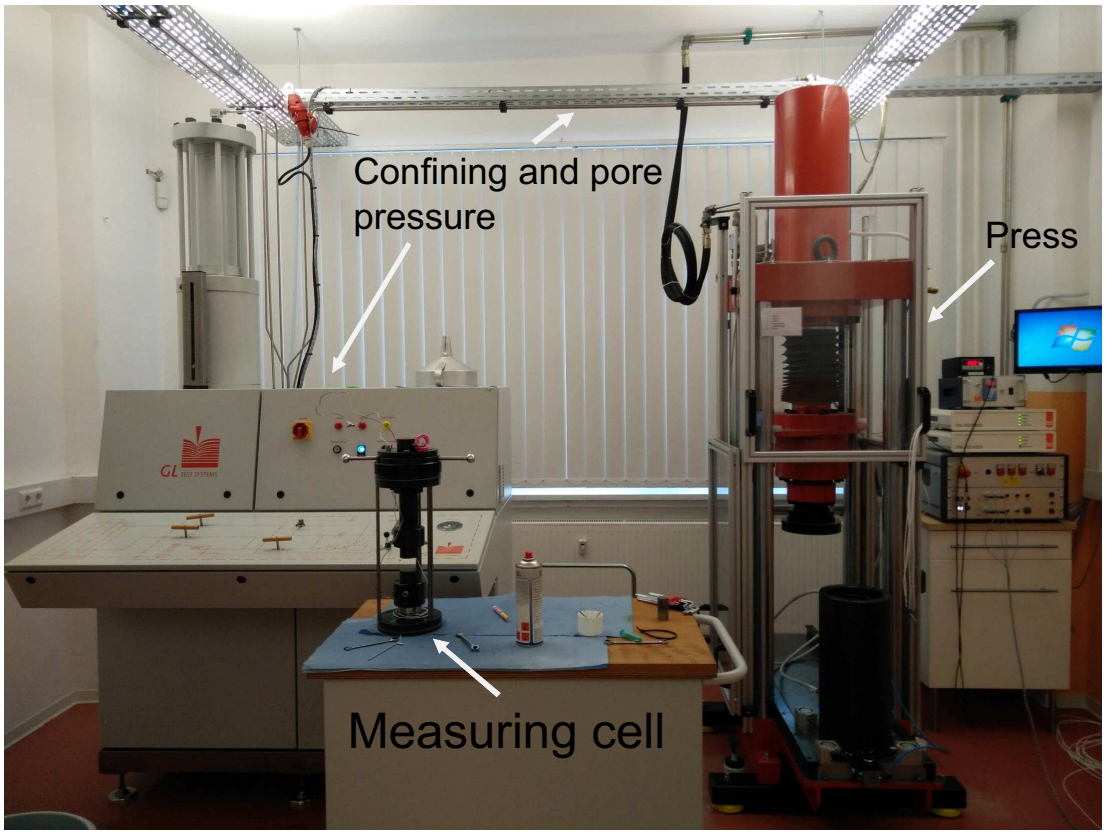

Figure 6.1: *Experimental equipment in "Gesteinslabor Jahns" laboratory.*

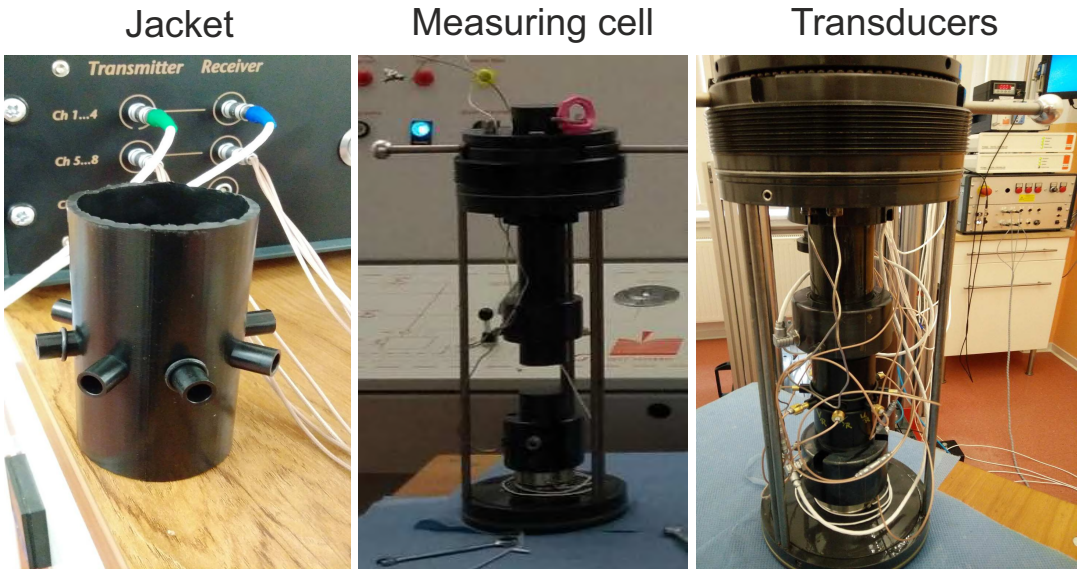

Figure 6.2: *Measuring Cell: left – resin jacket; middle – measuring cell; right – installed transducers.*

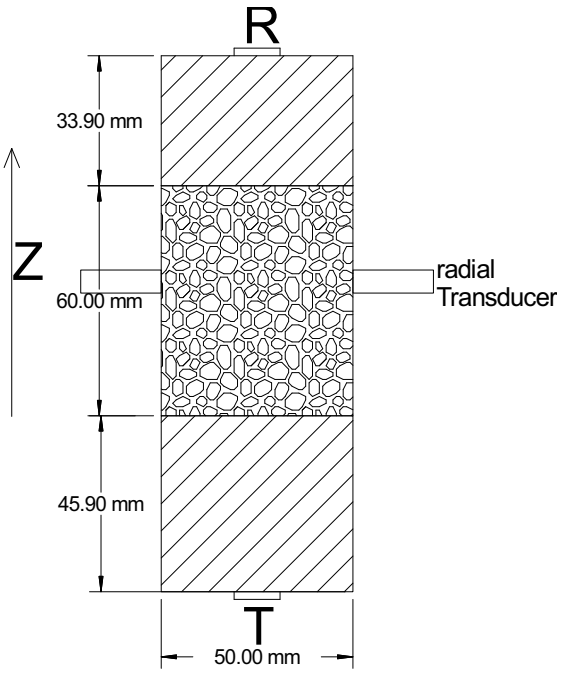

Figure 6.3: *Experimental setup for seismic velocity measurements. T – transducer, R – receiver. The sketch was prepared by H. Baumgartner.*

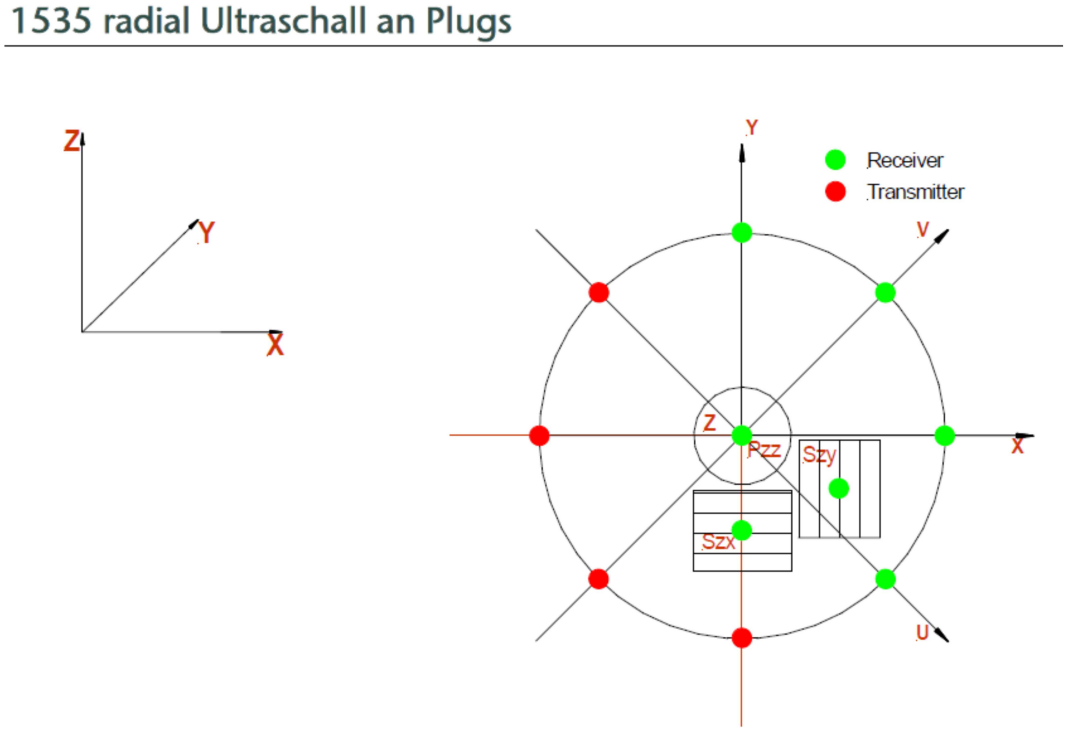

Figure 6.4: *Orientation of the transducers and notation of the experimental set-up used by "Gesteinslabor Jahns". In this thesis is used a different notation, which depends on the sample symmetry.*

6.0.2 Strain measurements

Axial deformations were measured digitally, using LVDT (Linear Variable Differential Transformer). Radial deformations were not measured directly due to the construction difficulties.

6.1 Measurements methodology

The single-plug methodology was applied and all required seismic velocities were measured on the same sample (Wang, 2002a). Five independent stiffnesses of the VTI samples were measured during a single experiment. Nine independent stiffnesses of the orthorhombic medium (initially HTI samples) were measured during two separate experiments. Two separate experiments were a minimal possible number to complete the measurements, because of the limited space at the sample's surface for installation of the transducers.

6.1.1 Loading path

The samples were loaded in a quasi-static regime. The maximal load was chosen corresponding to the samples's consolidation. The number of the loading stages defines the sampling rate of the ultrasonic measurements and was designed to provide necessary density of the data points. Triaxial loading was applied stepwise in two distinct regimes: hydrostatical loading and differential axial loading. The complete experiment was divided into six phases: phase 1 – hydrostatical loading 0-80 MPa; phase 2 – differential axial loading 0-40 MPa; phase 3 – differential axial unloading 40-0 MPa; phase 4 – hydrostatical unloading 80-5 MPa; phase 5 – hydrostatical loading 5-80 MPa; phase 6 – differential axial loading 0-40 MPa, see Figure 6.5. Values correspond to the experiment on the HR1-VTI sample. The values of differential axial loading can vary for different samples, depending on the sample's consolidation.

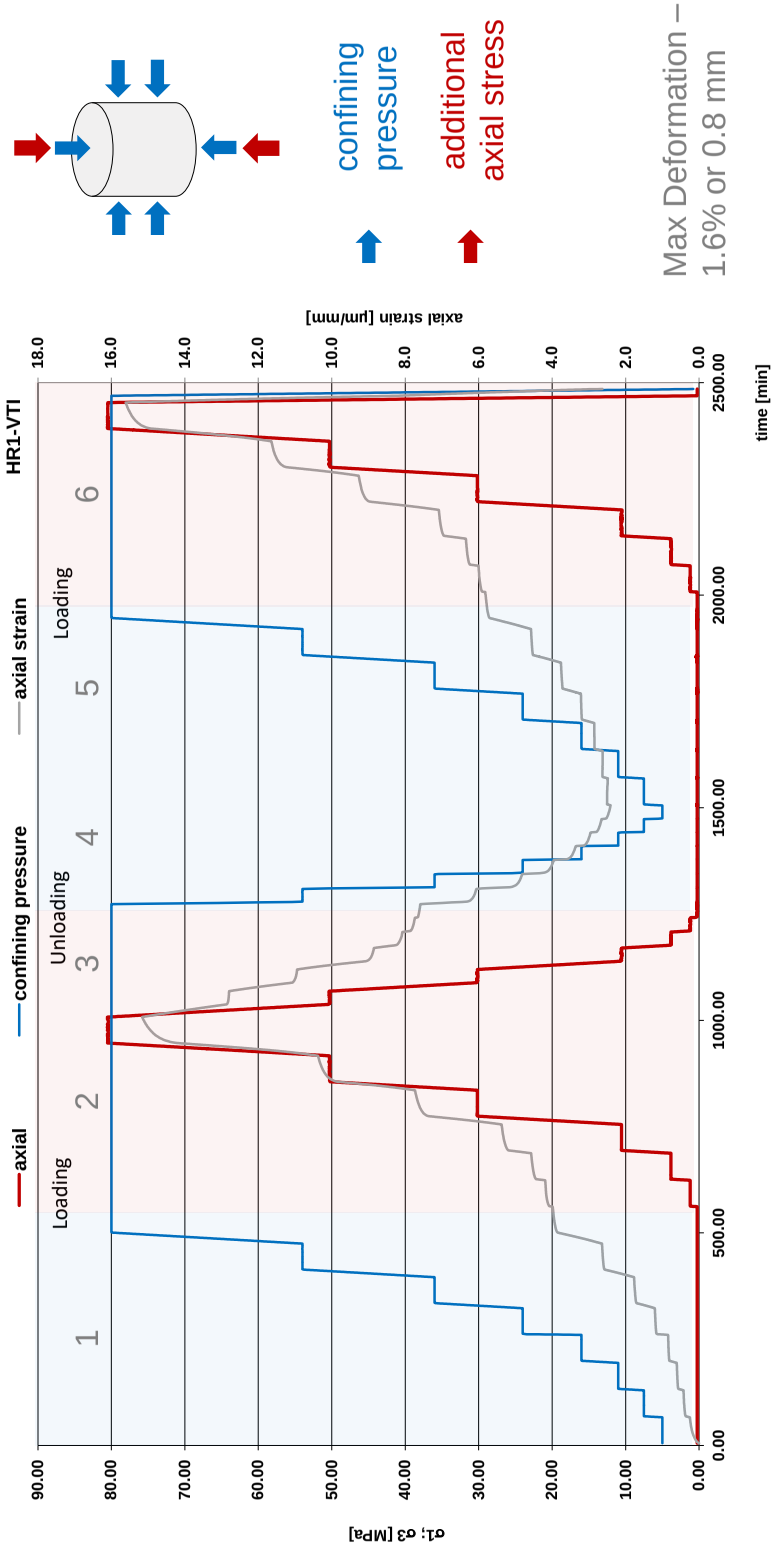

Figure 6.5: *Exemplary loading path: phase 1 – hydrostatical loading; phase 2 – differential axial loading; phase 3 – differential axial unloading; phase 4 – hydrostatical unloading; phase 5 – hydrostatical loading; phase 6 – differential axial loading. Stress values can vary depending on the sample.*

6.1.2 Stress-dependent travel path

The size of the sample is changing during the loading and depends on the current stress regime. Therefore, the true travel path of the elastic waves depends on the sample deformations and on the loading. The true velocities were recalculated using the true travel path. In case of the sample shortening, the apparent velocity demonstrates overestimated values. In case of the sample expanding, the apparent velocity shows underestimated values. All deformations in the axial direction were measured by use of LVDT (linear variable differential transformer). Deformations in the radial direction were estimated using the measured ultrasonic velocities.

During loading was observed the following. In the axial direction occurred the sample shortening during the both, hydrostatical and differential axial loading. While, in the radial direction is observed shrinking during the hydrostatical loading and expanding during the differential axial loading.

During unloading were measured the different trends: in the axial direction sample expands during the both, hydrostatical and differential axial unloading. In the radial direction sample is expanding during hydrostatical unloading and is shrinking during the differential axial unloading.

Obtained deformations were used for calculation of the true velocities. This effect has a significant influence and can not be neglected.
Recalculation of the velocities was done according to the equation 6.1:

$$V_{true} = \frac{S_{true}}{t_{meas} - t_0}, \tag{6.1}$$

where V_{true} – true velocity;
S_{true} – true travel path;
t_{meas} – measured travel time;
t_0 – travel time of the electrical impulse through the cables and equipment.
The actual travel path S_{true} in axial direction was determined using the LVDT according to equation 6.2:

$$S_{true} = S_0 - S_{def}, \tag{6.2}$$

where S_0 – the sample size before experiment;
S_{def} – measured axial sample deformation, shortening is determined as the positive deformation and expanding as the negative deformation.
Radial deformations were estimated using elastic parameters determined from measured ultrasonic velocities. This methodology does not provide very accurate estimation, but is the best possible solution. Shortening under hydrostatical loading was calculated according to equation 6.3:

$$S_{true} = S_0 - (\frac{S_{def}}{E_1/E_3} \cdot \frac{1}{E_{dyn}}), \tag{6.3}$$

where E_1 and E_3 – dynamically determined Young's modulus for TI medium,
E_{dyn} – correction coefficient defined as average relation of Young's modulus E_3 calculated using velocity measurements to Young's modulus E_3 calculated using deformation measurements.
Expansion in the radial direction under differential axial loading was calculated using following equation 6.4:

$$S_{true} = S_{def} \cdot \nu_{31}, \tag{6.4}$$

where ν_{31} – Poisson's ratio of TI medium calculated using measured velocities, see Mavko et al. (2009), p. 34.

As an illustration of the velocities recalculation, compare Figure 6.6 showing measured ultrasonic velocities without any recalculation and Figure 6.7 showing ultrasonic velocities after recalculation corresponding to the true travel path.

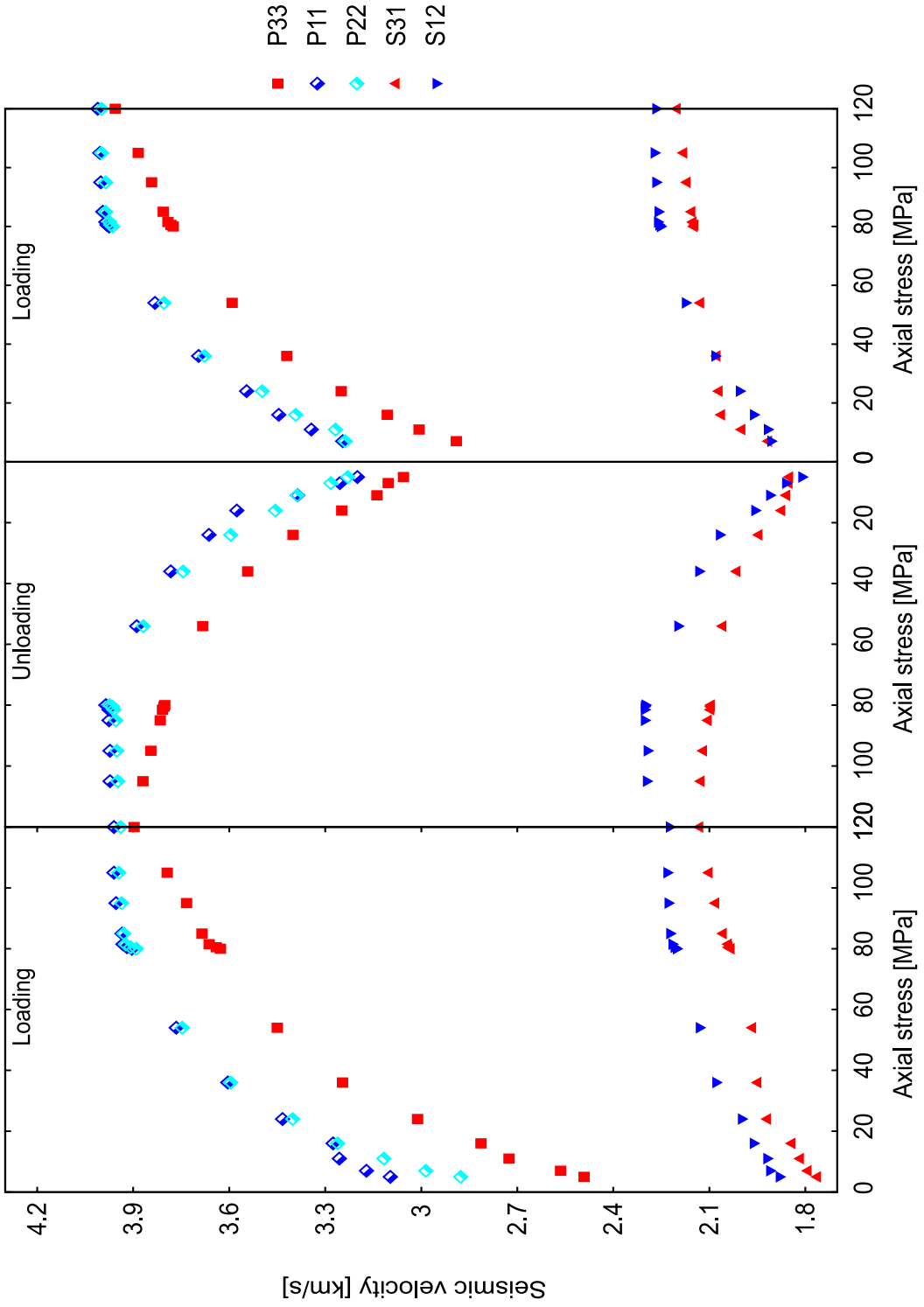

Figure 6.6: *SPS-VTI sample, combined graphic of seismic velocities without taking into account the deformations. Velocities have following indication: red squares – P-axial; light blue and dark blue diamonds – P-radial in two mutually orthogonal directions; red triangles – S-axial; blue triangles – S-radial with polarization parallel to the bedding.*

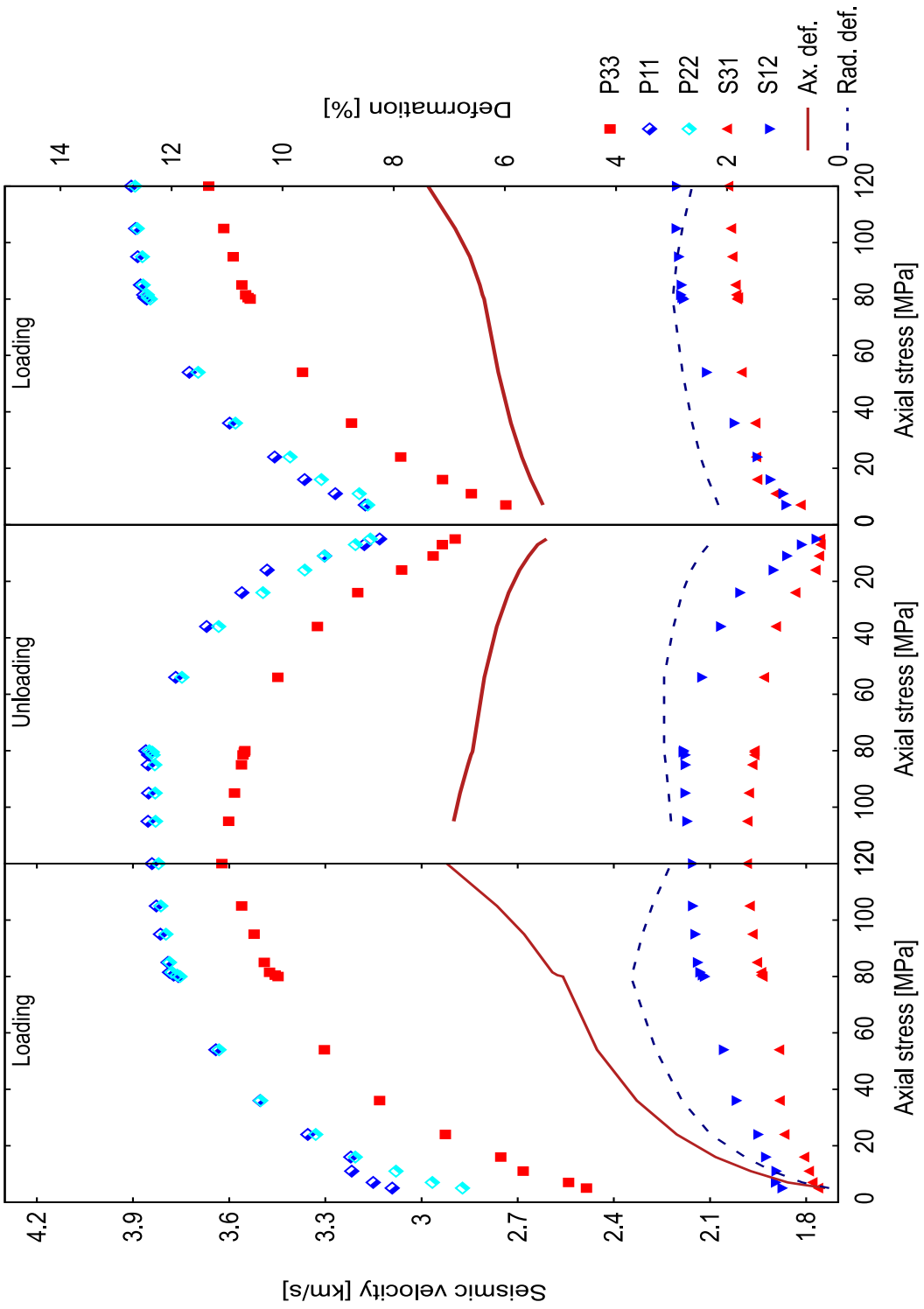

Figure 6.7: *SPS-VTI sample, combined graphic of seismic velocities over 6 loading phases. Velocities have following indication: red squares – P-axial; light blue and dark blue diamonds – P-radial in two mutually orthogonal directions; red triangles – S-axial; blue triangles – S-radial with polarization parallel to the bedding. Red solid line denotes measured axial deformations. Blue dashed line displays estimated radial deformations.*

6.1.3 Errors estimation

The error (accuracy + precision) for velocity measurements was estimated to be: in the axial and in the off-axis directions – 0.5%; in the radial direction – 0.3%. The filtering and other post-processing procedures reduce the error by 0.1-0.2%. The difference between two analogues experiments caused by positioning and coupling uncertainties was estimated to be around 1%. In total, we estimate the summarized accuracy (due to the errors in estimation of the sample's lengths and calibration of the electronic) equal to 0.3% and the summarized precision (due to the errors in picking, positioning and coupling uncertainties) equal to 1%.

6.2 Rock sample characterization

This chapter contains the characterization of the investigated samples and short descriptions of used methodologies. Density was determined either by use of Archimedes' principle or using the geometrical methodology. The Scanning Electron Microscope (SEM) and thin section analysis were used for the sample's analysis. Investigated samples have different grades of consolidation and were classified as shales and marlstones.

Figure 6.8: *Seal peel sample SPS, income state. The core was preserved by three layers: resin, steel, gyps. Photo is provided by the "Gesteinslabor Jahns" laboratory.*

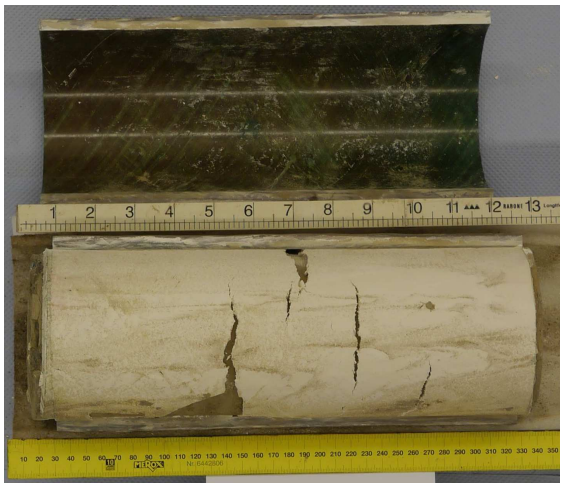

Figure 6.9: *Seal peel sample SPS, opening process. The core was preserved by three layers: resin, steel and gyps, displayed as the white cover on the sample. Photo is provided by the "Gesteinslabor Jahns" laboratory.*

6.2.1 Description of the sample SPS

Seal peel sample was extracted from a depth of 2087 meters. The sample was preserved immediately after the extraction, see Figure 6.8. The protective tubing was opened just before the ultrasonic experiments (Figure 6.9). The saturation of the sample was considered as close to in-situ conditions. The prepared sample has cracks visible by the naked eye, see Figure 6.10. The dominant mineral is quartz, with angular shape. This shape indicates that the quartz minerals were transported by wind. The dominant grain size is around 100 μm. The intrinsic anisotropy is present, the disc shaped minerals demonstrate preferred orientation. The density of the sample was measured in "Gesteinslabor Jahns" using geometrical methodology (weight/volume) and is equal to 2100 kg/m^3. Geometrically, the sample has cylindrical form with 60.3 mm height and 49.84 mm diameter.

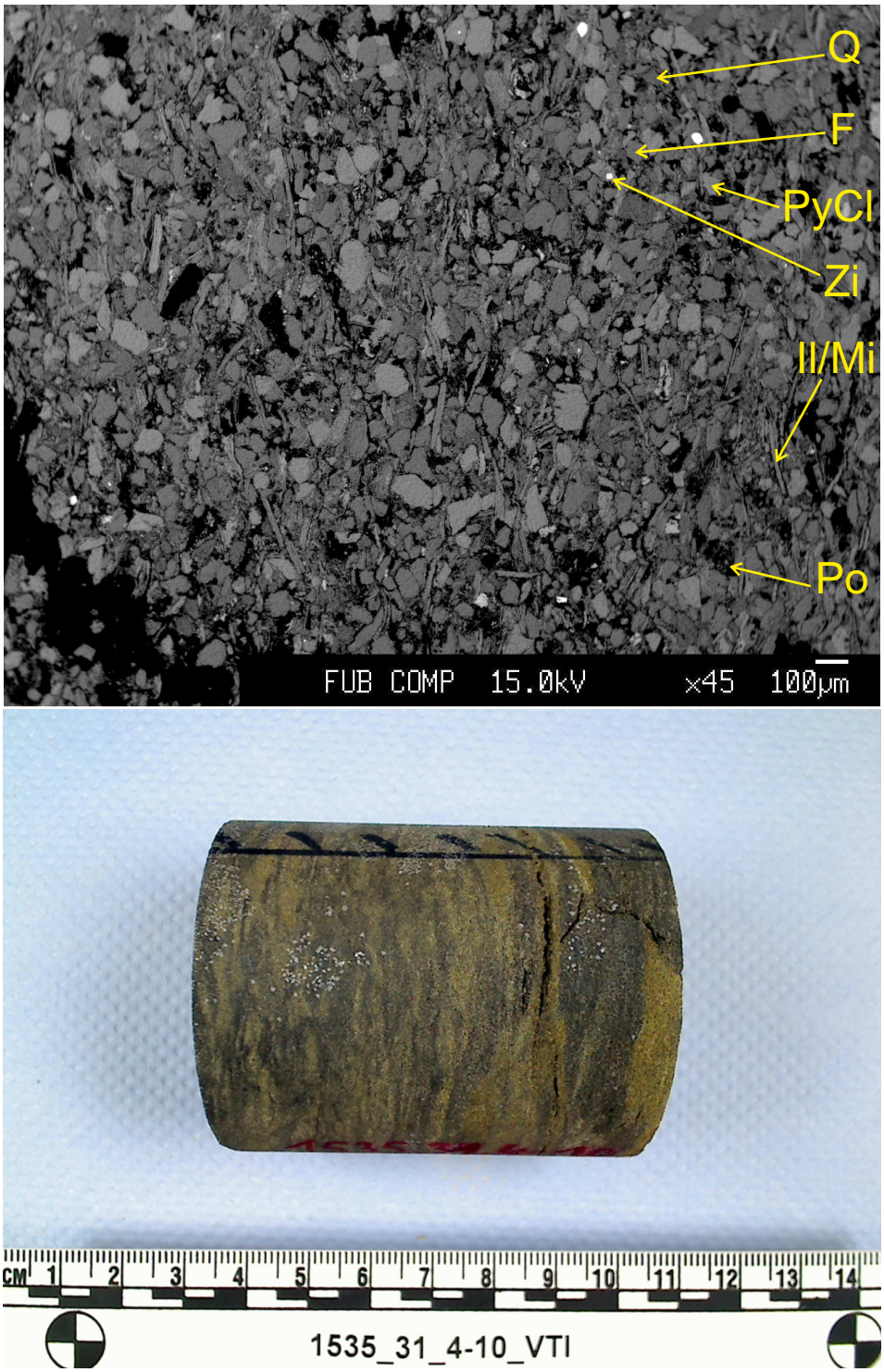

Figure 6.10: *Seal peel sample SPS. Top – Electron probe microanalysis, where: Q – quartz (dark grey); F – feldspar/orthoclase (grey); PyCl – pyrite+clay (light-grey); Zi – zircon (white); Il/Mi – illite/mica (plate/disc); Po – pore space (black). Bottom – sample photo, made just after samples extraction. Some cracks are visible by the naked eye, these cracks are oriented parallel to the layering.*

6.2.2 Description of the sample HR1

Sample HR1 was extracted from a depth of 1632 meters and stored under in-situ humidity conditions. Drilling core was preserved using foil and vacuum evacuation, see Figure 6.11. According to the visual inspection, the sample is well consolidated, see Figure 6.13. The sample was classified as dolomite rock. The dominant mineral is dolomite and the dominant grain size is between 10 and 20 μm. Microanalysis demostrates strong lamination of the minerals. Observed cracks are probably the product of the genesis, possibly related to the release of stress (personal communication, Ralf Milke, 2017). The measured in "Gesteinslabor Jahns" density is equal to 2330 kg/m^3. Geometrically, the sample has cylindrical form with 52.31 mm height and 49.85 mm diameter.

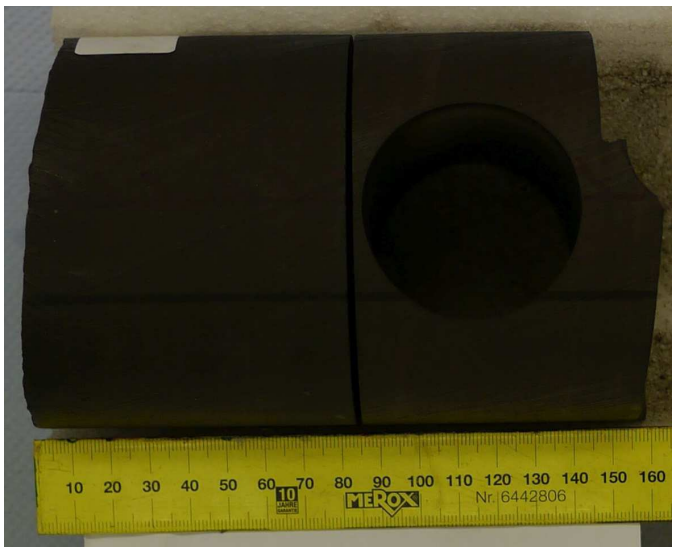

Figure 6.11: *Sample HR1, sample extraction. Photo is provided by the "Gesteinslabor Jahns" laboratory.*

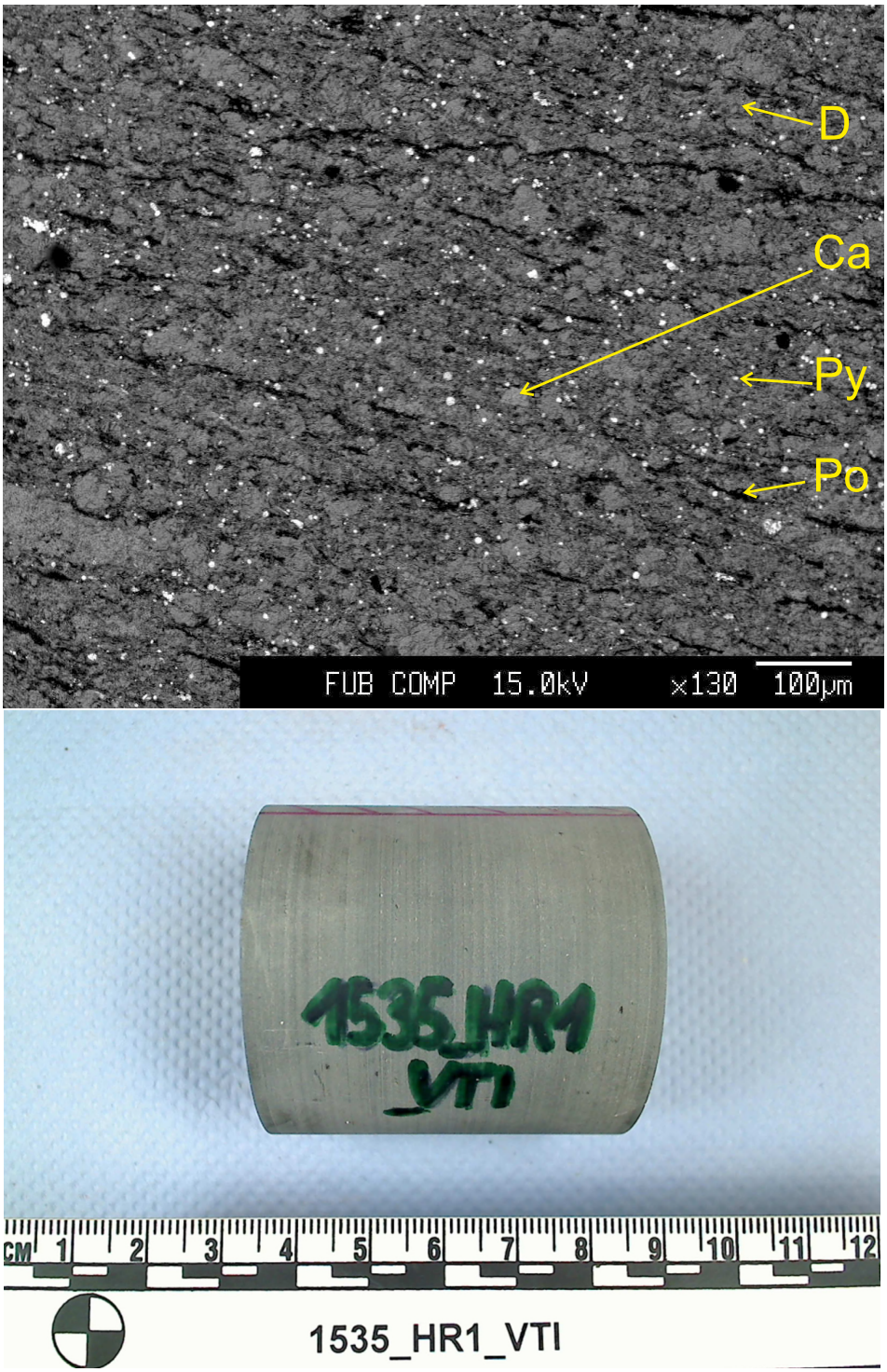

Figure 6.12: *Sample HR1. Top – Electron probe microanalysis, where: D – dolomite (dark grey); Ca – calcite (light grey); Py – pyrite (white); Po – pore space (black). Grains are 10-20 μm in diameter, strongly laminated. Bottom – photo of the sample, after visual inspection the sample was considered as well consolidated.*

6.2.3 Description of the sample FB1

Sample FB1 was extracted from a depth of 3214 meters (Brown Jurassic, Dogger) and stored under in-situ humidity conditions. According to the visual inspection, the sample is well consolidated, see Figure 6.13. The sample was classified as shale with clay minerals rich on aluminum (personal communication, Ralf Milke, 2017). Preferred orientation of the minerals or disc-shaped minerals were not observed. The measured in "Gesteinslabor Jahns" density is equal to 2520 kg/m^3. Geometrically, the sample has cylindrical form with 60.34 mm height and 49.82 mm diameter.

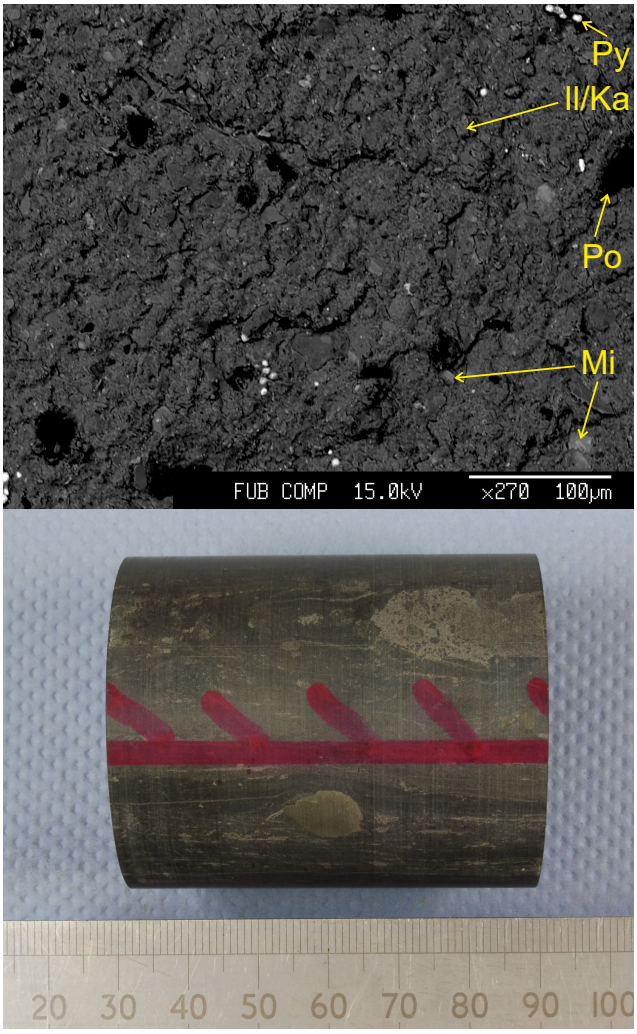

Figure 6.13: *Sample FB1. Top – Electron probe microanalysis, where: Il/Ka – illite/kaolinite (platelets/grey); Mi – mica (light grey); Py – pyrite (white); Po – pore space (black). Grains are 20-30 μm in diameter. Bottom – photo of the sample, after visual inspection the sample was considered as well consolidated.*

Chapter 7

Measurement results: triaxial loading

7.1 Deformations

Information about the sample's deformation under the stress is important for following reasons: calculation of the true travel path of the seismic wave; mechanical hysteresis; (non)linearity of the stress-deformation relation. Deformations were measured directly in the axial direction only.

7.1.1 VTI and HTI samples SPS

Measured axial strain was used to calculate the true velocities. The maximal axial deformation equals 7.4%. The sample does not recover the initial shape and size after the first loading cycle, see Figure 7.1, Figure 7.2. The deformation is mostly irreversible. As a possible explanation are considered the drained measurement conditions of the experiment. Fluid is free to leave the sample during the loading but can not be sucked back during the unloading. The second reason is the irreversible close of cracks and compliant porosity.

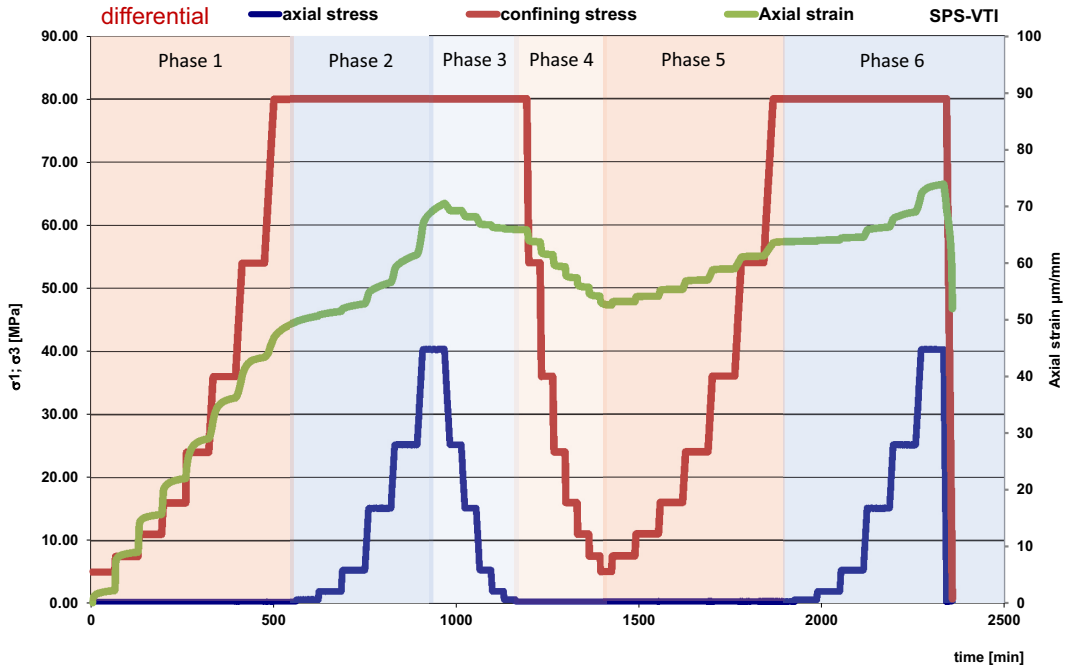

Figure 7.1: *Seal peel sample SPS-VTI. Axial strain is indicated by the green line. The strain remains significant after unloading in phase 3 and phase 4 (significant hysteresis of strain). This is an indication of irreversible deformation.*

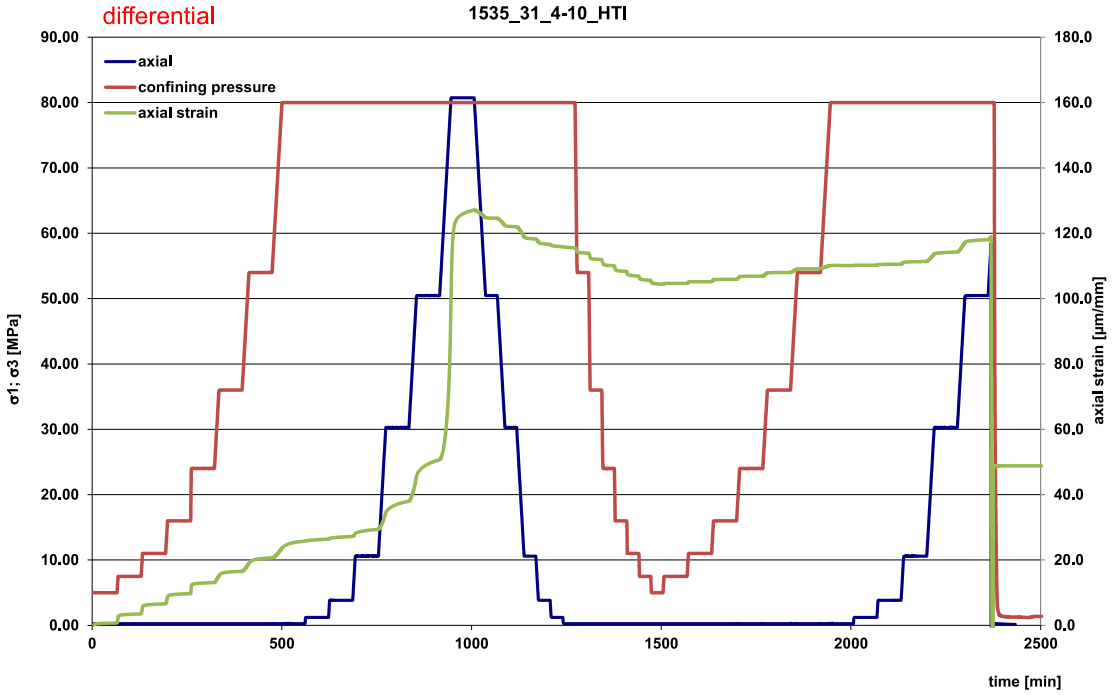

Figure 7.2: *Seal peel sample SPS-HTI. For the notation see Figure 7.1. Significant hysteresis of strain as in the sample SPS-VTI.*

7.1.2 VTI and HTI samples HR1

The measured axial strain is moderate and was used to calculate the true velocities. The maximal axial deformation equals 1.6%. The deformations have rather reversible character, see Figure 7.3, Figure 7.4. Visually, the sample shows good consolidation, which was confirmed by the observations. The sample demonstrates a notable creep effect.

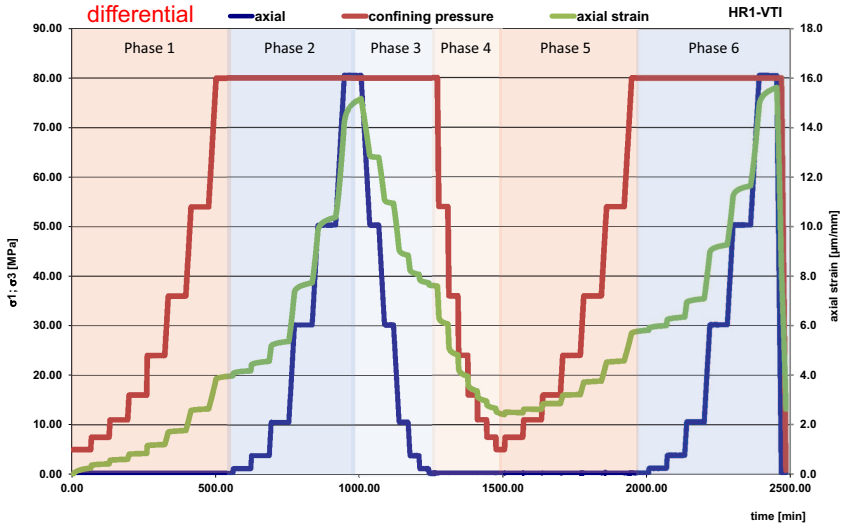

Figure 7.3: *HR1-VTI sample. For the notation see Figure 7.1 Observed hysteresis of strain is moderate.*

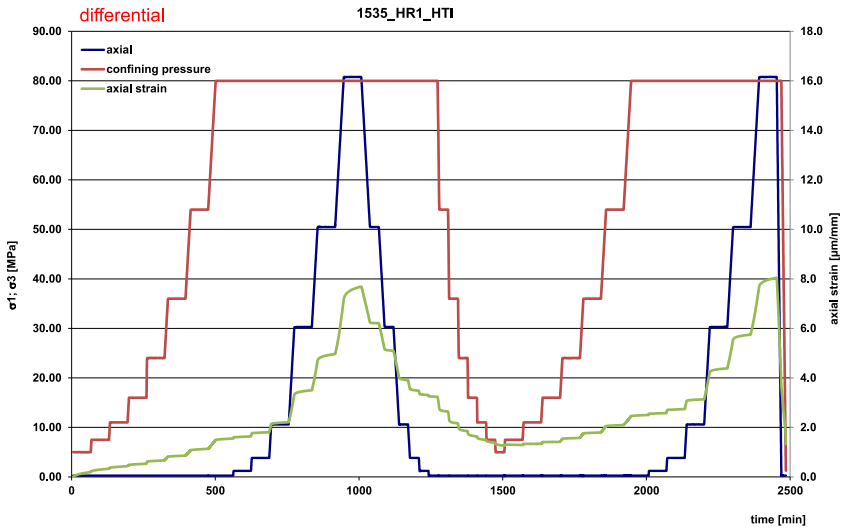

Figure 7.4: *HR1-HTI sample. For the notation see Figure 7.1. The strain is almost recovered after unloading, which is an indication of the reversible deformation.*

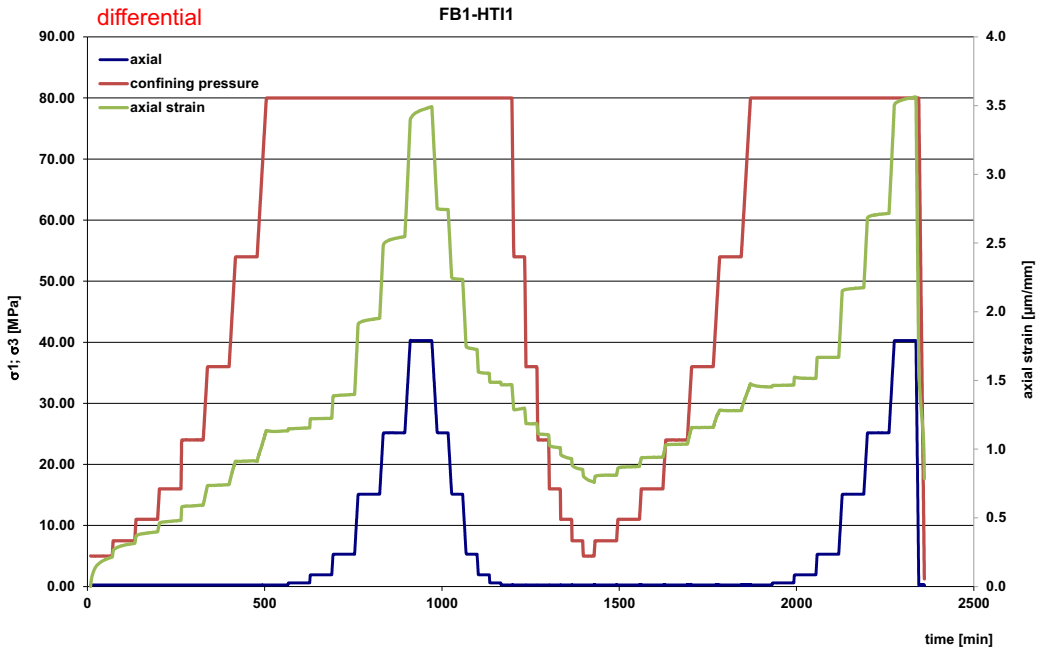

Figure 7.5: *FB1-HTI sample. For the notation see Figure 7.1 Observed hysteresis of strain is moderate.*

7.1.3 HTI sample FB1

Maximal deformation was 0.5 $\mu m/mm$ for hydrostatic loading and additionally 2.5 $\mu m/mm$ for triaxial loading, see Figure 7.5. The strain in the axial direction shows non-significant magnitude with maximum of 0.35%. The hysteresis was observed for the first loading and unloading cycles. The deformations are mostly reversible and were used for the calculation of the true velocities. The creep effect is observed.

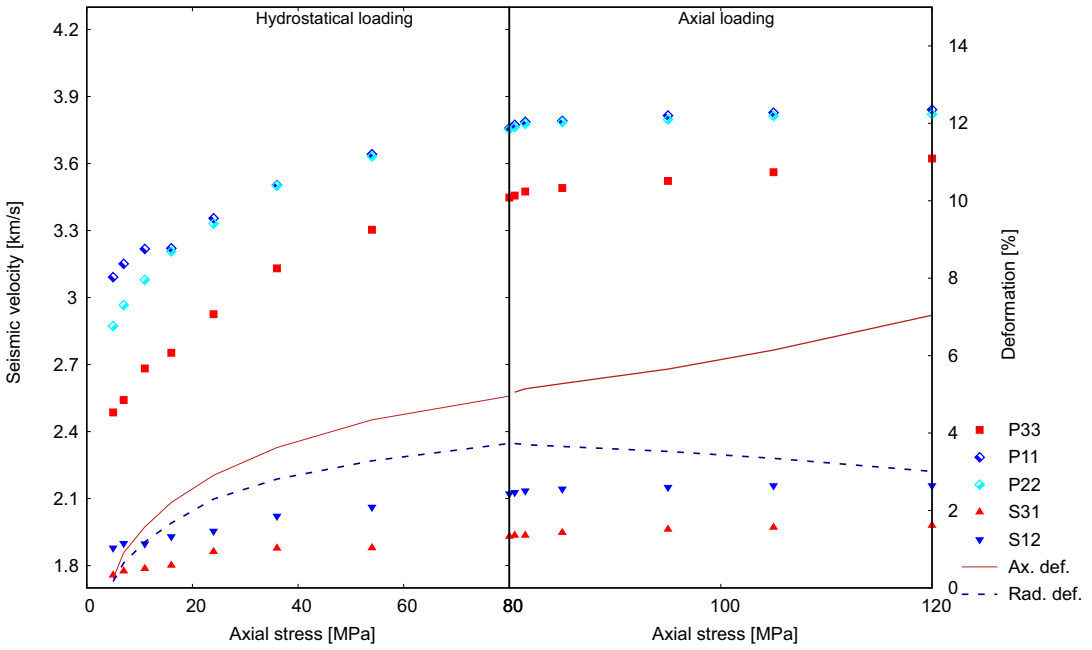

Figure 7.6: *SPS-VTI sample, seismic velocities during the first loading cycle: hydrostatic loading on the left and differential axial loading on the right. Velocities have following indication: red squares – P-axial; light blue and dark blue diamonds – P-radial in two mutually orthogonal directions; red triangles – S-axial; blue triangles – S-radial with polarization parallel to the bedding.*

7.2 Ultrasonic velocities

The loading paths of the triaxial experiments contains three cycles: two loading- and one unloading-cycle. Each cycle, consists of two stages: hydrostatic- and differential axial- loading. For the sake of simplicity, the whole loading path is decomposed and the first loading cycle is considered separately. The hydrostatic- and differential axial- loading stages are compared. The description of the whole loading path is based on observations from the first cycle.

SPS samples

Generally, the SPS samples were classified as weakly consolidated samples with visible cracks. This explains very weak and disturbed signals at the low stress levels and the growing signal quality during increasing of the stress. The quality of the signal was enhanced by use of stacking and noise compensation methodology.

7.2.1 VTI sample SPS

SPS-VTI, first loading cycle

The first loading cycle consist of hydrostatic and differential axial loading stages. Hydrostatic loading impacts all measured ultrasonic velocities, see Figure 7.6 on the left. Despite an equal loading along all the directions, velocity increase depends on the direction of the wave propagation. The elastic waves propagated in the axial direction, P_{33} and S_{31}, are more stress sensitive than elastic waves propagating in the radial direction P_{11}, P_{22} and S_{12}. Also, the shape of the velocities curves in the axial direction shows higher nonlinearity in comparison to the radial direction. These observations correspond to the layered

composition of the sample, where the axial direction is perpendicular to the layering and radial direction is parallel to the layering.

The second loading stage with differential axial loading is applied to the pre-stressed sample. This explains the observed relatively moderate velocities increase.
Elastic waves propagated in the loading direction rise significantly and display a nonlinear shape. Elastic waves propagated in the radial direction show notable nonlinear increase as well.

Interpretation and discussion

The hydrostatic loading is applied to the unstressed sample and therefore, has the major impact on the compliant porosity. As the consequence velocities show a significant nonlinear increase as function of stress. The velocity of the elastic waves propagated in the axial direction increase more than the velocity of the radially propagated waves. This can be explained by the layered structure of the sample: the majority of compliant porosity and of the micro/macro pores is oriented parallel to the layering and perpendicular to the axial direction of the sample. The deformation of compliant porosity and of the micro/macro cracks describes the directivity (dependence on the direction) of the stress-induced velocities increase.

As expected, the differential axial stress leads to a moderate velocity increase in the axial (loading) direction. A rather unexpected observation was, that velocities increase also in the radial direction. This can be probably explained by the saturation of the sample, by the hydrostatically pre-stressed (during the first loading stage) state of the sample, and by the drained measurement conditions. The mobile fluids could partly transfer axial stress into the radial direction. The similarity of measured P-wave velocities in the radial direction, P_{11} and P_{22}, confirms the expected VTI symmetry of the sample.

SPS-VTI, complete loading path

Here, the trends observed for the first loading cycle are expanded for the following unloading and reloading cycles. The effects related to the loading/unloading processes are described, see Appendix C.
The shape of stress-velocity curves is not completely symmetrical for the loading and unloading (first and second) cycles. see Figure C.1. This displays the hysteresis of ultrasonic velocities. Maximal velocities during the reloading (third) cycle are similar to the maximal velocities during the first loading cycle.
Anisotropy parameter ε systematically decreases during the loading and increases during the unloading. This behaviour remains similar for both loading regimes: hydrostatic and uniaxial. The decrease of ε during the hydrostatic loading is more significant than during the uniaxial loading, which can be explained by the fact that before the hydrostatic loading the sample is unstressed.
Anisotropy parameter γ shows different trends for different stress regimes. In the case of hydrostatic loading, γ increases, in the case of hydrostatic unloading γ decreases. In contrast to the hydrostatic loading, during the uniaxial loading γ decreases and during the uniaxial unloading γ increases.

Interpretation and discussion

Hysteresis of seismic velocities is significant and indicates an irreversible deformation of pore space/cracks. This can be particularly explained by the drained experiment conditions: fluids were free to escape the sample during the loading and could not be sucked back into the sample during the unloading.

Interpretation of the stress-dependent parameter ε is straightforward: in the case of any loading, the compaction in the axial direction is more significant and sample becomes more isotropic, which means a decrease of the anisotropy parameter ε. In the case of unloading. the compliant porosity and cracks are reopening and the sample becomes more anisotropic, ε rises.

Interpretation of the stress dependent parameter γ is more complicated. In the case of uniaxial loading/unloading, the dependency trends coincide with trends, described above for parameter ε and have a

similar explanation. In the case of hydrostatic loading/unloading dependency trends are opposite to the trends observed for parameter ε: an increase during the loading and a decrease during the unloading. This indicates that for a saturated, weakly consolidated, shale sample under hydrostatic loading, the velocity increase of the radially propagated S-wave with polarization parallel to the layering ("fast" S-wave) is more significant than the velocity increase of the axially propagated S-wave with polarization parallel to the layering ("slow" S-wave). A possible explanation for the observed effect would be the fact that S-wave does not propagate into the fluids, and the compaction parallel the layering could have a greater influence in comparison to the compaction perpendicular to the layering (also perpendicular to the water-filled cracks between the layers).

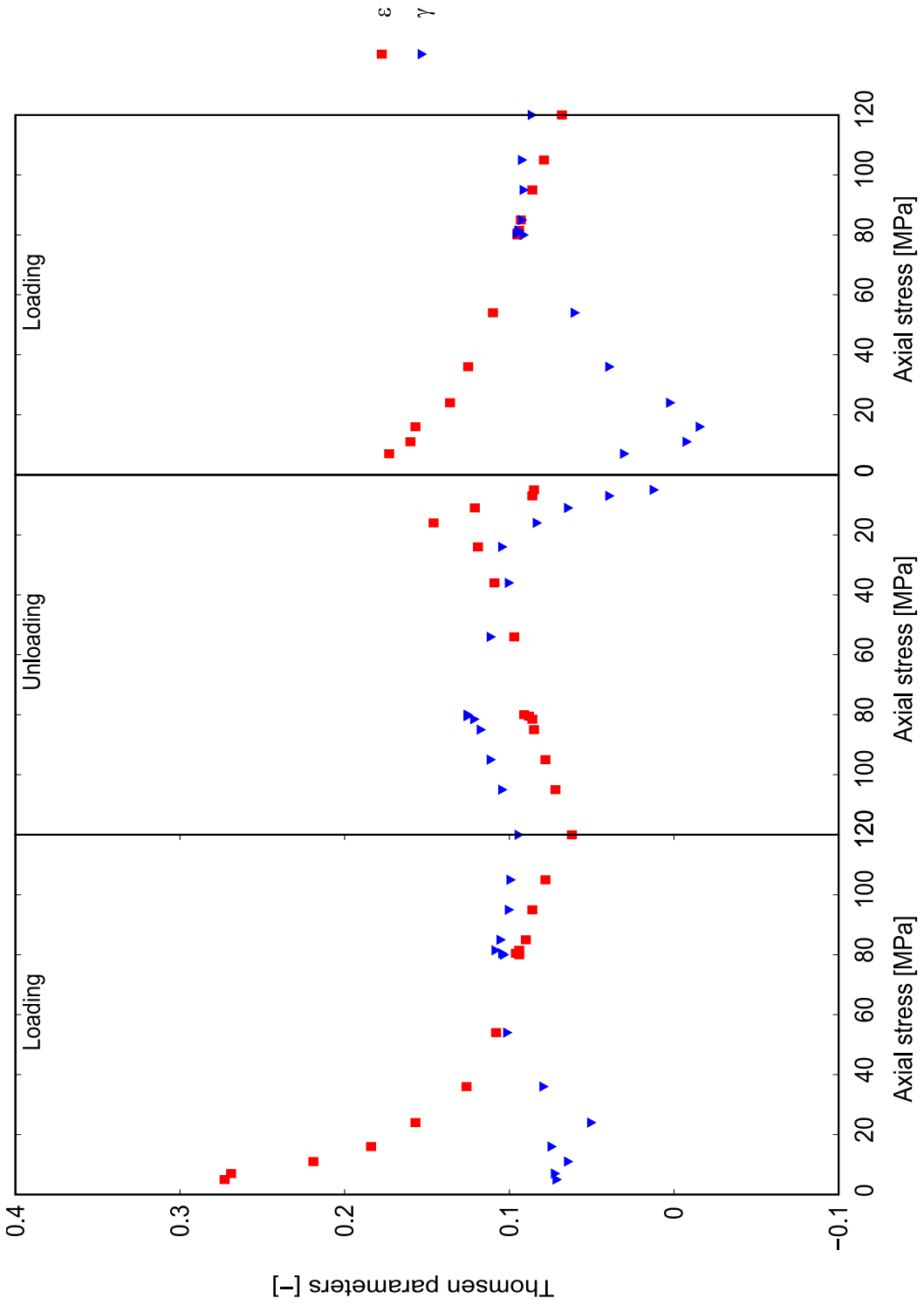

Figure 7.7: *SPS-VTI sample, Thomsen Parameters as a function of the stress.*

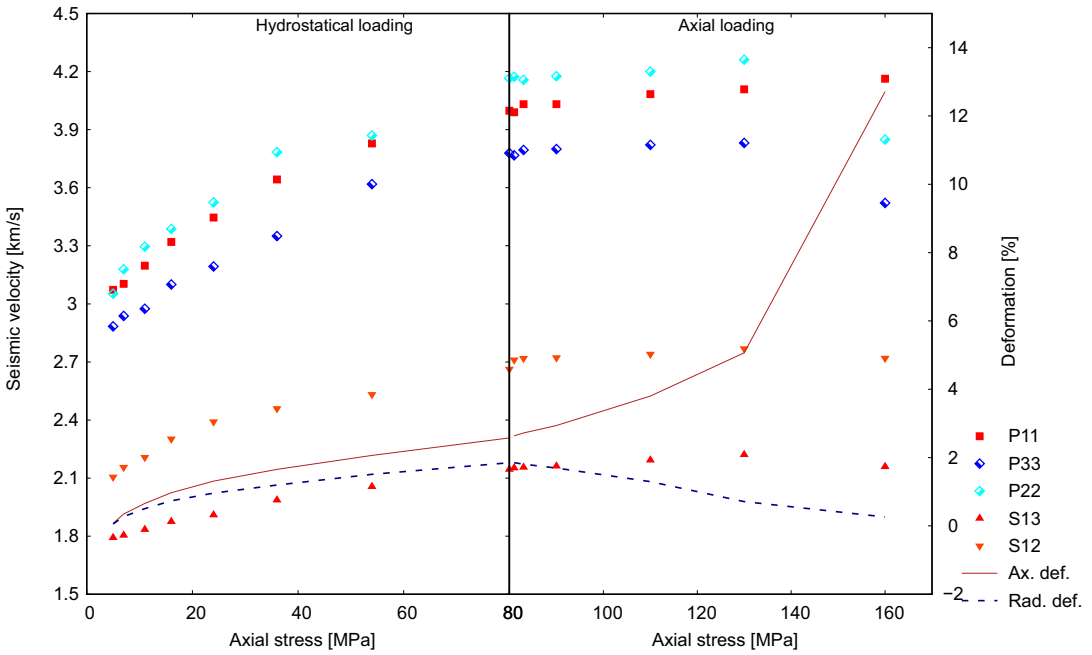

Figure 7.8: *SPS-HTI-1 sample, seismic velocities during the first loading cycle: hydrostatic loading on the left and differential axial loading on the right. Velocities have following indication: red squares – P-axial; light blue and dark blue diamonds – P-radial in two mutually orthogonal directions; red triangles – S-axial; blue triangles – S-radial with polarization parallel to the bedding. Red solid line denotes measured axial deformations. Blue dashed line displays estimated radial deformations.*

7.2.2 HTI sample SPS

Here, is determined the stiffness matrix of the orthorhombic medium. Due to the number of required measurements and due to the experimental setup were performed two similar experiments for each sample. These two experiments provide all necessary ultrasonic velocities. The two experiments are denoted as SPS-HTI-1 and SPS-HTI-2 (abbreviation HTI refers to initial HTI symmetry of the sample). Each experiment contains two loading cycles and one unloading cycle. For the sake of simplicity the first loading cycle is described separately and then the description is expanded for the whole loading path.

SPS-HTI-1, first loading cycle

The hydrostatic loading impacts all measured ultrasonic velocities. The induced velocity increase is significant and the shape of dependencies has a nonlinear form. The velocities of the P-waves propagated parallel to the layering in the axial and in the radial directions, P_{11} and P_{22}, demonstrate similar values, as expected. P-wave propagated in the radial direction perpendicular to the layering, P_{33}, displays similar shape but lower velocities. S-wave propagated in the axial direction with polarization parallel to the layering ("fast" S-wave) shows significant velocity increase and greater values than the velocity the S-wave propagated in the axial direction with polarization perpendicular to the layering ("slow" S-wave).

The differential axial loading influences all measured velocities, elastic waves propagated or polarized in the axial direction show more significant velocity increase in comparison to the elastic waves propagated in the radial direction. Nevertheless, elastic waves propagated in the radial direction show some increase as well. The last measurement carried out under 160 MPa demonstrates the velocities drop for all measured directions, except for P_{11}.

Interpretation and discussion

The radially propagated elastic wave P_{22} displays greater velocities than the axially propagated P_{11}, which is rather unexpected. A possible explanation for this effect are inelastic deformations (maybe cracks opening) of the saturated sample and difficulties of the deformation estimation in the radial direction. Exact estimation of the radial deformations is required for the determination of the true travel path and recalculation of the true velocities.

At the stress level of 160 MPa is observed a drop of all velocities except for axially propagated P-wave P_{11}. At the same time, measured axial deformations are around 12 %. A possible explanation is that the sample was damaged and split by a macro crack(s). Interestingly, the axial P-wave velocity P_{11} remains unaffected, what indicates that the crack(s) plane is non-intersecting with the travel path of P_{11}. A probable crack(s) plane is oriented parallel to the layering, but a little aside from the P_{11} travel path. The assumption of the sample destruction is supported by the measured axial deformation, which does not recover during unloading of the sample. After the experiment the sample was extracted from the measurements cell, and it was observed that the sample was crushed into many pieces.

SPS-HTI-1, complete loading path

A comparison of the first loading cycle to following unloading and reloading cycles reveal a significant hysteresis of observed velocities and deformations. The best demonstration is a comparison of the beginning of the first loading cycle with the beginning of the reloading cycle, see Appendix C, Figure C.2. Axial deformation is almost irreversible. These effects can be explained by drained loading conditions and by particular destruction of the sample, which became evident after extracting of the sample from the measurement cell.

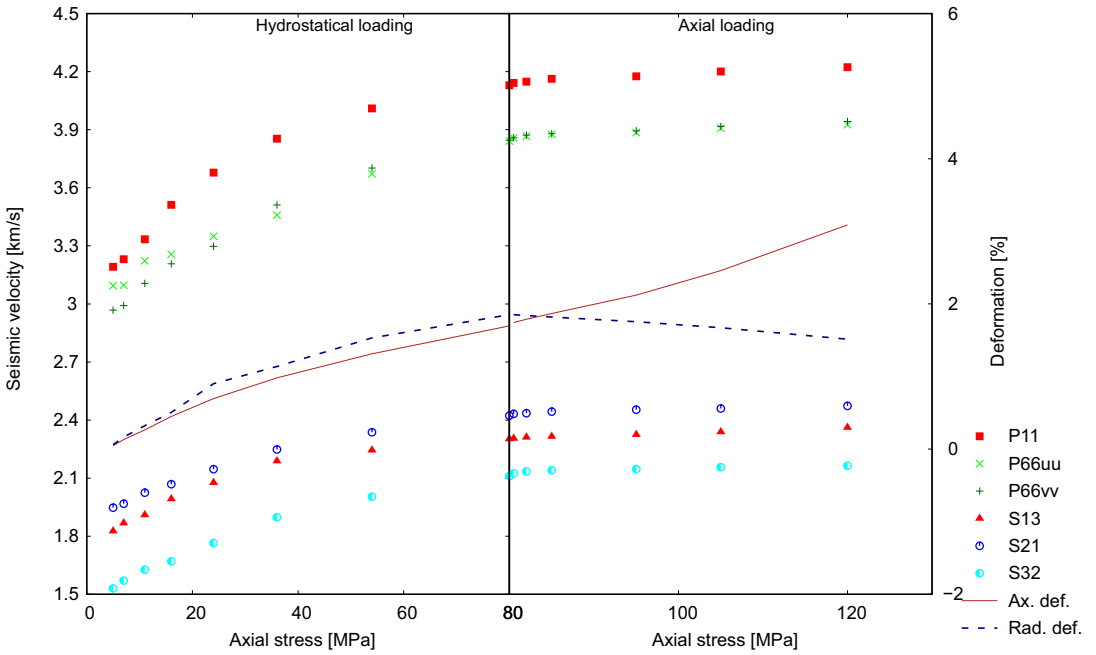

Figure 7.9: *SPS-HTI-2 sample, seismic velocities during the first loading cycle: hydrostatic loading on the left and differential axial loading on the right. Velocities notation: red squares – P-axial; light green and dark green crosses – P-radial under* 45° *to both vertical symmetry planes (exactly in between of them); red triangles – S-axial with polarization perpendicular to the bedding; blue open circles – S-radial with polarization parallel to the bedding. Red solid line denotes measured axial deformations. Blue dashed line displays estimated radial deformations.*

SPS-HTI-2

This experiment was supposed to be carried out using the same sample as for the previous experiment, but the sample SPS-HTI-1 was broken during the axial loading above 140 MPa. In order to complete the measurement set, an identical sample from the same core and on the same day was extracted. The maximal axial loading was reduced to 120 MPa, to prevent destruction of the sample.

SPS-HTI-2, first loading cycle

Hydrostatic loading influences all measured velocities, the shape of velocities change shows a nonlinear form, see Figure 7.9. Two mutually perpendicular P-waves propagated in the radial direction under 45° to the layering (of the initially HTI sample) P_{66uu} and P_{66vv} demonstrate similar curves and lie below the axially propagated P_{11}, which confirms presumed orthorhombic seismic symmetry of the sample.

During the axial loading, velocities of the elastic waves propagated in the loading direction demonstrate more significant increase than the velocities of the elastic waves propagated in the radial direction. S-wave propagated in the axial direction with polarization perpendicular to the bedding S_{13} is comparable to the measured on SPS-HTI-1: significant increase during the hydrostatic loading, moderate increase during differential axial loading, repeatability of measured values.

SPS-HTI-2, complete loading path

A substantial hysteresis was observed: velocity values after unloading are higher than before the loading, see Appendix C, Figure C.3. Unlike to the SPS-HTI1 sample, radially propagated elastic waves do not

indicate any failure. Axial deformations demonstrate a restricted reversibility.

Interpretation and discussion

Due to the failure of the sample during the first experiment the stress regime was changed: differential axial stress was reduced from 80 MPa to 40 MPa. The reduced stress regime preserved the sample from destruction.

For the calculation of anisotropy parameters were used data obtained during the first experiment, except for γ_2 where it was necessary to use the data obtained during the SPS-HTI-2 experiment. The maximal axial loading differs for these two experiments, therefore γ_2 was calculated up to the axial stress of 120 MPa (maximal for the SPS-HTI-2 experiment).

For this particular sample, the anisotropy parameters are describe for the first loading cycle only, because of presumed failure of the sample at the stress level of 160 MPa. Anisotropy parameter ε_1 (refers to the two radial P-waves) does not show any clear trend, ε_2 (refers to the axially propagated P-wave and propagated in the radial direction perpendicular to the layering P-wave) displays some fluctuations but not any definitive pattern, see Figure 7.10. Anisotropy parameter γ_1 (refers to the two axially propagated S-waves with polarization parallel and perpendicular to the layering) demonstrates some increase during the first loading cycle, which indicated more significant velocity increase of the S-wave polarized parallel to the layering. Parameter γ_2 displays some decrease during the loading.

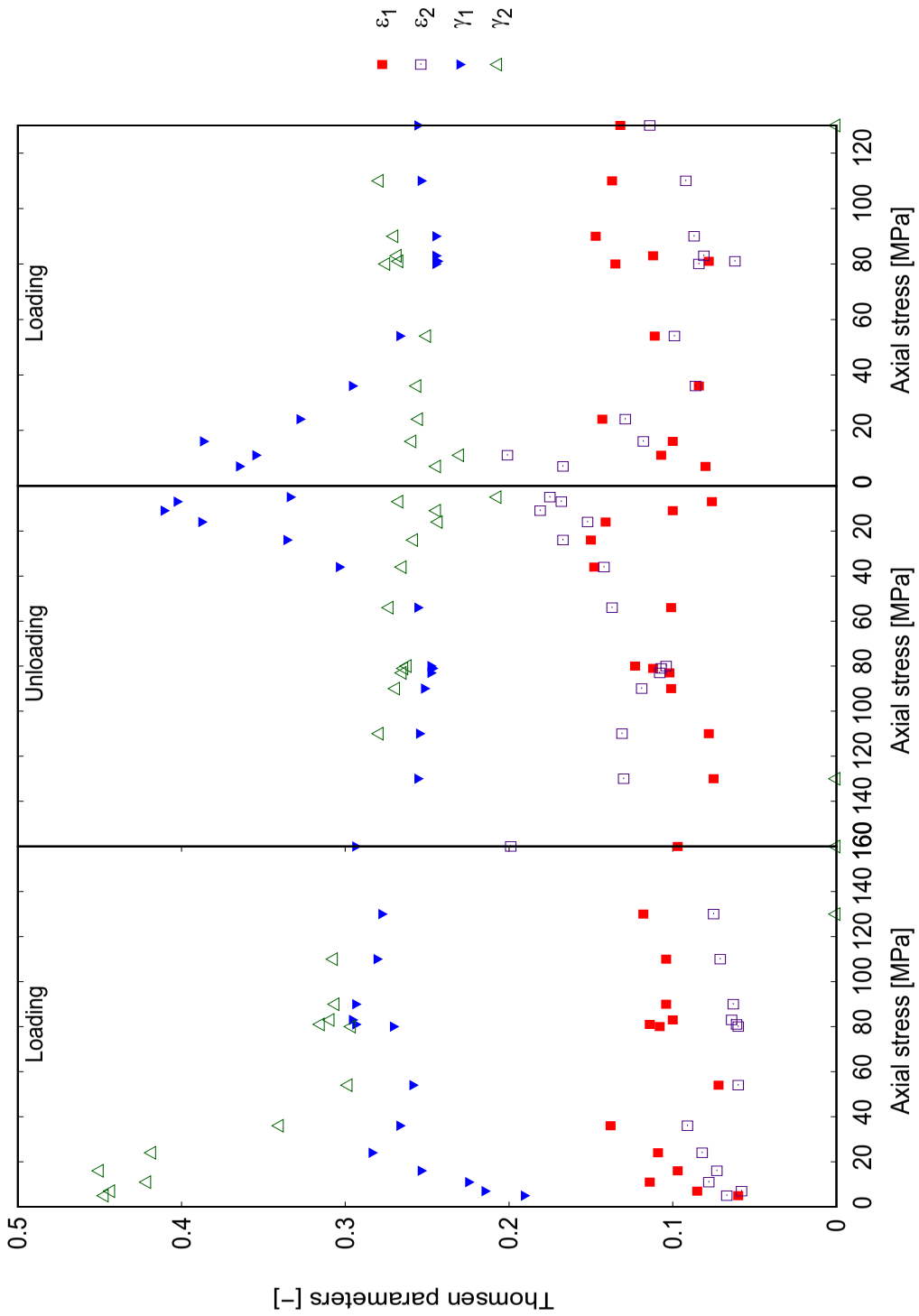

Figure 7.10: *SPS-HTI sample, anisotropy parameters as a function of the stress.*

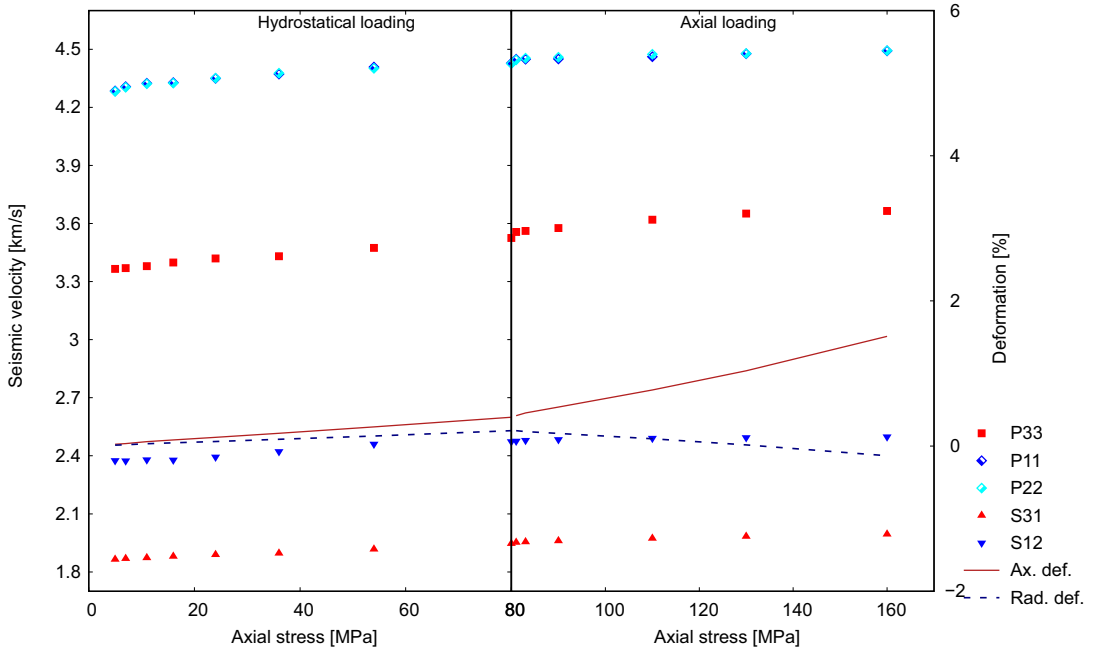

Figure 7.11: *HR1-VTI sample, seismic velocities during the first loading cycle: hydrostatic loading on the left and differential axial loading on the right. Velocities notation: red dots – P axial, light blue and dark blue dots – P radial in two mutually orthogonal directions, red triangles – S axial, blue triangles – S radial with polarization parallel to the bedding. Red solid line denotes measured axial deformations. Blue dashed line displays estimated radial deformations.*

HR1 samples

Generally, the samples were classified as well consolidated and partially saturated rock. Samples were stored under in-situ humidity conditions. Sample deformations lie below 2%. Hysteresis was considered as non-significant. Signal forms are pronounced and the signal quality is sufficient for reliable picking.

7.2.3 VTI sample HR1

HR1-VTI, first loading cycle

The hydrostatic loading affects all measured velocities, the stress dependency curves show a nonlinear form, see Figure C.4. The velocity increase is significant, P_{33} propagated in the axial direction increases by 4.8 %, while radially propagated P_{11} and P_{22} rise by 3.5%.
During the differential axial loading the velocities of the elastic waves propagated in the axial direction increase more significant than the velocities measured in the radial direction. For example P_{33} increases by 4.1% (relative to the beginning of the axial loading) and radially propagated P_{11} and P_{22} rise by 1.5%. The S-waves confirm the trends observed for the P-waves. The initial anisotropy is significant.

HR1-VTI, complete loading path

Here, the observations described for the first loading cycle are expanded for the complete loading path, see Appendix C. The axial deformations do not reveal any significant hysteresis, the ultrasonic velocities do not indicate any notable hysteresis, see Figure C.4. In a first approximation the sample deformations can be classified as reversible.

Interpretation and discussion

The two mutually perpendicular P-wave propagated in the radial direction, P_{11} and P_{22}, demonstrate almost identical velocities, which confirms supposed VTI symmetry of the sample.
The sample demonstrates significant initial anisotropy, more than 0.3 for ε and γ, see Figure 7.12. Both anisotropy parameters decrease during the loading and increase during the unloading. The influence of the differential axial loading/unloading on the anisotropy parameters is more significant than the influence of hydrostatic loading. Interestingly, initial ε and γ are almost equal, but response differently to the loading.

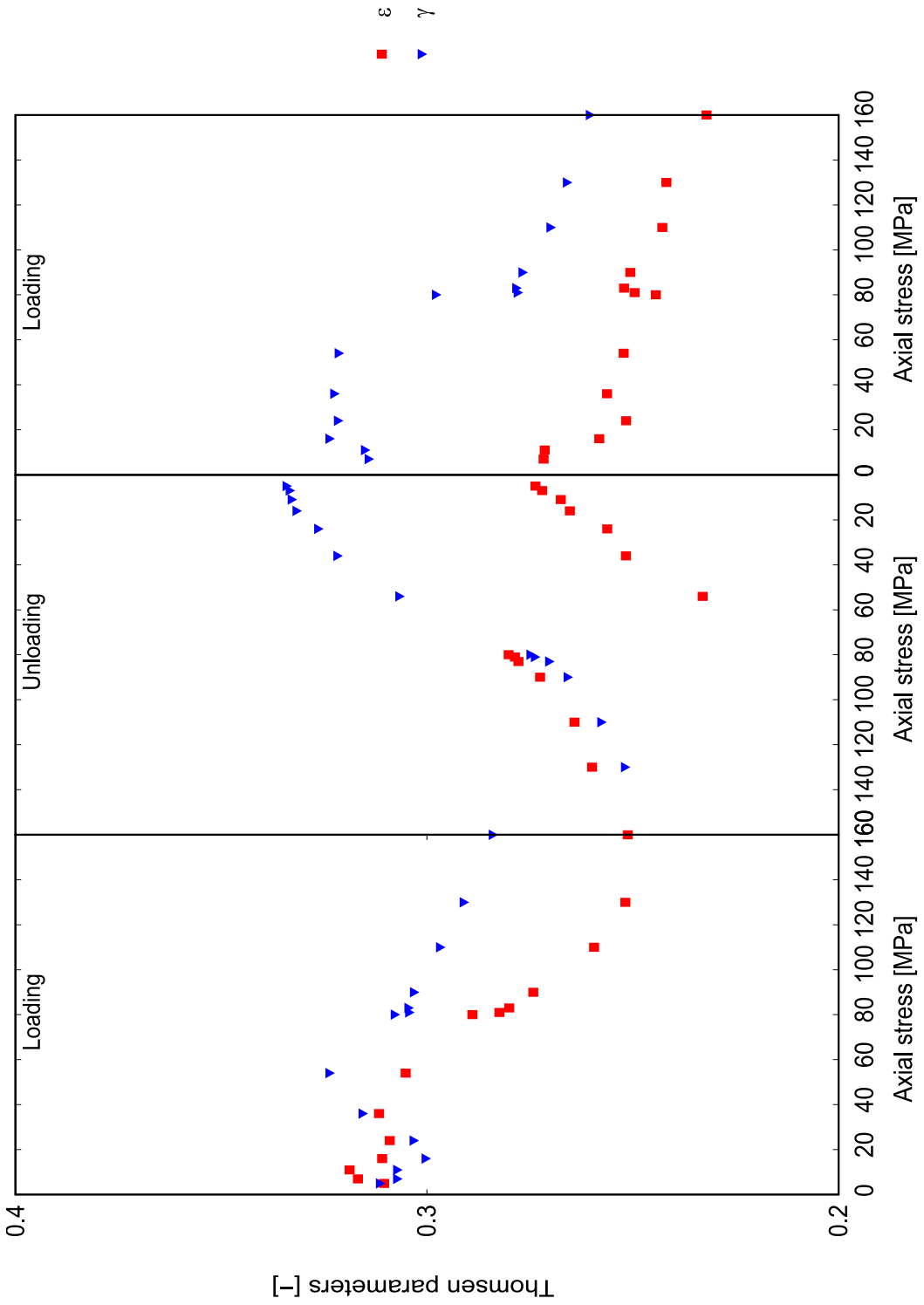

Figure 7.12: *HR1-VTI sample, Thomsen Parameters as a function of stress.*

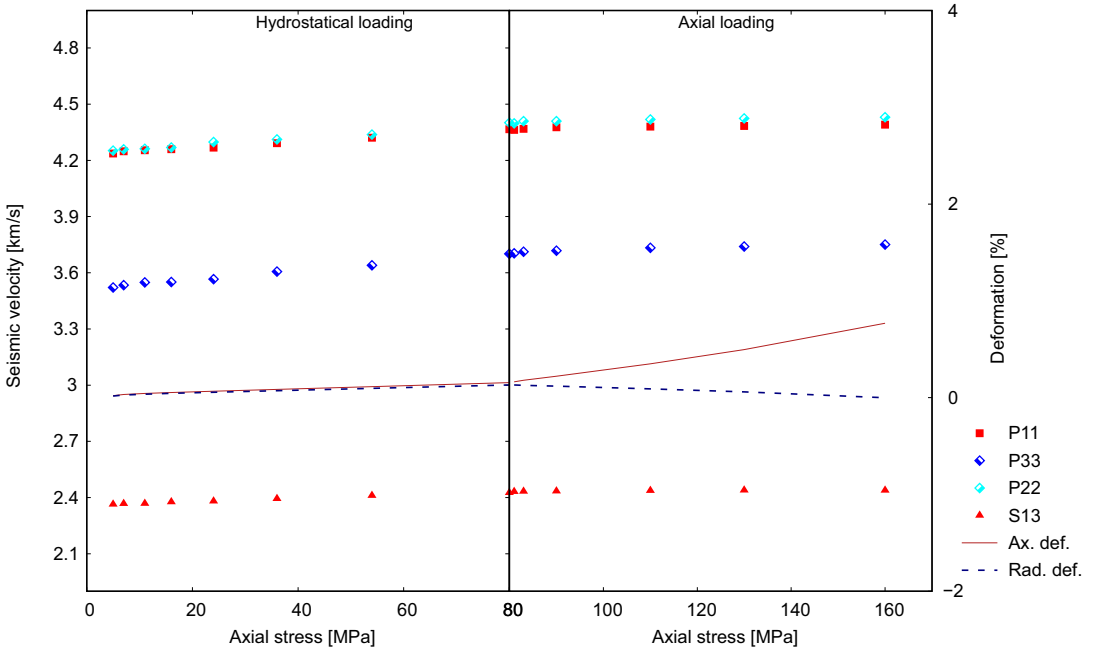

Figure 7.13: *HR1-HTI-1 sample, seismic velocities during the first loading cycle: hydrostatic loading on the left and differential axial loading on the right. Notation of velocities: red squares – P-axial; light blue and dark blue diamonds – P-radial in parallel direction and in perpendicular direction to the layering respectively; red triangles – S-axial with polarization perpendicular to the bedding. Red solid line denotes measured axial deformations. Blue dashed line displays estimated radial deformations.*

7.2.4 HTI sample HR1

In this section are described measurement results of the seismically orthorhombic (initially HTI) sample HR1. To determine all necessary velocities were carried out two experiments: HR1-HTI-1 and HR1-HTI-2 (abbreviation HTI refers to initial HTI symmetry of the sample). For both experiments was used the same sample. The sample had no visible cracks or any other damages after the first experiment. For reasons of simplicity, the first loading cycle is described separately and then the description is extended for the complete loading path.

HR1-HTI-1, first loading cycle

The hydrostatic loading affects all measured velocities, the shape of the velocity increase has a non-linear form, see Figure 7.13. Both velocities of the P-wave, propagated parallel to the layering in the axial direction P_{11} and in the radial direction P_{22} demonstrate similar shapes and confirm the visually observed HTI symmetry. P_{33} displays significantly lower velocity, indicating notable initial anisotropy. The deformations during the hydrostatic loading are negligible.

The differential axial loading has less influence on the velocities, because of the compaction of the sample during the hydrostatic loading. It is interesting that during the axial loading all measured velocities increase with comparable magnitude. The complete velocity increase for the hydrostatic loading plus the axial loading stages is as follows: P_{11} rises by 3.6%, P_{22} by 4.2%, P_{33} by 6.5%, S_{13} by 3.1 %. The deformation in the axial direction starts to grow notably during the axial loading, but does not exceed 1%.

HR1-HTI-1, complete loading path

The observed hysteresis is negligible for both, the ultrasonic velocities and the deformations, see Appendix C, Figure C.5. The shapes of the velocity and the deformation curves are almost symmetrical for the loading and the unloading cycles. A notable deformation occurs during the differential axial loading, but completely recovers after the unloading.

Interpretation and discussion

The measured velocities and deformations recover to initial values after the unloading, indicating a reversible deformation of the pore space. Generally, the sample is "room dry" (stored under room humidity conditions) and relatively stiff. The increase of all measured velocities during the differential axial loading may be related to the stress conditions: the sample was already loaded during the hydrostatic loading stage and is laterally restricted by the hydrostatic stress. This prevents the sample from expanding and partly transforms the axial stress component into the radial stress component.

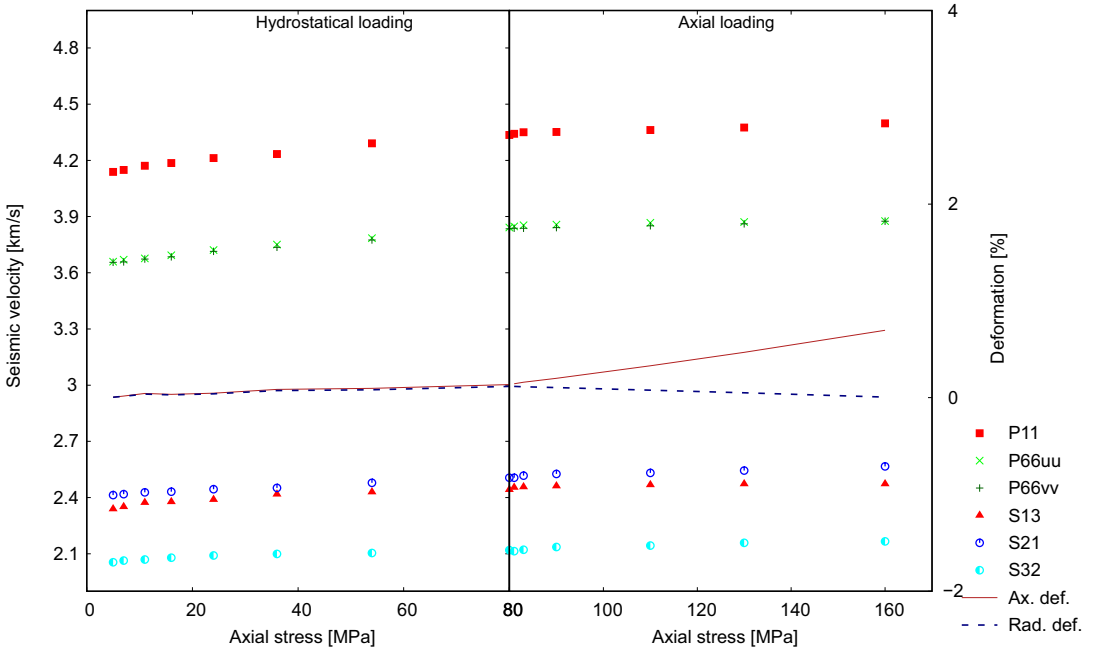

Figure 7.14: *HR1-HTI-2 sample, seismic velocities during the first loading cycle: hydrostatic loading on the left and differential axial loading on the right. Velocities notation: red squares – P-axial; light green and dark green crosses – P-radial under* $45°$ *to both vertical symmetry planes (exactly in between of them); red triangles – S-axial with polarization perpendicular to the bedding; blue open circles – S-radial with polarization parallel to the bedding; cyan half-open circles – S-radial with polarization perpendicular to the bedding. Red solid line denotes measured axial deformations. Blue dashed line displays estimated radial deformations.*

HR1-HTI-2, first loading cycle

The hydrostatic loading impacts all measured velocities, inducing a non-linear increase, see Figure 7.14. The velocities of the two mutually perpendicular P-waves, propagated in the radial direction under 45° to the layering P_{66uu} and P_{66vv}, demonstrate similar shapes and lower values in comparison to the P-wave propagated parallel to the layering P_{11}. This confirms the visually observed HTI anisotropy of the sample. Deformations are negligibly small.

The differential axial loading affects all measured velocities. The elastic waves propagated in the loading direction exhibit the strongest change. The axially propagated P_{11} shows the maximal velocity increase, which equals 6.3% in comparison to the unstressed state. The axial deformations rise intensively in comparison to the hydrostatic loading, but do not exceed 1%.

HR1-HTI-2, complete loading path

The behavior of the stress-dependent velocities is almost symmetrical during the two loading and one unloading cycles, the observed hysteresis is non-significant, see Appendix C, Figure C.6. Deformations during the hydrostatic loading are negligibly small, and during the differential axial loading deformations are notable. During the axial unloading, the sample returns to its initial state.

Interpretation and discussion

The observations indicate a reversible character of the pore space deformation. The initial anisotropy lies around the magnitude of 0.2 (in absolute units) and changes by up to 17% during the loading (relative to the initial value), see Figure 7.15. The two anisotropy parameters, related to the P-waves, ε_1 and ε_2, display similar shapes and similar magnitudes. Both decrease during the loading, and the decrease is more significant during the hydrostatic part of the loading. Both parameters tend to increase during the unloading. The anisotropy parameters related to the S-waves demonstrate more complicated stress dependencies. The parameter γ_1 (is related to the two axially propagated S-waves with polarization parallel and perpendicular to the layering) increases during the loading and decreases during the unloading. It is interesting that the impact of the hydrostatic part is nearly the same as the impact of the differential axial part. The anisotropy parameter γ_2 (is related to the "fast" axial S_{12} and to the "slow" radial S_{32} velocities) increases moderately during the loading and decreases slowly during the unloading (slight changes).

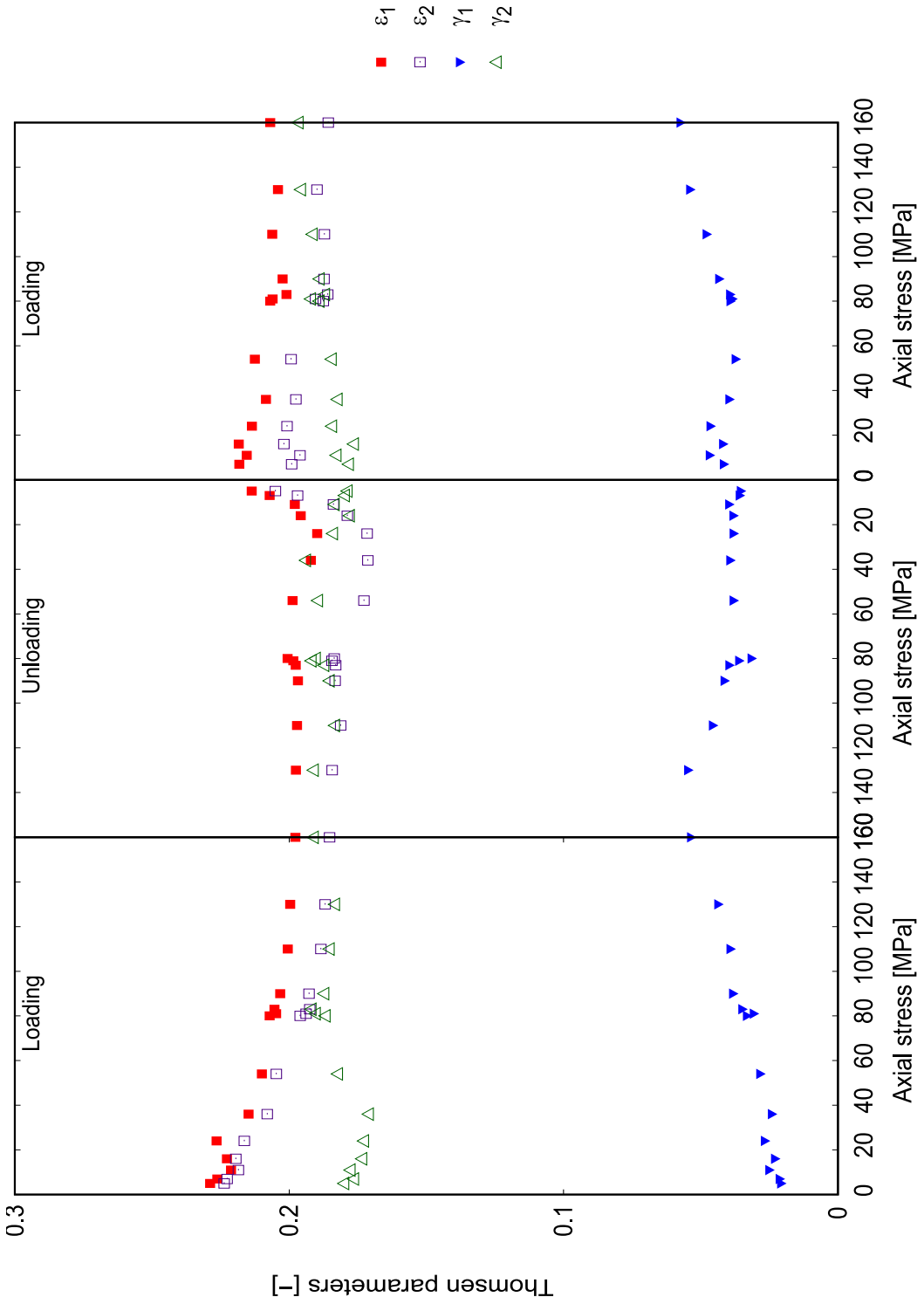

Figure 7.15: *HR1-HTI sample, the anisotropy parameters as function of stress.*

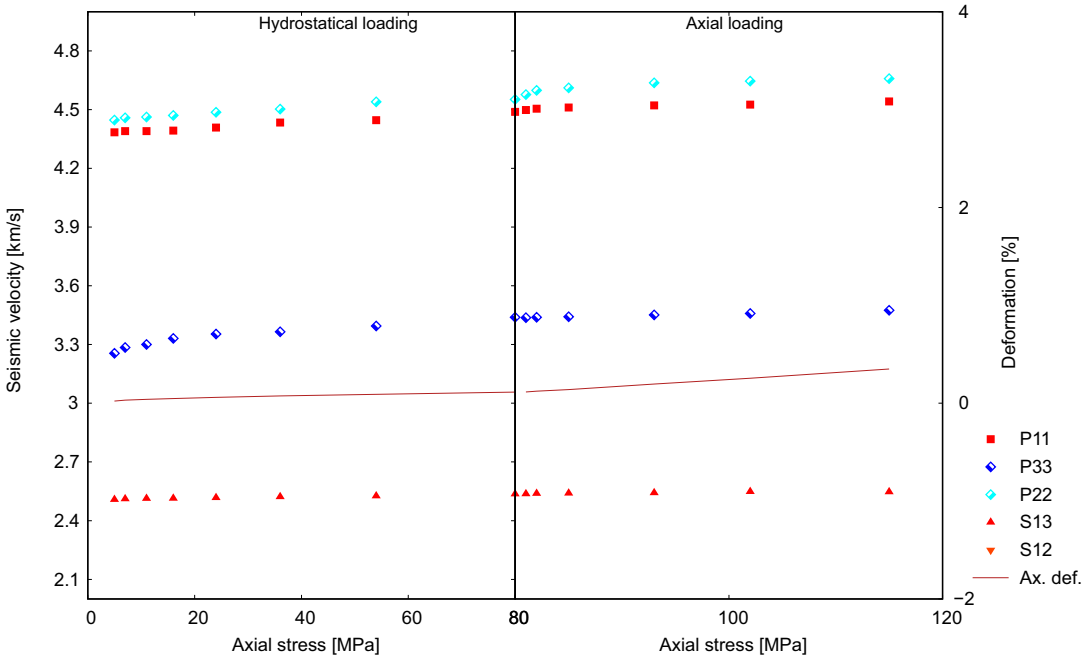

Figure 7.16: *FB1-HTI-1 sample, seismic velocities during the first loading cycle: hydrostatic loading on the left and differential axial loading on the right. The notation of velocities: red squares – P-axial; light blue and dark blue diamonds – P-radial in parallel and perpendicular to the layering directions correspondingly; red triangles – S-axial with polarization perpendicular to the bedding. Red solid line denotes measured axial deformations.*

7.2.5 HTI sample FB1

The sample FB1 was described as a stable, partially saturated, well consolidated sample. The samples were stored under in-situ humidity conditions. The hysteresis and the deformations are rather slight and the signal quality is above the average.

In this section are described the measurements of an seismically orthorhombic medium. The measurements of all required ultrasonic velocities were carried out during the two similar experiments: FB1-HTI-1 and FB1-HTI-2 (abbreviation HTI refers to initial HTI symmetry of the sample). The two experiments were needed for installation of the transducers in the all required directions. The same sample was used for both experiments. Here, the first loading cycle is introduced separately, and then the description is expanded for the complete loading path.

FB1-HTI-1, first loading cycle

The hydrostatic loading affects all measured velocities, inducing a nonlinear increase of them, see Figure 7.16. The velocities of the P-waves P_{11} and P_{22} (propagated parallel to the layering in the axial and in the radial directions) increase similarly by 2.4%. The velocity of P_{33} (propagated in the radial direction perpendicular to the layering) rises by 5.7%. The axially propagated S_{13} increases by 1.1%. The measured axial deformations are non-significant.

The differential axial loading affects all measured P-wave velocities, while the S-wave velocities increase only slightly. The radially propagated P_{22} shows the greatest rise. The axial deformation is more significant in comparison to the hydrostatic part, but still lies below 0.4%.

FB1-HTI-1, complete loading path

The observed hysteresis is not significant, the shapes of velocities and deformations are similar for the two loading and one unloading stages, see Appendix C, Figure C.7. The velocities recover to their initial values after the unloading stage and repeat the maximal values during the first and the second loading stages. The deformations in the axial direction during the hydrostatic loading/unloading are not significant, while deformations during the differential axial loading/unloading are notable, but reversible.

Interpretation and discussion

Several interesting observations were made during the considered experiment. The P_{22} (propagated in the radial direction parallel to the layering) is faster and its velocity increases more significantly than the P_{11} (propagated in the axial direction parallel to the layering). The greatest increase of the velocity demonstrates the radially propagated P_{33}. A possible explanation relate these observations to the saturation and to the possible inhomogeneities or micro-cracks.

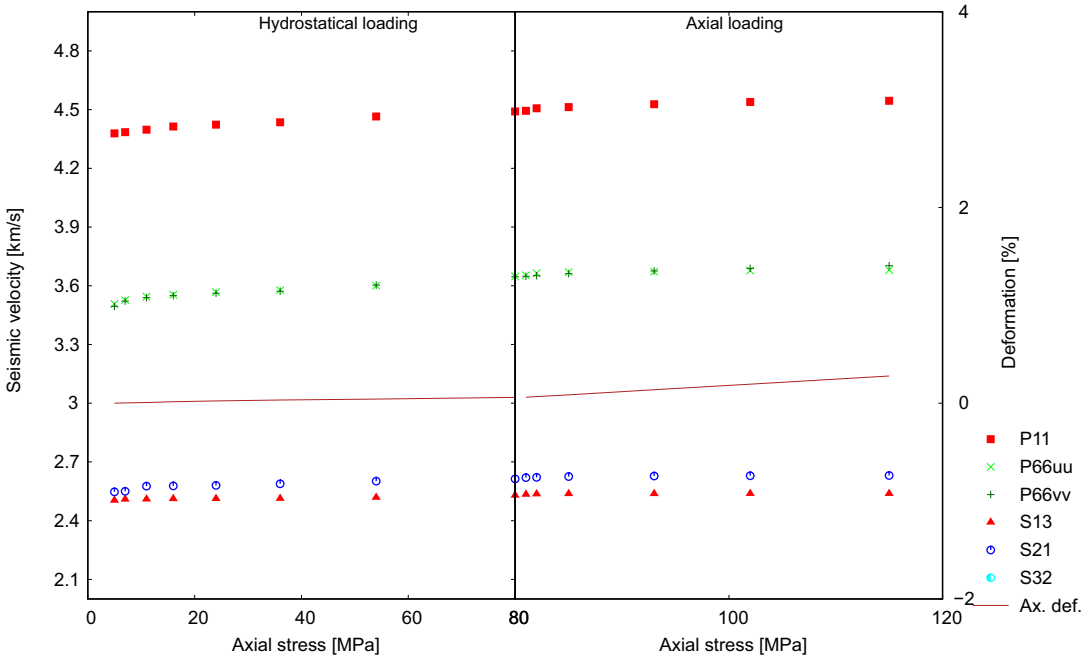

Figure 7.17: *FB1-HTI-2 sample, seismic velocities during the first loading cycle: hydrostatic loading on the left and differential axial loading on the right. The velocities notation: red squares – P-axial; light green and dark green crosses – P-radial under* $45°$ *to both vertical symmetry planes (exactly in between of them); red triangles – S-axial with polarization perpendicular to the bedding; blue open circles – S-radial with polarization parallel to the bedding; cyan half-open circles – S-radial with polarization perpendicular to the bedding. Red solid line denotes measured axial deformations.*

FB1-HTI-2, first loading cycle

The hydrostatic loading significantly influences all measured velocities, leading to their nonlinear increase, see Figure 7.17. The velocities of the elastic waves propagated in the radial direction demonstrate more significant increase in comparison to the velocities of the waves propagated in the axial direction. The two mutually perpendicular P_{66uu} and P_{66vv} (propagated in the radial direction at an angle of $45°$ to the symmetry plane) display similar values and confirm expected seismic symmetry of the medium. The measured axial deformation is negligible.

FB1-HTI-2, complete loading path

The observed repeatability of the velocities during the second loading cycle indicates a non-significant hysteresis, see Appendix C, Figure C.8. The deformation curves also demonstrate a symmetrical shape. Both observation indicate the reversible pore space deformation.

Interpretation and discussion

The initial anisotropy parameters, related to the P-waves, ε_1 and ε_2 show similar behavior and display a notable values above 0.4 (in absolute units), see Figure 7.18. Their stress dependency shares the trends and for the both parameters is provided a single description. The anisotropy decreases significantly during the hydrostatic loading and decreases slightly during the differential axial loading. They increase slightly during the axial unloading and rise significantly during the hydrostatic unloading. All changes have a symmetrical shape. The second loading cycle is similar to the first loading cycle.

The anisotropy parameter γ_1 demonstrates a low initial value of 0.02 (absolute units), it increases significantly during the hydrostatic loading and rises slightly during the differential axial loading. Then it slightly decreases during the axial unloading and decreases significantly during the hydrostatic unloading. The anisotropy parameter γ_2 could not be determined due to the technical difficulties, which occurred by the measurements of S_{32}.

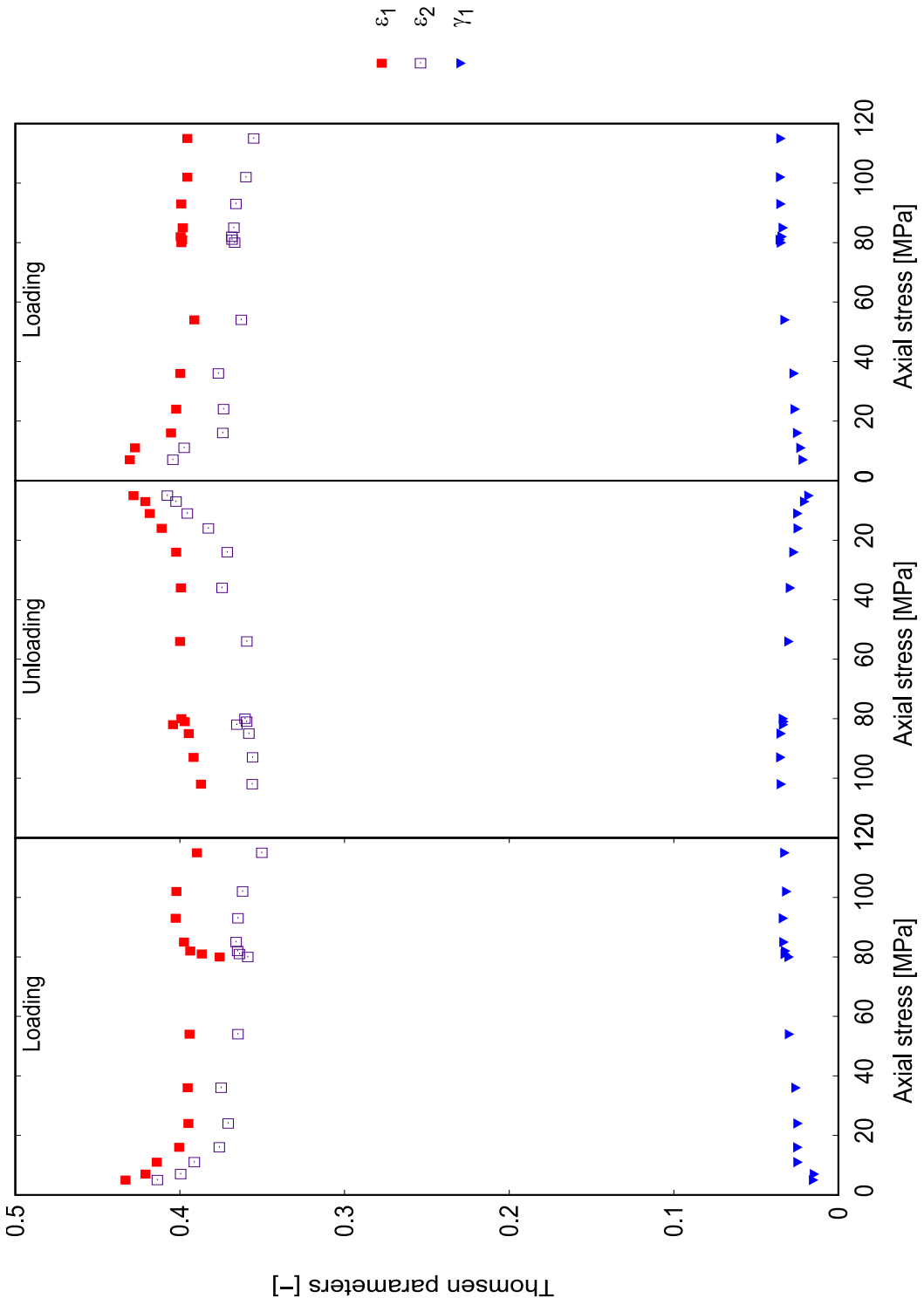

Figure 7.18: *FB1-HTI sample, the anisotropy parameters as a function of stress.*

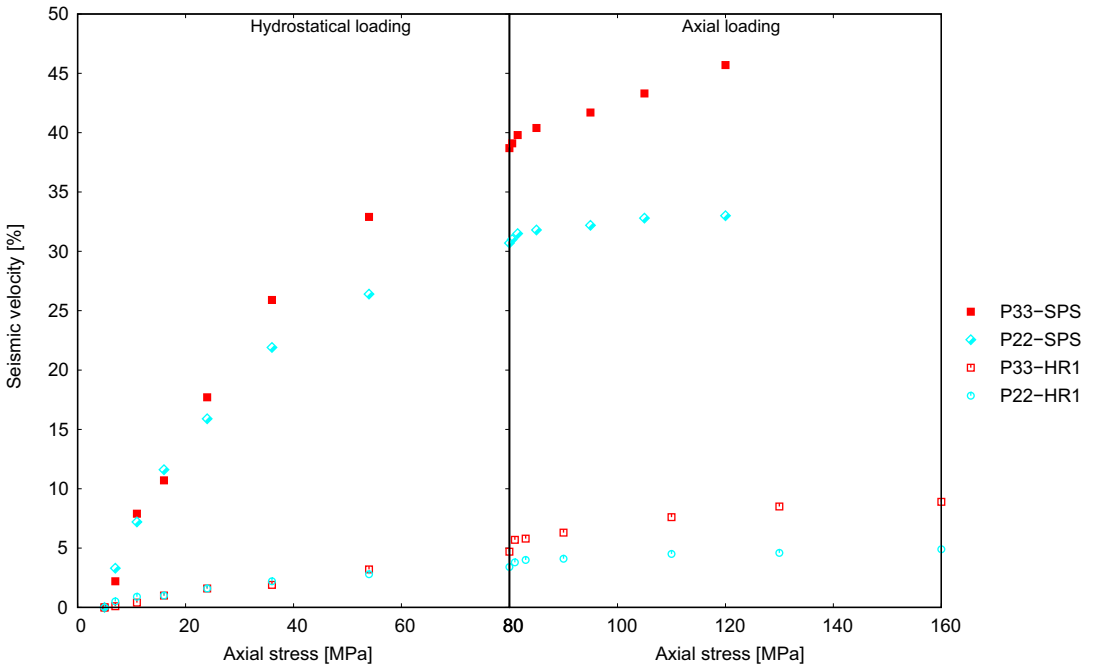

Figure 7.19: *Comparison of the stress-dependent P-wave velocity increase for SPS-VTI and HR1-VTI samples. The velocity is displayed as an increase relative to the initial value, in percent.*

7.3 Overview of measured velocities

Here, are compared the velocity increase for samples SPS-VTI and HR1-VTI. The velocity increase is displayed in percent units, each value is related to itself in an unloaded state. This comparison is shown to demonstrate the differences between the considered samples. Each sample has an individual genesis, mineralogy, lithology and compaction, which explains a very significant differences of the stress-dependent velocity changes. Nevertheless, the trends are similar for both samples and this indicates the uniqueness of involved physical mechanisms (in the first approximation).

Chapter 8

Application of the porosity deformation approach

Abstract

In this section is described application of the porosity deformation approach (PDA) to the triaxial data set. This enables a direct comparison of laboratory measurements with the numerical modelling for validation and further analysis. As intermediate product were obtained and compared experimentally measured and theoretically modeled compliance tensors, ultrasonic velocities and anisotropy parameters. The modelling of the VTI medium is performed using equations set 2.52. Theoretical background and a description of the PDA can be found in section 2.5.

8.1 VTI sample HR1

The porosity deformation approach was applied to the hydrostatic part of the triaxial loading. The modelling results expressed in terms of compliances reveal a nonlinear form of the stress-dependency between 0 and 15 MPa and a linear form of the dependency in the area of higher stresses, see Figure 8.1. All four independent diagonal terms of the compliance tensor S_{11}, S_{33}, S_{44}, S_{66} show a significant decrease. The non-diagonal S_{13} displays an increase.
The modelled compliances were calculated into the velocities and anisotropy parameters (lines), and compared to the experimentally observed (points), see Figure 8.2, Figure 8.3. The calculated velocities fit measured trends and describe a nonlinear part in the low stresses area. The maximal velocity discrepancy between the measured and modelled values is equal to 0.7%. The anisotropy parameters tend to decrease, however the changes are very slight. The compliant porosity was estimated using equation 2.54 and results 0.005 %.

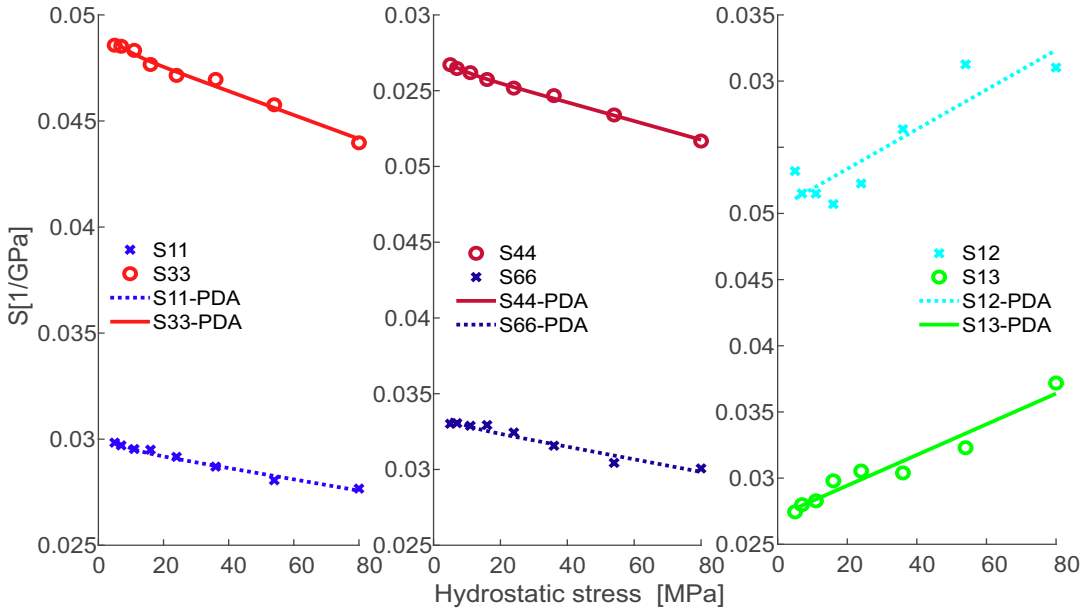

Figure 8.1: *Sample HR1-VTI. Components of the compliance tensor versus the hydrostatic stress. Points indicate experimentally determined values, lines display the data obtained by the PDA approach.*

Interpretation

The shape of the stress dependency indicates the close of compliant porosity in the stress area under 15 MPa. The linear part of the stress dependency is significant and can be explained by the deformation of the stiff porosity. Another indication of the significant influence of the stiff porosity is the increase of the non-diagonal term of the compliance tensor S_{13}. This increase is assumed to be a consequence of the stiff porosity deformation.

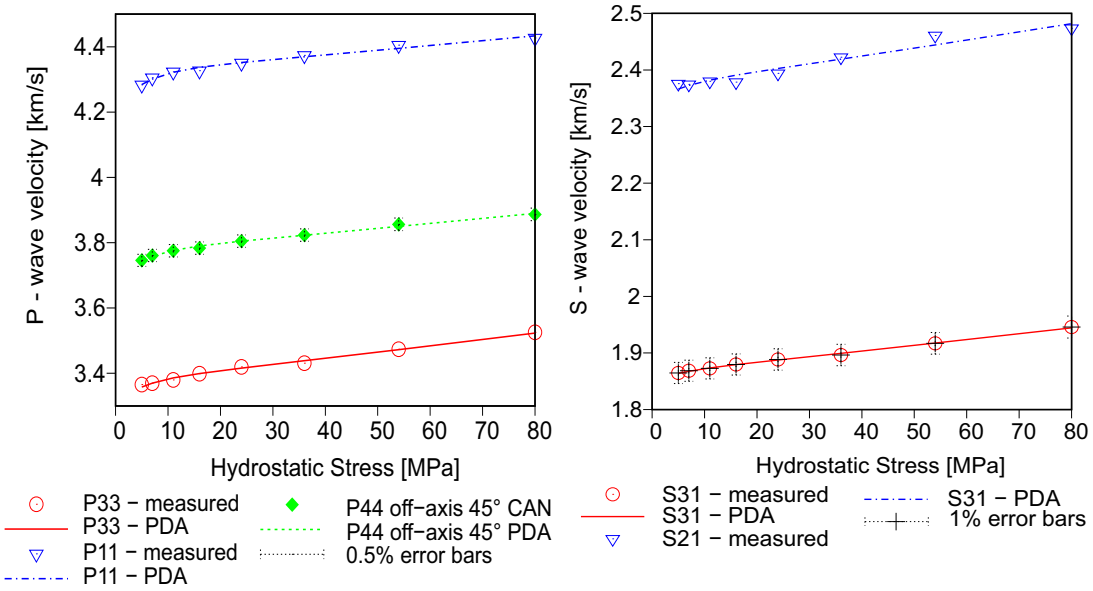

Figure 8.2: *Sample HR1-VTI, ultrasonic velocities as function of the uniaxial stress. Points indicate experimentally observed velocities, lines represent velocities modeled with the PDA approach, see Figure 8.1.*

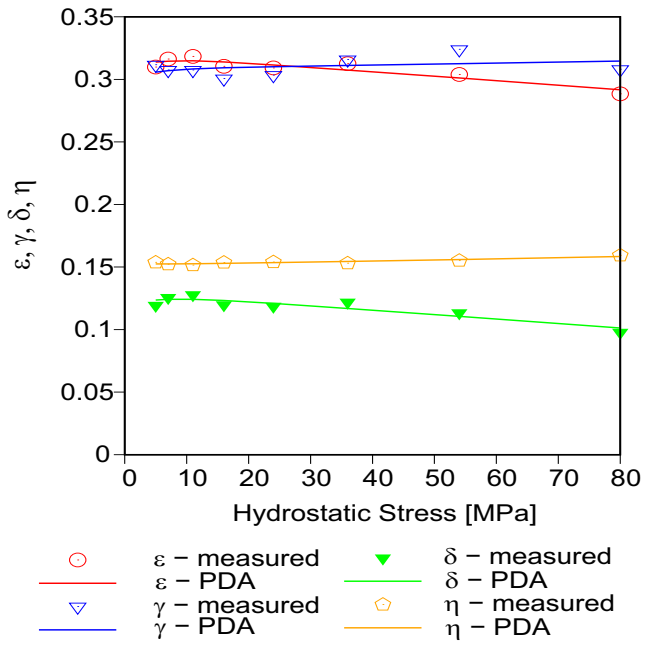

Figure 8.3: *Sample HR1-VTI, anisotropy parameters as function of the uniaxial stress. Points indicate experimentally observed values, lines represent anisotropy parameters modeled with the PDA approach, see Figure 8.1.*

Chapter 9

Conclusions

This thesis presents theoretical and experimental study of the stress-dependent elasticity. To the theoretical results belong: introduction and application of the constant anellipticity approach; introduction of the concept: "orthorhombic anisotropy due to an imperfect disorder"; modelling of the stress distribution in an uniaxially loaded sample. The main theoretical result is an application of the porosity deformation approach (PDA) on the data set obtained by measuring of uniaxially and triaxially loaded, vertical transverse isotropic (VTI) and orthorhombic shales. The PDA was applied on the four VTI and one orthorhombic samples. The stress-induced alteration of the ultrasonic velocities and anisotropies were modelled and analyzed. The role of the stiff porosity and the volume of the compliant porosity were estimated.

To the experimental results belong: preparation, density measurements and mineralogical description of nine anisotropic samples; thirteen experiments under uniaxial and triaxial loading conditions, with simultaneous measurements of stress-dependent deformations and seismic velocities.

The porosity deformation approach is one of the few theoretically based approaches, which describes the dependence of rock elasticity, and thus seismic velocities, upon confining stress and pore pressure, without any geometrical assumption about the pore space configuration. This approach represents an extension of the previously introduced Piezosensitivity theory, which was limited to isotropic rocks under isostatic load. The actual extension is working with any type of anisotropy under any loading conditions. It enables a rock-physical interpretation of observed seismic velocities as a function of the stress in terms of already established and new physical quantities. The main objective of this work was to validate the theoretical results by analyzing stress-dependent ultrasonic velocities observed for a variety of anisotropic samples. The porosity deformation approach relates stress-dependence of seismic velocities to the deformation of the pore space. Thus, physical considerations about the mechanism of pore space deformation and empirically based assumptions are used to derive a quite general description of stress-dependent rock elasticity. The pore space is described in terms of a tensorial quantity, the generalized porosity and is separated into two parts: stiff porosity and compliant porosity. Contribution of the pore space deformation to the stress-dependency of elastic parameters depends on the porosity type.

In frame of this work was shown, that for a significant part of the samples, the influence of the compliant porosity deformation is much more significant than the influence of the stiff porosity deformation. Using PDA tools were estimated the volume of the stiff and compliant pore spaces. Deformation of the compliant porosity relates to the direction of the stress application. For example, uniaxially applied loading causes deformation of the compliant porosity, oriented normally (or nearly normally) to the direction of the stress application. This describes a significant change of elastic parameters along the direction of the stress application. While, the stiff porosity is partly deformed disregarding to the direction of the stress application, deformation of the stiff porosity shows much less influence on the elastic parameters. This explains significant increase of the P-wave velocity in the direction of the uniaxial loading and non-significant change in the orthogonal direction. In terms of the compliance tensor, the influence of stiff porosity deformation is illustrated by a slight change of the non-diagonal elements of the compliance

matrix (e.g. S_{13}). These observations are applicable for studied VTI and orthorhombic samples with different lithologies and under different loading conditions. The results of the modelled compliance tensor were calculated in to the seismic velocities and compared to the experimentally observed velocities. This has shown, that the uniaxial stress changes the anisotropy, but does not impact the anellipticity parameter. Collection of the substantial data bank, and a comparison between the uniaxial and triaxial data sets demonstrated applicability and uniqueness of the theoretical approach.

The constant anellipticity approach, developed in frame of this work, is aimed to estimate stress-dependent off-axis (under an inclination to the symmetry axis) velocities. It proposes the anellipticity parameter η' to be stress-independent. Here, anellipticity is defined as a difference between the anisotropy parameters Epsilon and Delta. Application of the CAN shows acceptable results and confirms the proposed stress independence of η'. The greatest uncertainty causes estimation of the initial off-axis velocity (in an unloaded state) and not the estimation of its stress-dependency. The constant anellipticity approach was applied to the four VTI data sets. Two data sets were incomplete and the CAN proved itself as a useful tool for estimation of missing off-axis velocity.

Open questions and outlook

An interesting question and a possible future application of the porosity deformation approach is a prediction of the stress-dependent parameters. The concept assumes "learning" of the modelling constants using the experimental data set and following prediction of the stress-dependent elastic parameters under various stress conditions. This would be a great tool for modelling of different possible scenarios in the subsurface medium during production or exploration. As an exemplary experimental data bank can be considered a triaxial data set provided in the Part III of this dissertation. In these experiments, the loading path is separated into two stages, the stage with hydrostatic loading and the stage with differential axial loading. The PDA is assumed to "learn" the modelling constants during the first stage and predict the results of the second stage. Measured data can be compared with the theoretically predicted data for further analysis. If the residuum is acceptable and the modelling results are reproducible for different lithologies, one can demonstrate and verify the prediction option.

ACKNOWLEDGEMENTS

I would like to thank my research advisers PD Dr. Sibylle I. Mayr and Prof. Dr. Serge A. Shapiro for guiding me throughout the duration of my PhD and for the support. They gave me a rare opportunity to carry out a very interesting research and I have learned an incredible amount of information in the past few years. Thanks to these people we upgraded a rock-physics laboratory and made possible further experimental activity. I would like to thank the Freie Universität Berlin for the organisation. I want to thank Anna Giribaldi, Dr. Ralf Milke, Sabine Meister and Ramona Niemann assisted with thin sections preparation, the electron microscope measurements, preparation and interpretation of SEM images. I want to thank Jan Evers for professional photos of the samples and laboratory equipment. I would like to thank "Gesteinslabor Jahns" for the cooperation, Dr. Eberhard Jahns and Hasjörg Baumgarten for their professional assistance and advice. I am grateful to Annette Schmid-Röhl for the personal communication professional advice. I would like to thank Dr Frans Kets for the very valuable discussions. I want to thank Taisiya Biryaltseva for the programming assistance. I would like to thank all my colleagues for the help and for the support. I want to thank my friends and my family for the mental energy.
The research was carried out in the frame of the DGMK-project 741. We thank the companies EMPG (Hannover), Neptune Energy, DEA Deutsche Erdoel AG and Wintershall Holding GmbH (Kassel) for financing the project, providing of the samples, discussions and authorization to present the results. I would like to thank the PHASE consortium for the financing of the project.

Appendices

Appendix A

Tables of velocities

Stress [MPa]	P_{33}	P_{11}	S_{31}	S_{21}	P_{44}
1.2	4.803	5.368	2.882	3.240	5.106
2.8	4.827	5.370	2.890	3.240	5.116
5.4	4.844	5.372	2.900	3.242	5.126
8.2	4.858	5.378	2.905	3.244	5.131
10.6	4.870	5.381	2.911	3.246	5.133
15.9	4.886	5.386	2.922	3.248	5.135
21.0	4.900	5.388	2.925	3.248	5.139
26.2	4.915	5.391	2.930	3.249	5.140
31.4	4.922	5.391	2.936	3.252	5.142

Table A.1: *Experimentally determined seismic velocities in the BaZ-VTI sample. Uniaxial stress was applied along the axis x_3. The sample was measured in room dry state, the density of the sample is equal to 2720 kg/m^3. Velocities are provided in [km/s] units. V_{44} is the off-axis (quasi P-wave) velocity measured under an angle of $\theta = 64°$ to the symmetry axis.*

Stress [MPa]	P_{33}	P_{11}	S_{31}	S_{21}	P_{44}
1.3	2.942	4.139	1.930	2.413	3.541
2.5	2.960	4.144	1.940	2.420	3.551
3.8	2.990	4.156	1.950	2.420	3.569
5.1	3.008	4.147	1.958	2.421	3.570
7.6	3.051	4.139	1.968	2.437	3.582
10.2	3.089	4.143	1.972	2.428	3.599
12.7	3.116	4.146	1.980	2.431	3.611

Table A.2: *Measured seismic velocities in the DH06-VTI sample. Uniaxial stress was applied along the axis x_3. The sample was measured in room dry state, the density of the sample is equal to 2210 kg/m^3. Velocities are displayed in [km/s] units. The provided in Table P_{44} velocity was not measured experimentally, but estimated by constant anellipticity approach (CAN). P_{44} is the off-axis (quasi P-wave) velocity under an angle of $\theta = 45°$ to the symmetry axis.*

Stress [MPa]	P_{33}	P_{11}	S_{31}	S_{21}	P_{44}
1.7	4.779	5.224	3.015	3.162	5.130
2.7	4.784	5.224	3.015	3.162	5.138
5.2	4.799	5.225	3.018	3.163	5.144
7.9	4.820	5.225	3.022	3.165	5.147
10.6	4.833	5.225	3.024	3.166	5.151
15.5	4.851	5.226	3.027	3.170	5.156
20.4	4.880	5.228	3.033	3.171	5.165
25.4	4.919	5.231	3.038	3.173	5.182
30.8	4.943	5.234	3.041	3.176	5.185

Table A.3: *Experimentally determined seismic velocities in the DR-VTI sample. Uniaxial stress was applied along the axis x_3. The sample was measured in room dry state, the density of the sample is equal to 2540 kg/m^3. Velocities are provided in [km/s] units. Vp_{44} is the quasi P-wave off-axis velocity measured under an angle of $\theta = 64^\circ$ to the symmetry axis.*

Stress [MPa]	P_{11}	P_{22}	P_{33}	P_{44}	P_{55}	P_{66}	S_{12}	S_{13}	S_{32}
2	4.999	5.067	4.651	4.652	5.079	4.873	3.059	2.873	2.853
3	5.009	5.071	4.646	4.656	5.082	4.873	3.061	2.874	2.854
6	5.021	5.071	4.652	4.658	5.085	4.878	3.063	2.877	2.855
8	5.029	5.073	4.645	4.666	5.083	4.876	3.065	2.880	2.856
11	5.037	5.077	4.649	4.669	5.089	4.878	3.068	2.882	2.855
14	5.042	5.081	4.653	4.676	5.087	4.879	3.070	2.883	2.856
17	5.049	5.084	4.645	4.677	5.086	4.875	3.073	2.884	2.856
22	5.056	5.086	4.650	4.683	5.092	4.879	3.076	2.886	2.857
27	5.061	5.086	4.651	4.680	5.099	4.877	3.079	2.887	2.858
33	5.067	5.088	4.651	4.689	5.102	4.877	3.082	2.889	2.859

Table A.4: *Measured seismic velocities in the orthorhombic DR-ORT sample. Uniaxial stress was applied along the axis x_1 The sample was measured in room dry state, the density of the sample is equal to 2540 kg/m^3. Velocities are displayed in [km/s] units.*

Loading path [Mpa]			Deformations [%]		Ultrasonic velocities [km/s]					Thomsen parameters [-]	
σ_c	$\Delta\sigma_{ax}$	σ_{ax}	ε_{ax}	ε_{rad}	Vp11	Vp22	Vp33	Vs21	Vs31	ε	γ
5	0	5	0.233	0.164	3.091	2.872	2.486	1.879	1.757	0.273	0.072
7	0	7	0.909	0.645	3.151	2.966	2.541	1.900	1.774	0.269	0.073
11	0	11	1.573	1.187	3.218	3.079	2.683	1.898	1.786	0.219	0.065
16	0	16	2.208	1.675	3.221	3.207	2.753	1.930	1.800	0.184	0.075
24	0	24	2.907	2.296	3.355	3.330	2.925	1.954	1.862	0.157	0.051
36	0	36	3.625	2.812	3.503	3.502	3.131	2.022	1.877	0.126	0.080
54	0	54	4.339	3.284	3.642	3.632	3.303	2.062	1.879	0.108	0.102
80	0	80	4.955	3.731	3.758	3.753	3.448	2.122	1.930	0.094	0.104
80	0.5	80.5	5.056	3.731	3.773	3.762	3.457	2.128	1.935	0.096	0.105
80	1.5	81.5	5.144	3.700	3.786	3.778	3.474	2.135	1.935	0.094	0.109
80	5	85	5.278	3.654	3.791	3.786	3.491	2.143	1.947	0.090	0.106
80	15	95	5.653	3.524	3.814	3.797	3.522	2.151	1.962	0.086	0.101
80	25	105	6.143	3.348	3.827	3.813	3.561	2.159	1.970	0.078	0.100
80	40	120	7.044	3.009	3.841	3.820	3.623	2.158	1.979	0.062	0.095
80	25	105	6.921	3.009	3.853	3.830	3.602	2.176	1.977	0.072	0.105
80	15	95	6.808	3.051	3.851	3.831	3.583	2.182	1.973	0.078	0.112
80	5	85	6.666	3.103	3.852	3.832	3.561	2.182	1.962	0.085	0.118
80	1.5	81.5	6.611	3.123	3.852	3.837	3.557	2.182	1.956	0.086	0.122
80	0.5	80.5	6.587	3.132	3.854	3.840	3.553	2.188	1.956	0.088	0.126
80	0	80	6.578	3.134	3.860	3.849	3.551	2.187	1.955	0.091	0.126
54	0	54	6.368	3.134	3.767	3.747	3.448	2.130	1.925	0.097	0.112
36	0	36	6.144	2.964	3.671	3.633	3.325	2.071	1.889	0.109	0.101
24	0	24	5.932	2.804	3.560	3.494	3.199	2.011	1.828	0.119	0.105
16	0	16	5.735	2.646	3.482	3.364	3.062	1.907	1.765	0.146	0.084
11	0	11	5.568	2.495	3.302	3.303	2.964	1.864	1.754	0.121	0.065
7	0	7	5.409	2.328	3.178	3.206	2.935	1.819	1.749	0.086	0.040
5	0	5	5.251	2.158	3.131	3.160	2.895	1.773	1.751	0.085	0.013
7	0	7	5.315	2.158	3.176	3.168	2.737	1.867	1.812	0.173	0.031
11	0	11	5.409	2.236	3.269	3.194	2.844	1.877	1.889	0.160	-0.007
16	0	16	5.531	2.340	3.365	3.313	2.934	1.917	1.947	0.157	-0.015
24	0	24	5.694	2.479	3.458	3.410	3.065	1.957	1.951	0.136	0.003
36	0	36	5.891	2.629	3.599	3.581	3.218	2.028	1.953	0.125	0.040
54	0	54	6.118	2.801	3.725	3.697	3.371	2.115	1.996	0.110	0.061
80	0	80	6.373	2.978	3.857	3.846	3.535	2.186	2.010	0.095	0.092
80	0.5	80.5	6.382	2.978	3.863	3.852	3.541	2.191	2.007	0.095	0.096
80	1.5	81.5	6.401	2.972	3.867	3.855	3.549	2.196	2.012	0.094	0.095
80	5	85	6.451	2.955	3.877	3.868	3.561	2.194	2.014	0.093	0.093
80	15	95	6.629	2.895	3.885	3.871	3.588	2.202	2.024	0.086	0.092
80	25	105	6.894	2.803	3.892	3.887	3.617	2.209	2.029	0.079	0.093
80	40	120	7.383	2.629	3.905	3.894	3.664	2.208	2.037	0.068	0.087

Table A.5: *SPS-VTI: Table of velocities and Thomsen parameters. All velocities displayed in [km/s] units. $\Delta\sigma_{ax}$ indicates differential axial loading.*

Loading path [Mpa]			Deformations [%]		Ultrasonic velocities [km/s]					Thomsen parameters [-]			
σ_c	$\Delta\sigma_{ax}$	σ_{ax}	ε_{ax}	ε_{rad}	Vp11	Vp22	Vp33	Vs12	Vs13	ε_1	ε_2	γ_1	γ_2
5	0	5	0.073	0.057	3.072	3.052	2.884	2.106	1.792	0.060	0.067	0.191	0.447
7	0	7	0.348	0.274	3.103	3.178	2.937	2.157	1.804	0.085	0.058	0.215	0.443
11	0	11	0.657	0.504	3.197	3.296	2.975	2.208	1.834	0.114	0.078	0.225	0.421
16	0	16	0.971	0.733	3.320	3.387	3.100	2.302	1.875	0.097	0.073	0.254	0.450
24	0	24	1.310	0.961	3.446	3.524	3.193	2.392	1.909	0.109	0.082	0.284	0.418
36	0	36	1.655	1.198	3.643	3.784	3.350	2.459	1.986	0.138	0.091	0.267	0.340
54	0	54	2.065	1.510	3.829	3.870	3.618	2.532	2.056	0.072	0.060	0.259	0.298
80	0	80	2.577	1.851	3.998	4.166	3.779	2.663	2.144	0.108	0.060	0.271	0.296
80	1	81	2.637	1.851	3.990	4.173	3.767	2.711	2.152	0.114	0.061	0.294	0.315
80	3	83	2.720	1.808	4.032	4.157	3.795	2.720	2.155	0.100	0.064	0.296	0.311
80	10	90	2.939	1.693	4.031	4.176	3.800	2.723	2.161	0.104	0.063	0.294	0.309
80	30	110	3.800	1.294	4.084	4.200	3.821	2.741	2.193	0.104	0.071	0.281	0.315
80	50	130	5.067	0.710	4.108	4.262	3.832	2.769	2.221	0.118	0.075	0.278	0.324
80	80	160	12.713	0.262	4.163	3.849	3.521	2.720	2.159	0.097	0.199	0.294	0.290
80	50	130	12.464	0.262	4.134	3.950	3.683	2.715	2.207	0.075	0.130	0.256	0.280
80	30	110	12.201	0.326	4.110	3.935	3.659	2.705	2.201	0.078	0.131	0.255	0.279
80	10	90	11.826	0.456	4.065	4.006	3.654	2.693	2.196	0.101	0.119	0.252	0.268
80	3	83	11.660	0.528	4.044	4.026	3.668	2.688	2.197	0.102	0.108	0.248	0.266
80	1	81	11.589	0.567	4.047	4.061	3.672	2.686	2.197	0.112	0.107	0.247	0.262
80	0	80	11.558	0.602	4.035	4.097	3.671	2.684	2.195	0.123	0.104	0.248	0.262
54	0	54	11.394	0.602	3.986	3.872	3.532	2.635	2.143	0.101	0.137	0.256	0.273
36	0	36	11.196	0.322	3.800	3.820	3.355	2.557	2.017	0.148	0.142	0.304	0.265
24	0	24	11.006	0.073	3.667	3.618	3.174	2.487	1.923	0.150	0.167	0.336	0.258
16	0	16	10.832	-0.147	3.493	3.462	3.058	2.399	1.800	0.141	0.152	0.388	0.243
11	0	11	10.689	-0.335	3.298	3.095	2.825	2.331	1.727	0.100	0.181	0.411	0.244
7	0	7	10.558	-0.529	3.194	2.965	2.763	2.272	1.690	0.076	0.168	0.403	0.267
5	0	5	10.438	-0.738	3.045	1.794	2.621	2.163	1.675	-0.266	0.175	0.334	0.207
7	0	7	10.468	-0.738	3.049	2.843	2.641	2.228	1.694	0.080	0.167	0.365	0.244
11	0	11	10.518	-0.670	3.196	2.974	2.700	2.262	1.730	0.107	0.201	0.355	0.230
16	0	16	10.589	-0.567	3.280	3.234	2.952	2.337	1.755	0.100	0.118	0.387	0.259
24	0	24	10.686	-0.429	3.478	3.516	3.101	2.408	1.871	0.143	0.129	0.328	0.255
36	0	36	10.798	-0.249	3.650	3.643	3.372	2.503	1.984	0.084	0.086	0.296	0.256
54	0	54	10.913	-0.072	3.818	3.856	3.489	2.587	2.089	0.111	0.099	0.267	0.250
80	0	80	11.014	0.095	4.016	4.190	3.717	2.689	2.203	0.135	0.084	0.245	0.275
80	1	81	11.024	0.095	4.022	4.080	3.794	2.690	2.205	0.078	0.062	0.244	0.270
80	3	83	11.054	0.083	4.027	4.135	3.737	2.695	2.207	0.112	0.081	0.245	0.271
80	10	90	11.136	0.046	4.039	4.239	3.727	2.701	2.213	0.147	0.087	0.245	0.272
80	30	110	11.426	-0.072	4.109	4.262	3.777	2.721	2.216	0.137	0.092	0.254	0.282
80	50	130	11.803	-0.179	4.162	4.223	3.755	2.746	2.233	0.132	0.114	0.256	0.295

Table A.6: *SPS-HTI-1: Table of velocities and Thomsen parameters. All velocities displayed in [km/s] units. $\Delta\sigma_{ax}$ indicates differential axial loading.*

Loading path [Mpa]			Deformations [%]		Ultrasonic velocities [km/s]						
σ_c	$\Delta\sigma_{ax}$	σ_{ax}	ε_{ax}	ε_{rad}	Vp11	Vp66uu	Vp66vv	Vs12	Vs13	Vs21	Vs32
5	0	5	0.047	0.060	3.192	3.094	2.968	1.457	1.826	1.948	1.530
7	0	7	0.132	0.167	3.231	3.097	2.992	1.488	1.867	1.968	1.571
11	0	11	0.265	0.323	3.334	3.222	3.106	1.541	1.910	2.025	1.627
16	0	16	0.450	0.506	3.512	3.257	3.207	1.602	1.992	2.069	1.670
24	0	24	0.696	0.900	3.679	3.350	3.298	1.676	2.076	2.147	1.765
36	0	36	0.981	1.138	3.854	3.459	3.511	1.796	2.188	2.248	1.898
54	0	54	1.312	1.531	4.010	3.672	3.702	1.899	2.244	2.337	2.004
80	0	80	1.696	1.851	4.129	3.842	3.846	1.988	2.302	2.422	2.111
80	0.5	80.5	1.744	1.851	4.142	3.857	3.858	1.995	2.305	2.432	2.124
80	2	82	1.788	1.840	4.148	3.867	3.872	2.001	2.311	2.436	2.135
80	5	85	1.868	1.819	4.163	3.877	3.880	2.007	2.315	2.444	2.141
80	15	95	2.122	1.754	4.176	3.885	3.894	2.019	2.324	2.454	2.147
80	25	105	2.459	1.671	4.201	3.907	3.917	2.037	2.339	2.460	2.156
80	40	120	3.088	1.514	4.223	3.926	3.942	2.091	2.361	2.473	2.164
80	25	105	2.996	1.514	4.218	3.935	3.942	2.077	2.361	2.474	2.174
80	15	95	2.912	1.533	4.209	3.938	3.941	2.069	2.358	2.474	2.167
80	5	85	2.810	1.556	4.189	3.934	3.946	2.062	2.352	2.473	2.173
80	2	82	2.771	1.564	4.185	3.937	3.948	2.059	2.348	2.471	2.171
80	0.5	80.5	2.754	1.568	4.183	3.936	3.948	2.060	2.353	2.469	2.175
80	0	80	2.748	1.570	4.180	3.933	3.948	2.060	2.349	2.468	2.174
54	0	54	2.609	1.570	4.112	3.853	3.872	2.014	2.305	2.428	2.119
36	0	36	2.464	0.954	4.030	3.773	3.826	1.965	2.272	2.357	2.066
24	0	24	2.330	0.395	3.933	3.715	3.749	1.927	2.211	2.300	2.020
16	0	16	2.208	-0.057	3.835	3.571	3.721	1.911	2.189	2.262	1.968
11	0	11	2.108	-0.304	3.799	3.490	3.595	1.876	2.007	2.200	1.911
7	0	7	2.018	-0.476	3.670	3.401	3.519	1.856	1.876	2.096	1.834
5	0	5	1.938	-0.670	3.628	3.321	3.436	1.846	1.832	2.052	1.819
7	0	7	1.958	-0.670	3.638	3.350	3.450	1.775	1.869	2.085	1.827
11	0	11	1.998	-0.518	3.675	3.409	3.589	1.779	1.907	2.142	1.872
16	0	16	2.060	-0.258	3.743	3.505	3.591	1.795	2.010	2.203	1.897
24	0	24	2.148	0.141	3.840	3.585	3.720	1.860	2.188	2.279	1.960
36	0	36	2.260	0.612	3.944	3.718	3.753	1.923	2.222	2.334	2.036
54	0	54	2.393	1.171	4.050	3.806	3.848	1.977	2.272	2.411	2.112
80	0	80	2.551	1.841	4.167	3.910	3.913	2.039	2.331	2.456	2.160
80	0.5	80.5	2.562	1.841	4.176	3.919	3.916	2.044	2.332	2.467	2.168
80	2	82	2.581	1.837	4.178	3.929	3.926	2.049	2.340	2.469	2.171
80	5	85	2.623	1.827	4.197	3.936	3.933	2.055	2.344	2.472	2.173
80	15	95	2.749	1.797	4.213	3.940	3.942	2.063	2.353	2.480	2.176
80	25	105	2.919	1.757	4.230	3.948	3.948	2.073	2.366	2.484	2.177
80	40	120	3.246	1.681	4.247	3.957	3.961	2.085	2.376	2.487	2.179

Table A.7: *SPS-HTI-2: Table of velocities and Thomsen parameters. All velocities displayed in [km/s] units. $\Delta\sigma_{ax}$ indicates differential axial loading.*

Loading path [Mpa]			Deformations [%]		Ultrasonic velocities [km/s]					Thomsen parameters [-]	
σ_c	$\Delta\sigma_{ax}$	σ_{ax}	ε_{ax}	ε_{rad}	Vp11	Vp22	Vp33	Vs21	Vs31	ε	γ
5	0	5	0.025	0.013	4.285	4.282	3.366	2.376	1.865	0.310	0.312
7	0	7	0.034	0.018	4.307	4.304	3.370	2.375	1.869	0.317	0.308
11	0	11	0.061	0.032	4.325	4.322	3.380	2.380	1.873	0.319	0.308
16	0	16	0.084	0.045	4.328	4.325	3.399	2.379	1.880	0.311	0.301
24	0	24	0.120	0.064	4.350	4.351	3.420	2.394	1.889	0.309	0.304
36	0	36	0.177	0.093	4.371	4.376	3.431	2.422	1.896	0.312	0.316
54	0	54	0.264	0.138	4.408	4.401	3.474	2.461	1.917	0.305	0.324
80	0	80	0.398	0.212	4.428	4.426	3.525	2.474	1.946	0.289	0.308
80	1	81	0.419	0.212	4.448	4.445	3.556	2.476	1.952	0.282	0.305
80	3	83	0.457	0.200	4.449	4.454	3.562	2.480	1.955	0.280	0.305
80	10	90	0.538	0.175	4.450	4.459	3.576	2.485	1.960	0.274	0.303
80	30	110	0.774	0.101	4.461	4.474	3.620	2.491	1.973	0.259	0.297
80	50	130	1.037	0.016	4.477	4.478	3.651	2.495	1.983	0.252	0.291
80	80	160	1.512	-0.132	4.492	4.493	3.665	2.498	1.995	0.251	0.284
80	50	130	1.280	-0.132	4.484	4.501	3.637	2.469	2.013	0.260	0.252
80	30	110	1.094	-0.077	4.473	4.478	3.618	2.472	2.008	0.264	0.258
80	10	90	0.885	-0.015	4.466	4.467	3.593	2.474	1.999	0.273	0.266
80	3	83	0.806	0.007	4.457	4.462	3.574	2.475	1.994	0.278	0.271
80	1	81	0.774	0.016	4.449	4.450	3.565	2.479	1.992	0.279	0.274
80	0	80	0.759	0.020	4.445	4.446	3.558	2.480	1.992	0.280	0.275
54	0	54	0.606	0.020	4.277	4.285	3.532	2.465	1.940	0.233	0.307
36	0	36	0.482	-0.045	4.247	4.237	3.464	2.440	1.903	0.252	0.322
24	0	24	0.396	-0.090	4.213	4.200	3.426	2.427	1.887	0.256	0.327
16	0	16	0.336	-0.121	4.197	4.180	3.392	2.419	1.876	0.265	0.332
11	0	11	0.296	-0.142	4.180	4.160	3.374	2.408	1.866	0.267	0.333
7	0	7	0.266	-0.157	4.167	4.147	3.353	2.403	1.861	0.272	0.334
5	0	5	0.241	-0.170	4.153	4.127	3.339	2.399	1.857	0.274	0.334
7	0	7	0.249	-0.170	4.164	4.134	3.352	2.371	1.858	0.272	0.314
11	0	11	0.263	-0.162	4.170	4.161	3.358	2.379	1.863	0.271	0.315
16	0	16	0.285	-0.150	4.187	4.164	3.401	2.397	1.867	0.258	0.324
24	0	24	0.322	-0.131	4.201	4.180	3.426	2.410	1.880	0.252	0.322
36	0	36	0.376	-0.103	4.228	4.204	3.438	2.426	1.891	0.256	0.323
54	0	54	0.458	-0.060	4.269	4.249	3.481	2.454	1.914	0.252	0.322
80	0	80	0.582	0.010	4.326	4.297	3.545	2.468	1.953	0.244	0.298
80	1	81	0.601	0.010	4.337	4.308	3.542	2.476	1.985	0.250	0.278
80	3	83	0.635	0.000	4.349	4.320	3.546	2.483	1.990	0.252	0.279
80	10	90	0.708	-0.022	4.365	4.351	3.563	2.487	1.995	0.251	0.277
80	30	110	0.927	-0.086	4.387	4.380	3.599	2.490	2.006	0.243	0.270
80	50	130	1.164	-0.156	4.413	4.403	3.623	2.493	2.014	0.242	0.266
80	80	160	1.561	-0.277	4.438	4.428	3.668	2.497	2.024	0.232	0.261

Table A.8: *HR1-VTI: Table of velocities and Thomsen parameters. All velocities displayed in [km/s] units. $\Delta\sigma_{ax}$ indicates differential axial loading.*

Loading path [Mpa]			Deformations [%]		Ultrasonic velocities [km/s]				Thomsen parameters [-]			
σ_c	$\Delta\sigma_{ax}$	σ_{ax}	ε_{ax}	ε_{rad}	Vp11	Vp22	Vp33	Vs13	ε_1	ε_2	γ_1	γ_2
5	0	5	0.020	0.016	4.237	4.252	3.522	2.364	0.229	0.224	0.021	0.180
7	0	7	0.033	0.028	4.248	4.259	3.534	2.368	0.226	0.223	0.022	0.176
11	0	11	0.043	0.036	4.254	4.262	3.549	2.368	0.221	0.218	0.025	0.177
16	0	16	0.053	0.045	4.259	4.269	3.551	2.376	0.223	0.219	0.023	0.173
24	0	24	0.067	0.056	4.268	4.298	3.566	2.381	0.226	0.216	0.027	0.172
36	0	36	0.086	0.072	4.292	4.312	3.606	2.394	0.215	0.208	0.024	0.171
54	0	54	0.114	0.096	4.321	4.337	3.640	2.410	0.210	0.205	0.029	0.182
80	0	80	0.155	0.131	4.366	4.401	3.701	2.426	0.207	0.196	0.034	0.186
80	1	81	0.163	0.131	4.363	4.397	3.704	2.432	0.205	0.194	0.031	0.190
80	3	83	0.180	0.128	4.369	4.409	3.712	2.433	0.205	0.192	0.035	0.191
80	10	90	0.221	0.119	4.376	4.409	3.718	2.434	0.203	0.193	0.039	0.187
80	30	110	0.350	0.091	4.380	4.419	3.733	2.437	0.201	0.188	0.040	0.185
80	50	130	0.496	0.060	4.383	4.424	3.740	2.439	0.200	0.187	0.044	0.183
80	80	160	0.769	-0.001	4.391	4.430	3.750	2.439	0.198	0.185	0.054	0.191
80	50	130	0.621	-0.001	4.384	4.427	3.748	2.436	0.198	0.184	0.055	0.191
80	30	110	0.510	0.024	4.367	4.418	3.741	2.435	0.197	0.181	0.046	0.183
80	10	90	0.391	0.049	4.366	4.409	3.735	2.432	0.197	0.183	0.042	0.185
80	3	83	0.348	0.058	4.358	4.404	3.729	2.431	0.198	0.183	0.040	0.187
80	1	81	0.331	0.061	4.356	4.400	3.723	2.430	0.199	0.184	0.036	0.191
80	0	80	0.324	0.063	4.346	4.400	3.717	2.430	0.201	0.184	0.032	0.190
54	0	54	0.264	0.063	4.302	4.385	3.709	2.412	0.199	0.173	0.038	0.189
36	0	36	0.217	0.023	4.268	4.333	3.683	2.395	0.192	0.171	0.040	0.193
24	0	24	0.185	-0.004	4.251	4.308	3.668	2.379	0.190	0.172	0.038	0.184
16	0	16	0.164	-0.022	4.234	4.286	3.634	2.364	0.196	0.179	0.038	0.178
11	0	11	0.149	-0.034	4.225	4.269	3.613	2.351	0.198	0.184	0.040	0.183
7	0	7	0.138	-0.043	4.220	4.251	3.574	2.342	0.207	0.197	0.036	0.179
5	0	5	0.126	-0.052	4.214	4.240	3.549	2.331	0.214	0.205	0.036	0.178
7	0	7	0.129	-0.052	4.191	4.248	3.544	2.325	0.218	0.199	0.042	0.178
11	0	11	0.133	-0.049	4.197	4.255	3.557	2.328	0.215	0.196	0.047	0.182
16	0	16	0.141	-0.042	4.220	4.269	3.561	2.344	0.218	0.202	0.042	0.176
24	0	24	0.158	-0.029	4.237	4.276	3.579	2.354	0.214	0.201	0.047	0.184
36	0	36	0.179	-0.010	4.260	4.293	3.607	2.379	0.208	0.198	0.040	0.182
54	0	54	0.210	0.015	4.289	4.330	3.627	2.403	0.212	0.199	0.038	0.184
80	0	80	0.250	0.050	4.340	4.401	3.701	2.425	0.207	0.188	0.040	0.189
80	1	81	0.258	0.050	4.356	4.405	3.707	2.427	0.206	0.190	0.039	0.192
80	3	83	0.274	0.046	4.361	4.409	3.723	2.428	0.201	0.186	0.040	0.187
80	10	90	0.313	0.038	4.369	4.417	3.727	2.429	0.202	0.187	0.044	0.189
80	30	110	0.438	0.010	4.370	4.430	3.728	2.435	0.206	0.187	0.048	0.191
80	50	130	0.575	-0.019	4.386	4.431	3.734	2.435	0.204	0.190	0.054	0.195
80	80	160	0.804	-0.076	4.402	4.470	3.759	2.438	0.207	0.186	0.058	0.196

Table A.9: *HR1-HTI-1: Table of velocities and Thomsen parameters. All velocities displayed in [km/s] units. $\Delta\sigma_{ax}$ indicates differential axial loading.*

Loading path [Mpa]			Deformations [%]		Ultrasonic velocities [km/s]					
σ_c	$\Delta\sigma_{ax}$	σ_{ax}	ε_{ax}	ε_{rad}	Vp11	Vp66uu	Vp66vv	Vs13	Vs21	Vs32
5	0	5	0.005	0.004	4.138	3.659	3.656	2.339	2.414	2.054
7	0	7	0.017	0.014	4.149	3.670	3.658	2.350	2.418	2.064
11	0	11	0.043	0.037	4.171	3.677	3.674	2.373	2.428	2.069
16	0	16	0.034	0.029	4.186	3.694	3.685	2.377	2.431	2.079
24	0	24	0.046	0.039	4.212	3.721	3.715	2.389	2.444	2.091
36	0	36	0.086	0.073	4.234	3.751	3.736	2.418	2.452	2.099
54	0	54	0.096	0.082	4.291	3.784	3.775	2.429	2.478	2.104
80	0	80	0.136	0.116	4.336	3.842	3.835	2.442	2.506	2.119
80	1	81	0.143	0.116	4.342	3.848	3.838	2.454	2.506	2.114
80	3	83	0.159	0.113	4.350	3.854	3.838	2.457	2.517	2.121
80	10	90	0.200	0.104	4.352	3.857	3.841	2.462	2.526	2.136
80	30	110	0.329	0.078	4.362	3.867	3.851	2.467	2.531	2.144
80	50	130	0.468	0.050	4.375	3.871	3.861	2.472	2.544	2.159
80	80	160	0.696	0.006	4.397	3.876	3.875	2.473	2.567	2.166
80	50	130	0.555	0.006	4.394	3.876	3.875	2.476	2.567	2.116
80	30	110	0.444	0.028	4.373	3.872	3.862	2.473	2.544	2.123
80	10	90	0.323	0.052	4.369	3.868	3.852	2.468	2.531	2.137
80	3	83	0.280	0.062	4.361	3.859	3.843	2.460	2.526	2.144
80	1	81	0.262	0.066	4.349	3.855	3.840	2.454	2.517	2.158
80	0	80	0.255	0.068	4.346	3.843	3.840	2.451	2.506	2.165
54	0	54	0.191	0.068	4.305	3.797	3.787	2.433	2.503	2.114
36	0	36	0.143	0.027	4.253	3.766	3.763	2.407	2.488	2.112
24	0	24	0.109	-0.003	4.230	3.742	3.736	2.386	2.469	2.111
16	0	16	0.085	-0.023	4.201	3.723	3.709	2.362	2.453	2.091
11	0	11	0.070	-0.035	4.187	3.704	3.706	2.352	2.443	2.075
7	0	7	0.058	-0.045	4.162	3.685	3.687	2.341	2.425	2.066
5	0	5	0.047	-0.054	4.142	3.680	3.674	2.331	2.412	2.056
7	0	7	0.046	-0.054	4.165	3.686	3.680	2.330	2.421	2.064
11	0	11	0.047	-0.052	4.186	3.694	3.688	2.377	2.435	2.069
16	0	16	0.053	-0.048	4.200	3.719	3.707	2.379	2.441	2.084
24	0	24	0.066	-0.036	4.232	3.738	3.737	2.394	2.461	2.089
36	0	36	0.088	-0.018	4.249	3.757	3.750	2.419	2.472	2.101
54	0	54	0.119	0.008	4.287	3.796	3.786	2.434	2.492	2.114
80	0	80	0.161	0.045	4.341	3.856	3.864	2.449	2.519	2.128
80	1	81	0.165	0.045	4.353	3.859	3.864	2.456	2.520	2.125
80	3	83	0.181	0.041	4.362	3.862	3.868	2.459	2.522	2.135
80	10	90	0.221	0.033	4.370	3.866	3.871	2.465	2.533	2.140
80	30	110	0.349	0.007	4.374	3.870	3.872	2.470	2.550	2.151
80	50	130	0.486	-0.021	4.377	3.874	3.876	2.472	2.564	2.157
80	80	160	0.708	-0.074	4.397	3.879	3.881	2.473	2.575	2.166

Table A.10: *HR1-HTI-2: Table of velocities and Thomsen parameters. All velocities displayed in [km/s] units. $\Delta\sigma_{ax}$ indicates differential axial loading.*

Loading path [Mpa]			Deformations [%]		Ultrasonic velocities [km/s]				Thomsen parameters [-]			
σ_c	$\Delta\sigma_{ax}$	σ_{ax}	ε_{ax}	ε_{rad}	Vp11	Vp22	Vp33	Vs13	ε_1	ε_2	γ_1	γ_2
5	0	5	0.021	0.013	4.384	4.446	3.255	2.507	0.433	0.414	0.016	-
8	0	7	0.031	0.020	4.390	4.458	3.285	2.511	0.421	0.400	0.016	-
11	0	11	0.040	0.025	4.390	4.462	3.300	2.513	0.414	0.391	0.026	-
16	0	16	0.048	0.031	4.393	4.470	3.331	2.514	0.400	0.376	0.026	-
24	0	24	0.059	0.039	4.408	4.486	3.354	2.517	0.395	0.371	0.026	-
36	0	36	0.074	0.049	4.434	4.503	3.365	2.522	0.395	0.375	0.027	-
54	0	54	0.091	0.061	4.446	4.540	3.395	2.525	0.394	0.365	0.031	-
80	0	80	0.113	0.078	4.488	4.552	3.439	2.536	0.376	0.359	0.031	-
80	1	81	0.115	0.078	4.498	4.577	3.437	2.537	0.387	0.364	0.033	-
80	2	82	0.123	0.073	4.505	4.598	3.439	2.538	0.394	0.365	0.033	-
80	5	85	0.140	0.061	4.511	4.611	3.442	2.540	0.398	0.366	0.034	-
80	13	93	0.195	0.022	4.522	4.637	3.451	2.542	0.403	0.365	0.034	-
80	22	102	0.255	-0.019	4.526	4.645	3.458	2.548	0.402	0.362	0.033	-
80	35	115	0.349	-0.085	4.542	4.658	3.475	2.547	0.390	0.350	0.034	-
80	22	102	0.274	-0.085	4.539	4.632	3.478	2.539	0.387	0.356	0.036	-
80	13	93	0.223	-0.050	4.520	4.628	3.465	2.537	0.392	0.356	0.036	-
80	5	85	0.173	-0.014	4.509	4.619	3.453	2.536	0.395	0.358	0.036	-
80	2	82	0.155	-0.002	4.500	4.615	3.432	2.536	0.404	0.365	0.034	-
80	1	81	0.149	0.003	4.493	4.611	3.439	2.535	0.397	0.359	0.034	-
80	0	80	0.147	0.004	4.487	4.607	3.432	2.533	0.399	0.361	0.035	-
54	0	54	0.130	0.004	4.477	4.598	3.427	2.529	0.400	0.359	0.031	-
36	0	36	0.119	-0.003	4.465	4.544	3.388	2.522	0.399	0.374	0.030	-
24	0	24	0.110	-0.009	4.442	4.535	3.376	2.518	0.402	0.371	0.028	-
16	0	16	0.101	-0.015	4.429	4.515	3.345	2.516	0.411	0.383	0.026	-
11	0	11	0.093	-0.019	4.420	4.490	3.313	2.513	0.418	0.396	0.026	-
8	0	7	0.085	-0.023	4.410	4.470	3.294	2.511	0.421	0.402	0.022	-
5	0	5	0.076	-0.029	4.395	4.458	3.272	2.507	0.428	0.408	0.019	-
8	0	7	0.081	-0.029	4.401	4.478	3.283	2.509	0.430	0.404	0.022	-
11	0	11	0.087	-0.025	4.407	4.494	3.300	2.511	0.427	0.397	0.024	-
16	0	16	0.094	-0.020	4.413	4.507	3.349	2.514	0.405	0.374	0.026	-
24	0	24	0.104	-0.014	4.435	4.523	3.367	2.517	0.402	0.373	0.027	-
36	0	36	0.116	-0.005	4.461	4.535	3.381	2.522	0.400	0.377	0.028	-
54	0	54	0.128	0.003	4.471	4.560	3.416	2.525	0.391	0.363	0.033	-
80	0	80	0.145	0.015	4.490	4.590	3.423	2.528	0.399	0.367	0.036	-
80	1	81	0.147	0.015	4.503	4.598	3.430	2.529	0.399	0.368	0.036	-
80	2	82	0.152	0.012	4.510	4.607	3.434	2.533	0.400	0.368	0.035	-
80	5	85	0.167	0.001	4.523	4.619	3.446	2.536	0.398	0.367	0.035	-
80	13	93	0.218	-0.034	4.527	4.628	3.451	2.537	0.399	0.366	0.036	-
80	22	102	0.271	-0.072	4.535	4.641	3.468	2.538	0.395	0.360	0.036	-
80	35	115	0.356	-0.132	4.538	4.654	3.478	2.541	0.396	0.355	0.036	-

Table A.11: *FB1-HTI-1: Table of velocities and Thomsen parameters. All velocities displayed in [km/s] units. $\Delta\sigma_{ax}$ indicates differential axial loading.*

Loading path [Mpa]			Deformations [%]		Ultrasonic velocities [km/s]				
σ_c	$\Delta\sigma_{ax}$	σ_{ax}	ε_{ax}	ε_{rad}	Vp11	Vp66uu	Vp66vv	Vs13	Vs21
5	0	5	0.001	0.000	4.379	3.507	3.495	2.504	2.548
8	0	7	0.003	0.002	4.385	3.527	3.522	2.509	2.550
11	0	11	0.008	0.005	4.398	3.544	3.540	2.510	2.577
16	0	16	0.015	0.010	4.413	3.554	3.550	2.512	2.578
24	0	24	0.023	0.015	4.423	3.567	3.562	2.512	2.581
36	0	36	0.032	0.021	4.435	3.577	3.573	2.513	2.589
54	0	54	0.043	0.029	4.465	3.601	3.604	2.518	2.602
80	0	80	0.060	0.041	4.490	3.648	3.646	2.529	2.613
80	1	81	0.062	0.041	4.494	3.654	3.649	2.534	2.620
80	2	82	0.068	0.037	4.507	3.664	3.651	2.536	2.621
80	5	85	0.085	0.025	4.513	3.670	3.662	2.537	2.625
80	13	93	0.138	-0.012	4.528	3.672	3.675	2.537	2.628
80	22	102	0.194	-0.051	4.539	3.678	3.689	2.538	2.630
80	35	115	0.278	-0.110	4.545	3.681	3.703	2.538	2.631
80	22	102	0.204	-0.110	4.538	3.678	3.686	2.539	2.628
80	13	93	0.151	-0.073	4.520	3.672	3.678	2.538	2.627
80	5	85	0.099	-0.036	4.519	3.670	3.662	2.537	2.625
80	2	82	0.081	-0.024	4.503	3.662	3.657	2.534	2.621
80	1	81	0.074	-0.019	4.500	3.659	3.649	2.533	2.620
80	0	80	0.072	-0.017	4.490	3.648	3.643	2.529	2.619
54	0	54	0.050	-0.017	4.471	3.619	3.614	2.521	2.606
36	0	36	0.037	-0.026	4.458	3.598	3.588	2.517	2.597
24	0	24	0.028	-0.032	4.423	3.572	3.570	2.512	2.587
16	0	16	0.019	-0.038	4.413	3.562	3.557	2.511	2.579
11	0	11	0.012	-0.042	4.401	3.552	3.545	2.510	2.577
8	0	7	0.005	-0.046	4.391	3.534	3.532	2.507	2.565
5	0	5	0.000	-0.049	4.375	3.517	3.515	2.504	2.554
8	0	7	0.000	-0.049	4.388	3.529	3.527	2.508	2.565
11	0	11	0.005	-0.046	4.401	3.547	3.540	2.511	2.570
16	0	16	0.012	-0.041	4.413	3.560	3.547	2.512	2.578
24	0	24	0.022	-0.034	4.420	3.567	3.568	2.512	2.585
36	0	36	0.032	-0.027	4.429	3.577	3.573	2.517	2.591
54	0	54	0.043	-0.020	4.451	3.611	3.601	2.520	2.608
80	0	80	0.059	-0.009	4.474	3.640	3.641	2.527	2.617
80	1	81	0.061	-0.009	4.490	3.656	3.643	2.533	2.620
80	2	82	0.067	-0.013	4.497	3.662	3.654	2.536	2.621
80	5	85	0.084	-0.025	4.513	3.670	3.662	2.537	2.623
80	13	93	0.137	-0.062	4.524	3.672	3.670	2.537	2.627
80	22	102	0.192	-0.100	4.546	3.678	3.684	2.538	2.628
80	35	115	0.275	-0.158	4.545	3.683	3.700	2.538	2.631

Table A.12: *FB1-HTI-2: Table of velocities and Thomsen parameters. All velocities displayed in [km/s] units. $\Delta\sigma_{ax}$ indicates differential axial loading.*

Appendix B

Tables of modelling coefficients

	i	j	S_{ij}^{drs} [1/GPa]	D_{ijj} [1/GPa]	F_c^{une} [1/MPa]	residuum [-]	ϕ_i^{c0} [%]	θ_i [-]
BaZ	1	1	$13.8 \cdot 10^{-3}$	-	-	$1.8 \cdot 10^{-8}$	-	-
	3	3	$15.3 \cdot 10^{-3}$	$1.0 \cdot 10^{-3}$	0.06	$4.3 \cdot 10^{-9}$	0.02	1397
	4	4	$42.4 \cdot 10^{-3}$	-	0.06	$2.2 \cdot 10^{-8}$	-	-
	6	6	$34.9 \cdot 10^{-3}$	-	-	$6.4 \cdot 10^{-8}$	-	-
	1	3	$-1.2 \cdot 10^{-3}$	-	-	$6.8 \cdot 10^{-8}$	-	-
	3	4	-	$1.9 \cdot 10^{-3}$	-	-	-	-
DH06	1	1	$29.4 \cdot 10^{-3}$	-	-	$1.0 \cdot 10^{-7}$	-	-
	3	3	$45.5 \cdot 10^{-3}$	$9.6 \cdot 10^{-3}$	0.12	$2.8 \cdot 10^{-7}$	0.13	886
	4	4	$113 \cdot 10^{-3}$	-	0.12	$3.0 \cdot 10^{-7}$	-	-
	6	6	$77 \cdot 10^{-3}$	-	-	$1.6 \cdot 10^{-6}$	-	-
	1	3	$-2.6 \cdot 10^{-3}$	-	-	$1.2 \cdot 10^{-6}$	-	-
	3	4	-	$8.6 \cdot 10^{-3}$	-	-	-	-

Table B.1: *Modelling coefficients obtained by the PDA application on the data set of shales BaZ-VTI and DH06-VTI, see equations set 2.51.* S_{ij}^{drs} *denotes the compliance in the reference state and is not dependent on the stress.* B_{ijj} *and* F_c^{une} *are the coefficients of exponential function of the stress and represent the deformation of compliant pore space. The residuum is calculated using the least square method.*

	i	j	k	l	Voigt notation	S^{drs}_{ijkl} [1/GPa]	$4K^{\alpha}_{ijkl}$ [MPa/GPa]	$4B_{ik}$ [1/GPa]	F_c [1/MPa]	residuum [-]	ϕ^{c0}_i [−]	θ^c_i [-]
DR-VTI	1	1	1	1	11	$15.8 \cdot 10^{-3}$	$-0.5 \cdot 10^{-5}$	0	-	$5.4 \cdot 10^{-9}$	-	-
	3	3	3	3	33	$18.7 \cdot 10^{-3}$	$2.0 \cdot 10^{-5}$	0	0.25	$3.1 \cdot 10^{-8}$	n/a	n/a
	1	3	1	3	55	$41.9 \cdot 10^{-3}$	$2.5 \cdot 10^{-5}$	0	0.25	$4.7 \cdot 10^{-9}$	-	-
	1	2	1	2	66	$38.2 \cdot 10^{-3}$	$1.2 \cdot 10^{-5}$	0	-	$1.6 \cdot 10^{-9}$	-	-
	1	1	3	3	13	$-3.5 \cdot 10^{-3}$	$1.7 \cdot 10^{-5}$	-	-	$3.8 \cdot 10^{-8}$	-	-
DR-ORT	1	1	1	1	11	$17.3 \cdot 10^{-3}$	$0.6 \cdot 10^{-5}$	$0.3 \cdot 10^{-3}$	0.25	$1.0 \cdot 10^{-8}$	$1.2 \cdot 10^{-3}$	7825
	2	2	2	2	22	$18.1 \cdot 10^{-3}$	$1.2 \cdot 10^{-5}$	+	-	$5.2 \cdot 10^{-8}$	-	-
	3	3	3	3	33	$20.6 \cdot 10^{-3}$	$-0.3 \cdot 10^{-5}$	+	-	$3.3 \cdot 10^{-8}$	-	-
	2	3	2	3	44	$48.3 \cdot 10^{-3}$	$0.6 \cdot 10^{-5}$	+	-	$2.8 \cdot 10^{-9}$	-	-
	1	3	1	3	55	$47.5 \cdot 10^{-3}$	$1.1 \cdot 10^{-5}$	$0.3 \cdot 10^{-3}$	0.25	$1.7 \cdot 10^{-9}$	-	-
	1	2	1	2	66	$41.9 \cdot 10^{-3}$	$0.2 \cdot 10^{-5}$	$0.3 \cdot 10^{-3}$	0.25	$7.7 \cdot 10^{-9}$	-	-
	1	1	3	3	13	$2.4 \cdot 10^{-3}$	$2.1 \cdot 10^{-5}$	-	-	$1.5 \cdot 10^{-7}$	-	-
	2	2	3	3	23	$5.3 \cdot 10^{-3}$	$-0.9 \cdot 10^{-5}$	-	-	$9.7 \cdot 10^{-9}$	-	-
	1	1	2	2	12	$4.3 \cdot 10^{-3}$	$-1.2 \cdot 10^{-5}$	-	-	$1.6 \cdot 10^{-7}$	-	-

Table B.2: *Modelling coefficients of the DR-VTI (vertical transversely isotropic) and the DR-ORT (orthorhombic) samples. S^{drs}_{ijkl} denotes the compliance in the reference state and is not dependent on the stress. K^{α}_{iikl} is the coefficient of a linear function related to the deformation of the stiff porosity. B_{ik} and F_c are the coefficients of exponential function of the stress and represent the deformation of compliant pore space, see equations set 2.53 and 2.50. The coefficient B_{ik} is stress-dependent only along the loading direction. Otherwise, it is a constant value and it is included (subsumed) into the coefficient S^{drs}_{ijkl}. In such case, it is indicated with the symbol "+". The residuum is calculated using the least square method.*

	i	j	k	l	Voigt notation	S^{drs}_{ijkl} [1/GPa]	$4K^1_{ijkl}$ [MPa/GPa]	$4K^2_{ijkl}$ [MPa/GPa]	$4K^3_{ijkl}$ [MPa/GPa]	$4B_{ik}$ [1/GPa]	F_c [1/MPa]	residuum [-]	ϕ_i^{c0} [−]	θ_i^c [-]
HR1-VTI	1	1	1	1	11	$29.7 \cdot 10^{-3}$	$8.9 \cdot 10^{-6}$	$8.9 \cdot 10^{-6}$	$8.9 \cdot 10^{-6}$	$2.5 \cdot 10^{-4}$	0.2	$1.1 \cdot 10^{-7}$	-	-
	3	3	3	3	33	$48.7 \cdot 10^{-3}$	$18.8 \cdot 10^{-6}$	$18.8 \cdot 10^{-6}$	$18.8 \cdot 10^{-6}$	$2.5 \cdot 10^{-4}$	0.2	$2.7 \cdot 10^{-7}$	0.005	4168
	1	3	1	3	55	$123.4 \cdot 10^{-3}$	$10.3 \cdot 10^{-6}$	$10.3 \cdot 10^{-6}$	$10.3 \cdot 10^{-6}$	$2.5 \cdot 10^{-4}$	0.2	$2.3 \cdot 10^{-7}$	-	-
	1	2	1	2	66	$76.3 \cdot 10^{-3}$	$6.9 \cdot 10^{-6}$	$6.9 \cdot 10^{-6}$	$6.9 \cdot 10^{-6}$	$2.5 \cdot 10^{-4}$	0.2	$2.5 \cdot 10^{-6}$	-	-
	1	1	3	3	13	$-10.8 \cdot 10^{-3}$	$-3.9 \cdot 10^{-6}$	$-3.9 \cdot 10^{-6}$	$-3.9 \cdot 10^{-6}$	-	-	$3.8 \cdot 10^{-8}$	-	-

Table B.3: *Modelling coefficients of the HR1-VTI vertical transversely isotropic sample. S^{drs}_{ijkl} denotes the compliance in the reference state and is not dependent on the stress. K^{α}_{iikl} is the coefficient of a linear function related to the deformation of the stiff porosity. B_{ik} and F_c are the coefficients of exponential function of the stress and represent the deformation of compliant pore space, see equations set 2.52. The residuum is calculated using the least square method.*

Appendix C

Stress-velocities Figures under triaxial loading, complete loading path

In this Appendix are shown results of all triaxial measurements. The measured velocities and deformation are represented as a function of the stress. The description of the data sets is provided in section 7.

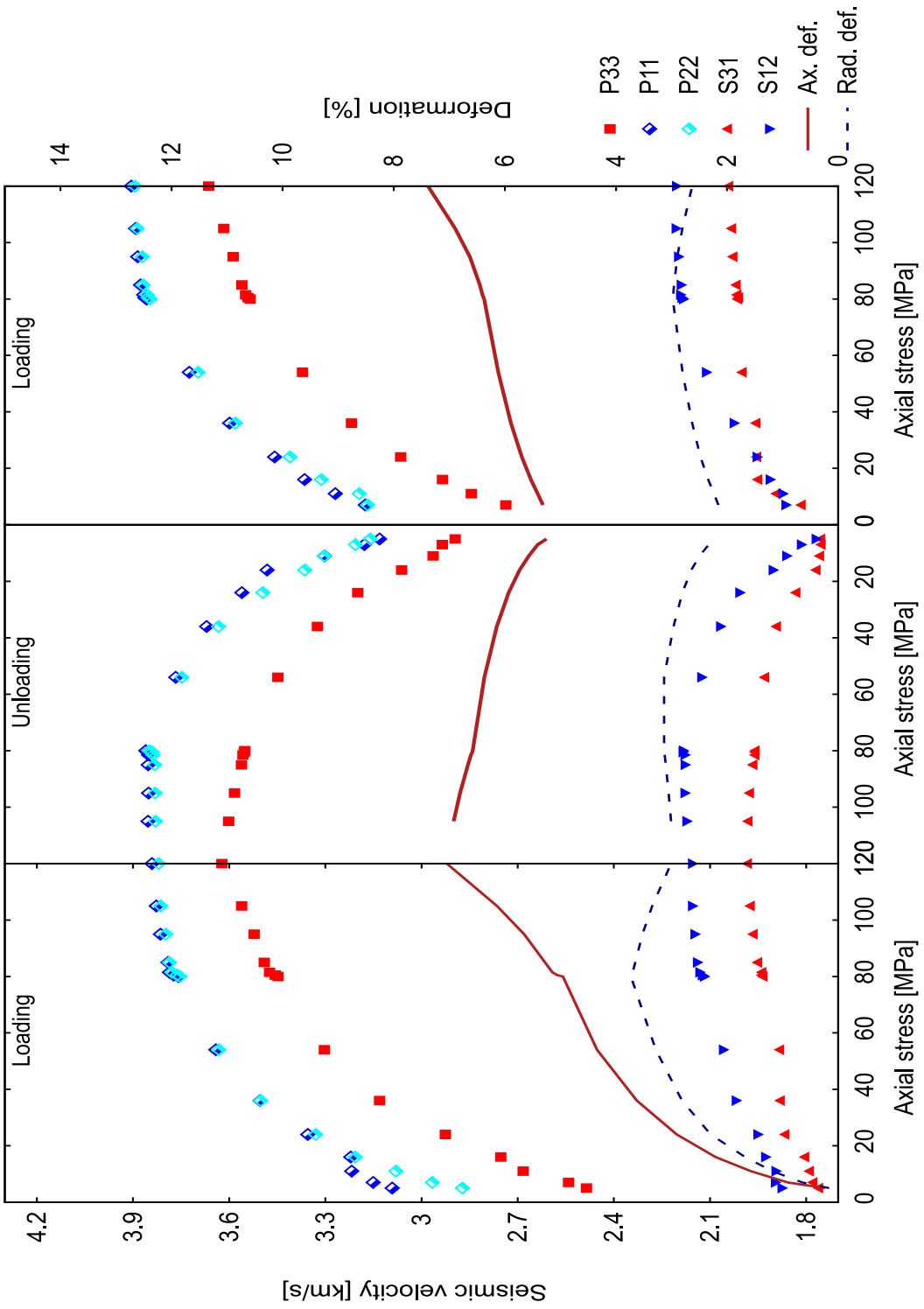

Figure C.1: *SPS-VTI sample, combined graphic of seismic velocities over 6 loading phases. Velocities have following indication: red squares – P-axial; light blue and dark blue diamonds – P-radial in two mutually orthogonal directions; red triangles – S-axial; blue triangles – S-radial with polarization parallel to the bedding. Red solid line denotes measured axial deformations. Blue dashed line displays estimated radial deformations.*

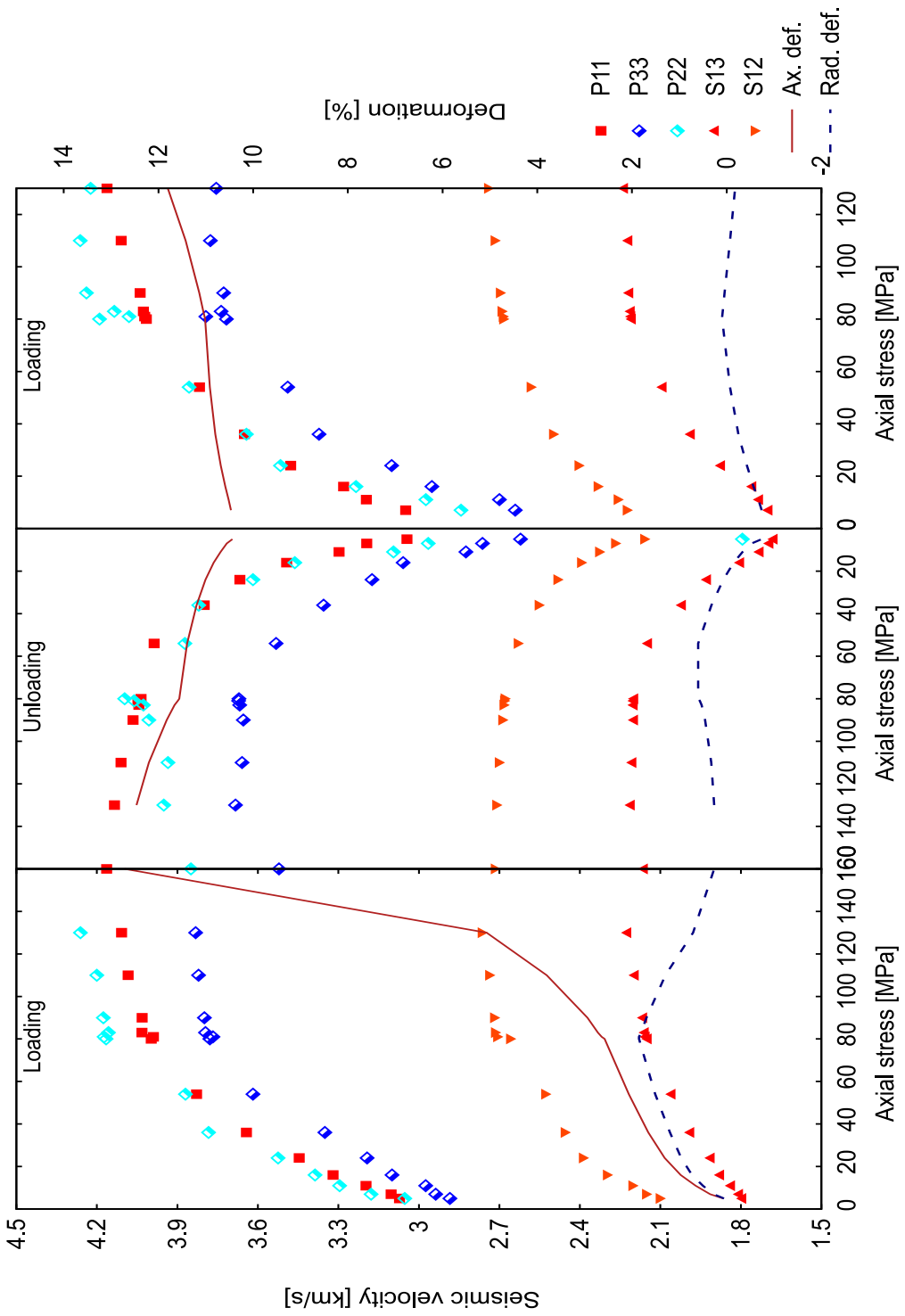

Figure C.2: *SPS-HTI-1 sample, combined graphic of seismic velocities over 6 loading phases. Notation of velocities: red squares – P-axial; light blue and dark blue diamonds – P-radial in parallel and perpendicular to the layering directions correspondingly; red triangles – S-axial with polarization perpendicular to the bedding; orange triangles – S-axial with polarization parallel to the bedding. Red solid line denotes measured axial deformations. Blue dashed line displays estimated radial deformations.*

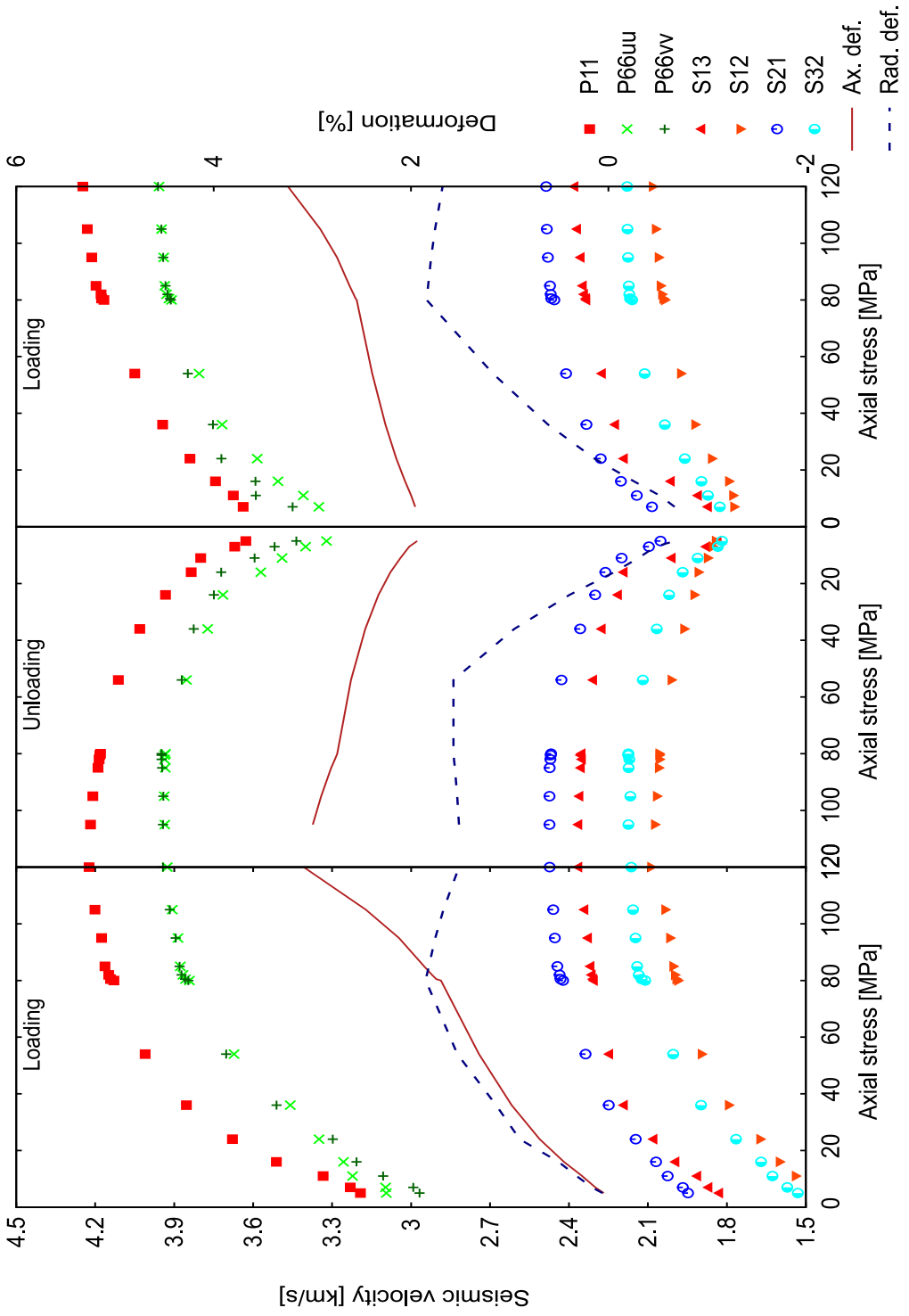

Figure C.3: *SPS-HTI-2 sample, combined graphic of seismic velocities over 6 loading phases. Velocities notation: red squares – P-axial; light green and dark green crosses – P-radial under* $45°$ *to both vertical symmetry planes (exactly in between of them); red triangles – S-axial with polarization perpendicular to the bedding; blue open circles – S-radial with polarization parallel to the bedding. Red solid line denotes measured axial deformations. Blue dashed line displays estimated radial deformations.*

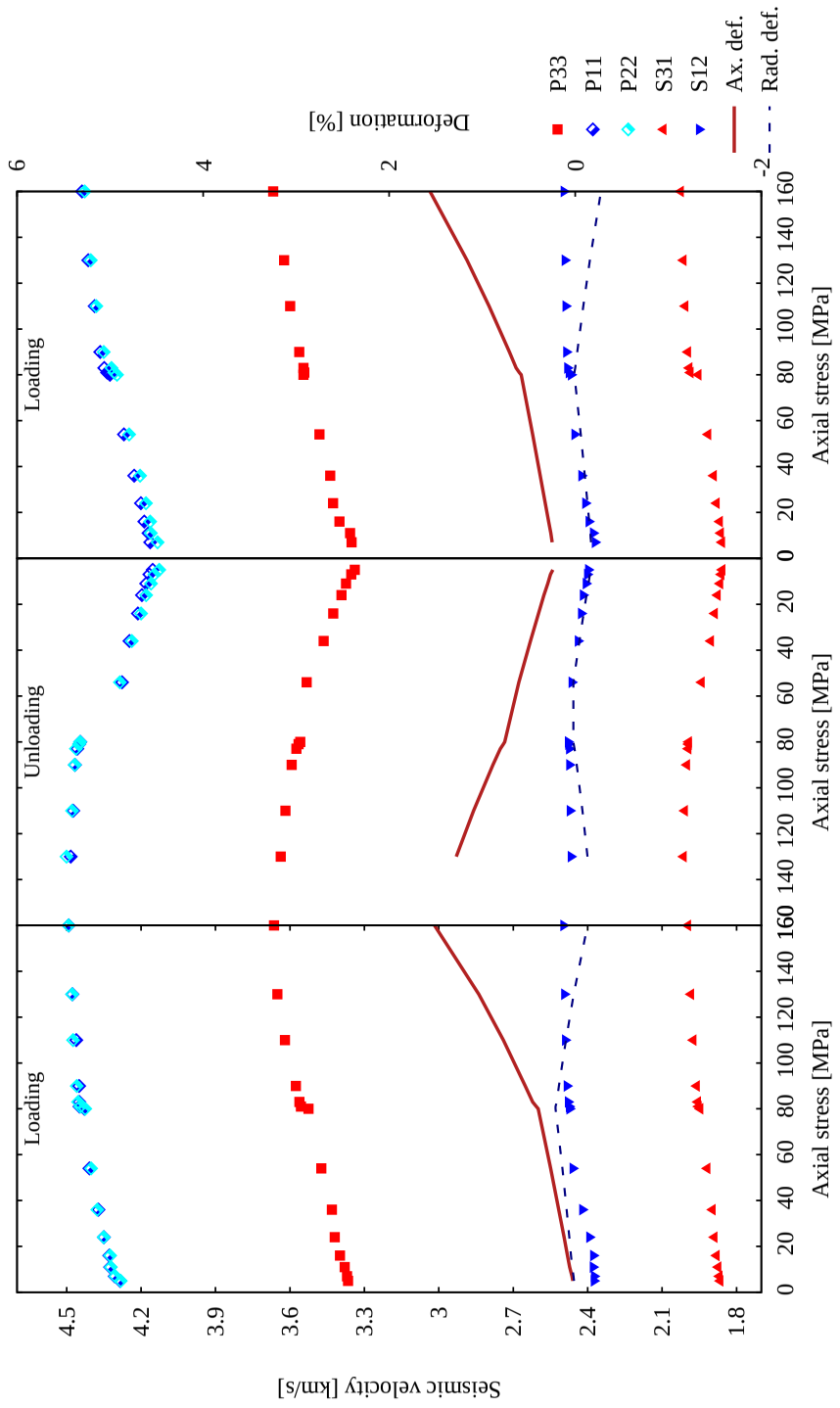

Figure C.4: *HR1-VTI sample, combined graphic of seismic velocities over 6 loading phases. Velocities notation: red dots – P axial, light blue and dark blue dots – P radial in two mutually orthogonal directions, red triangles – S axial, blue triangles – S radial with polarization parallel to the bedding. Red solid line denotes measured axial deformations. Blue dashed line displays estimated radial deformations.*

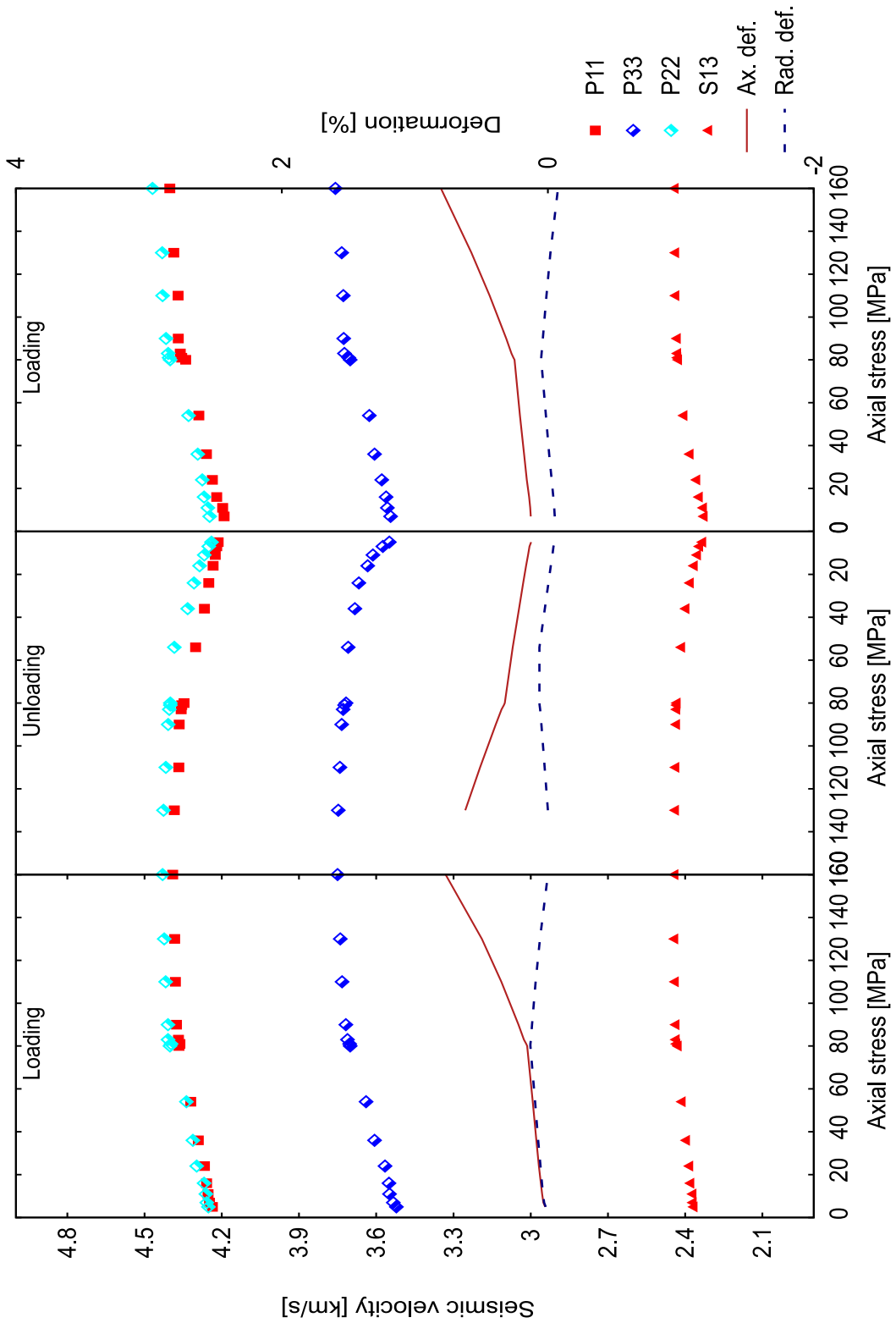

Figure C.5: *HR1-HTI-1 sample, combined graphic of seismic velocities over 6 loading phases. Notation of velocities: red squares – P-axial; light blue and dark blue diamonds – P-radial in parallel and perpendicular to the layering directions correspondingly; red triangles – S-axial with polarization perpendicular to the bedding. Red solid line denotes measured axial deformations. Blue dashed line displays estimated radial deformations.*

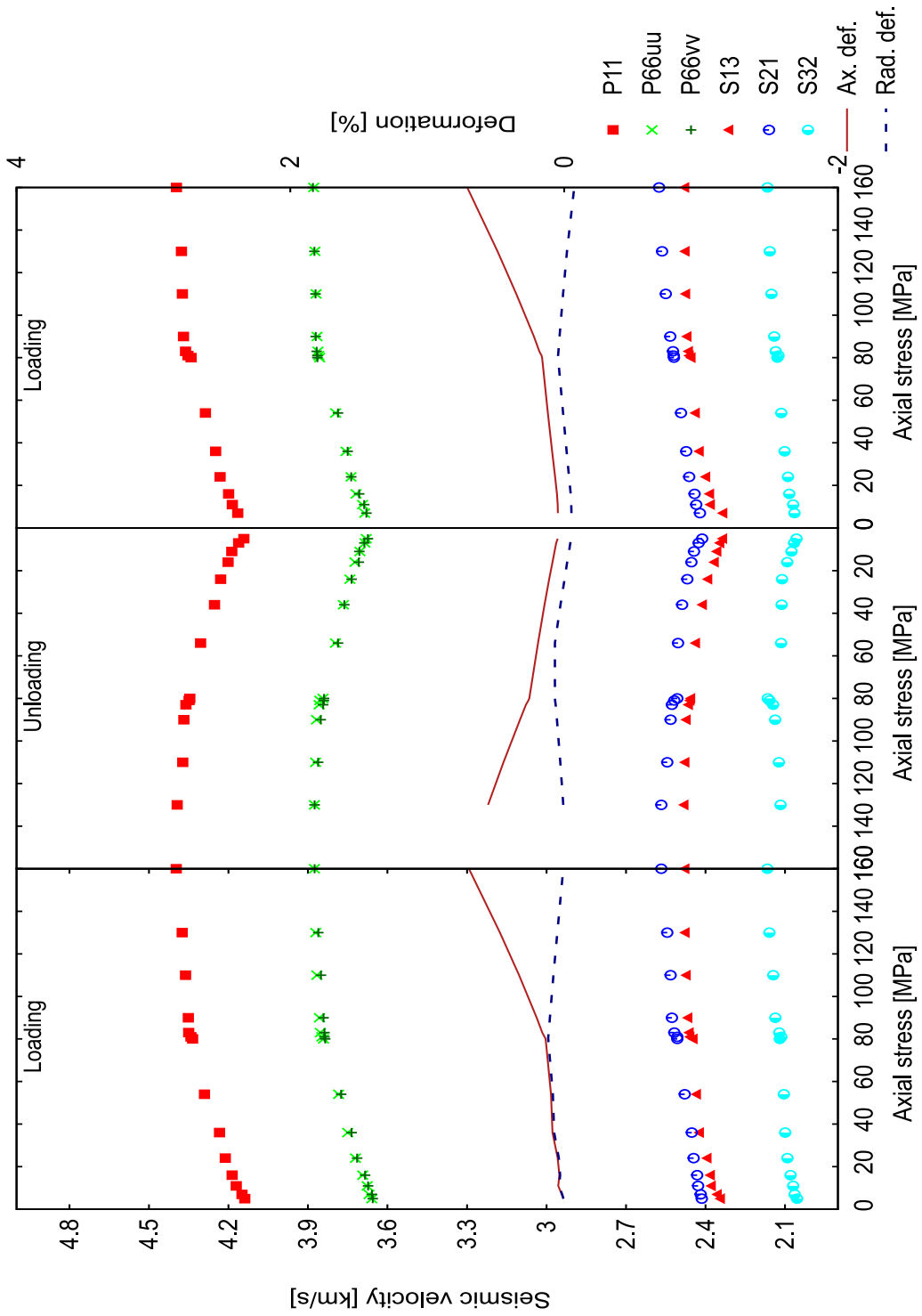

Figure C.6: *HR1-HTI-2 sample, combined graphic of seismic velocities over 6 loading phases. Velocities notation: red squares – P-axial; light green and dark green crosses – P-radial under* 45° *to both vertical symmetry planes (exactly in between of them); red triangles – S-axial with polarization perpendicular to the bedding; blue open circles – S-radial with polarization parallel to the bedding; cyan half-open circles – S-radial with polarization perpendicular to the bedding. Red solid line denotes measured axial deformations. Blue dashed line displays estimated radial deformations.*

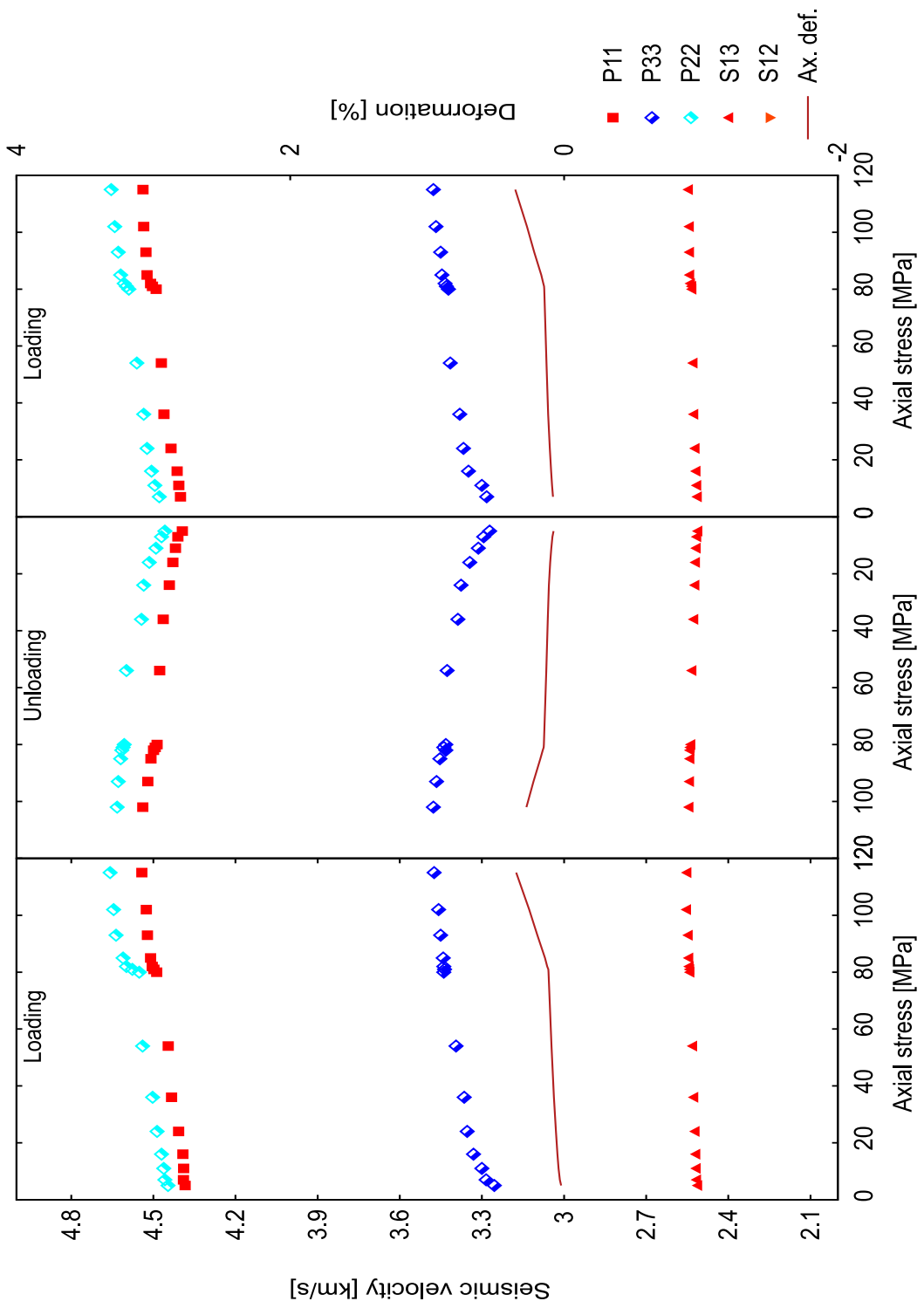

Figure C.7: *Sample FB1-HTI-1. Notation of velocities: red squares – P-axial; light blue and dark blue diamonds – P-radial in parallel and perpendicular to the layering directions correspondingly; red triangles – S-axial with polarization perpendicular to the bedding. Red solid line denotes measured axial deformations.*

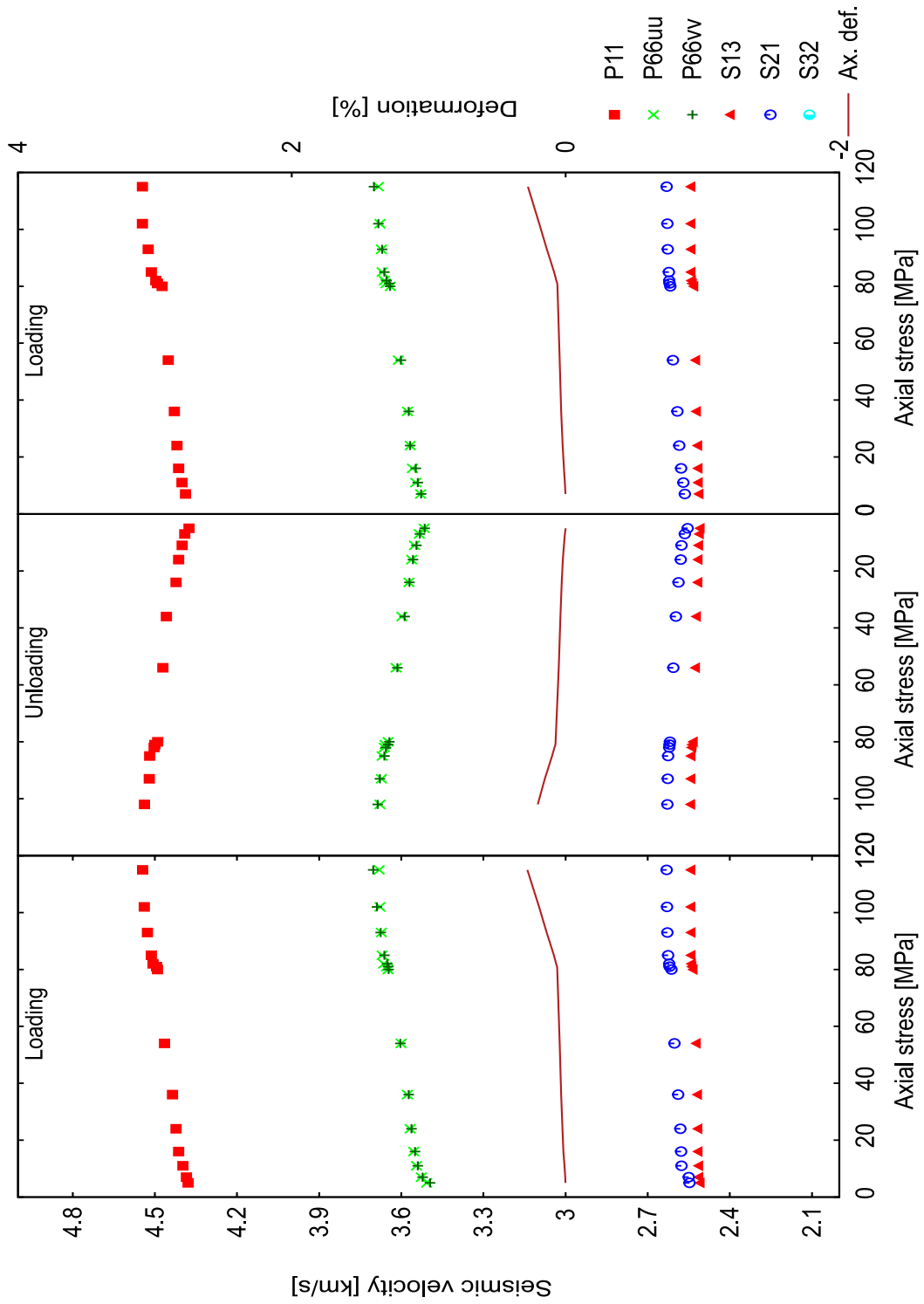

Figure C.8: *FB1-HTI-2 sample. Velocities notation: red squares – P-axial; light green and dark green crosses – P-radial under* $45°$ *to both vertical symmetry planes (exactly in between of them); red triangles – S-axial with polarization perpendicular to the bedding; blue open circles – S-radial with polarization parallel to the bedding; cyan half-open circles – S-radial with polarization perpendicular to the bedding. Red solid line denotes measured axial deformations.*

Bibliography

Abell, B. C., Shao, S., and Pyrak-Nolte, L. J. (2014). Measurements of elastic constants in anisotropic mediaelastic constants in anisotropic media. *Geophysics*, 79(5):D349–D362.

Alkhalifah, T. and Tsvankin, I. (1995). Velocity analysis for transversely isotropic media. *Geophysics*, 60(5):1550–1566.

Arenberg, D. L. (1950). Determination of elastic constants in single crystals with especial reference to silver chloride. *Journal of Applied Physics*, 21(9):941–942.

Asaka, M., Sekine, T., and Furuya, K. (2016). Geologic cause of seismic anisotropy: A case study from offshore western australia. *The Leading Edge*, 35(8):662–668.

Auld, B. (1990). *Acoustic fields and waves in solids.* Robert E. Krieger Publ. Co.

Biot, M. A. (1962). Mechanics of deformation and acoustic propagation in porous media. *Journal of applied physics*, 33(4):1482–1498.

Brown, R. J. and Korringa, J. (1975). On the dependence of the elastic properties of a porous rock on the compressibility of the pore fluid. *Geophysics*, 40(4):608–616.

Brugger, K. (1964). Thermodynamic definition of higher order elastic coefficients. *Physical Review*, 133(6A):A1611.

Cadeville, M. and Morán-López, J. L. (1987). Magnetism and spatial order in transition metal alloys: Experimental and theoretical aspects. *Physics Reports*, 153(6):331–399.

Calvert, R. (2005). *Insights and methods for 4D reservoir monitoring and characterization*, volume 8.

Carcione, J. M. and Tinivella, U. (2001). The seismic response to overpressure: a modelling study based on laboratory, well and seismic data. *Geophysical Prospecting*, 49(5):523–539.

Cheadle, S. P., Brown, R. J., and Lawton, D. C. (1991). Orthorhombic anisotropy: A physical seismic modeling study. *Geophysics*, 56(10):1603–1613.

Ciz, R. and Shapiro, S. A. (2008). Stress-dependent anisotropy in transversely isotropic rocks: Comparison between theory and laboratory experiment on shale. *Geophysics*, 74(1):D7–D12.

Collet, O., Gurevich, B., Madadi, M., and Pervukhina, M. (2014). Modeling elastic anisotropy resulting from the application of triaxial stress. *Geophysics*, 79(5):C135–C145.

Curie, P. (1894). Sur la symétrie dans les phénomènes physiques, symétrie d'un champ électrique et d'un champ magnétique. *Journal de physique théorique et appliquée*, 3(1):393–415.

David, E. and Zimmerman, R. W. (2012). Pore structure model for elastic wave velocities in fluid-saturated sandstones. *Journal of Geophysical Research: Solid Earth*, 117(B7).

Dellinger, J. and Vernik, L. (1994). Do traveltimes in pulse-transmission experiments yield anisotropic group or phase velocities? *Geophysics*, 59(11):1774–1779.

Dewhurst, D. N. and Siggins, A. F. (2006). Impact of fabric, microcracks and stress field on shale anisotropy. *Geophysical Journal International*, 165(1):135–148.

Eaton, B. A. et al. (1975). The equation for geopressure prediction from well logs. In *Fall meeting of the Society of Petroleum Engineers of AIME*. Society of Petroleum Engineers.

Eberhart-Phillips, D., Han, D.-H., and Zoback, M. D. (1989). Empirical relationships among seismic velocity, effective pressure, porosity, and clay content in sandstone. *Geophysics*, 54(1):82–89.

Every, A. and Sachse, W. (1990). Determination of the elastic constants of anisotropic solids from acoustic-wave group-velocity measurements. *Physical Review B*, 42(13):8196.

Fomel, S. (2004). On anelliptic approximations for qp velocities in vti media. *Geophysical Prospecting*, 52(3):247–259.

Freund, D. (1992). Ultrasonic compressional and shear velocities in dry clastic rocks as a function of porosity, clay content, and confining pressure. *Geophysical Journal International*, 108(1):125–135.

Green, R. E. (1973). *Ultrasonic investigation of mechanical properties*, volume 3. Academic Press.

Gurevich, B. (2004). A simple derivation of the effective stress coefficient for seismic velocities in porous rocks. *Geophysics*, 69(2):393–397.

Gurevich, B., Pervukhina, M., and Makarynska, D. (2011). An analytic model for the stress-induced anisotropy of dry rocks. *Geophysics*, 76(3):WA125–WA133.

Helbig, K. (1994). Handbook of geophysical exploration 22.

Helbig, K. and Rasolofosaon, P. N. (2001). A theoretical paradigm for describing hysteresis and nonlinear elasticity in arbitrary anisotropic rocks. *Anisotropy 2000: Fractures, Converted Waves and Case Studies*, pages 383–398.

Herwanger, J. V. and Horne, S. A. (2009). Linking reservoir geomechanics and time-lapse seismics: Predicting anisotropic velocity changes and seismic attributes. *Geophysics*, 74(4):W13–W33.

Heslop, D., McIntosh, G., and Dekkers, M. (2004). Using time-and temperature-dependent preisach models to investigate the limitations of modelling isothermal remanent magnetization acquisition curves with cumulative log gaussian functions. *Geophysical Journal International*, 157(1):55–63.

Hornby, B. E. (1998). Experimental laboratory determination of the dynamic elastic properties of wet, drained shales. *Journal of Geophysical Research: Solid Earth*, 103(B12):29945–29964.

Horne, S. (2013). A statistical review of mudrock elastic anisotropy. *Geophysical Prospecting*, 61(4):817–826.

Jaeger, J. and Cook, N. (1969). Fundamentals of rock mechanics: London, methuen and co.

Jones, L. E. and Wang, H. F. (1981). Ultrasonic velocities in cretaceous shales from the williston basin. *Geophysics*, 46(3):288–297.

Kalidindi, S. R. and Franco, E. (1997). Numerical evaluation of isostrain and weighted-average models for elastic moduli of three-dimensional composites. *Composites Science and Technology*, 57(3):293–305.

Kaselow, A. (2004). *The Stress Sensitivity Approach: Theory and Application*. Freie Universitaet Berlin.

Kreja, I. (2011). A literature review on computational models for laminated composite and sandwich panels. *Central European Journal of Engineering*, 1(1):59–80.

Landau, L. D. and Lifshitz, E. M. (1987). *Theory of Elasticity (in Russian)*. Nauka, Glavnaja Redaktsija Phys.-Math. Lit., Moscow.

Landrø, M., Digranes, P., and Strønen, L. (2001). Mapping reservoir pressure and saturation changes using seismic methods-possibilities and limitations. *First break*, 19(12):671–684.

Mavko, G., Mukerji, T., and Dvorkin, J. (2009). *The rock physics handbook: Tools for seismic analysis of porous media*. Cambridge university press.

Mavko, G., Mukerji, T., and Godfrey, N. (1995). Predicting stress-induced velocity anisotropy in rocks. *Geophysics*, 60(4):1081–1087.

Mayr, S., Niemann, R., and Shapiro, S. (2016). Understanding of elastic anisotropy of shale under triaxial loading: Porosity-deformation approach. *GEOPHYSICS*, 81(5):C163–C175.

Mayr, S. I. and Burkhardt, H. (2006). Ultrasonic properties of sedimentary rocks: Effect of pressure, saturation, frequency and microcracks. *Geophysical Journal International*, 164(1):246–258.

Mises, R. v. (1913). Mechanik der festen Körper im plastisch- deformablen Zustand. *Nachrichten von der Gesellschaft der Wissenschaften zu Göttingen, Mathematisch-Physikalische Klasse*, 1913:582–592.

Mohazzabi, P. (1997). Archimedes' principle revisited. *Journal of Applied Mathematics and Physics*, 5(04):836.

Muir, F. and Dellinger, J. (1985). A practical anisotropic system. *SEP-44*, 55:58.

Neighbours, J. and Smith, C. S. (1950). An approximation method for the determination of the elastic constants of cubic single crystals. *Journal of Applied Physics*, 21(12):1338–1339.

Nettles, T. (1994). Basic mechanics of laminated plates nasa reference publication 1351. *USA: MSFC, Alabama*.

Norris, A. N., Sinha, B. K., and Kostek, S. (1994). Acoustoelasticity of solid/fluid composite systems. *Geophysical Journal International*, 118(2):439–446.

Pervukhina, M., Gurevich, B., Golodoniuc, P., and Dewhurst, D. N. (2011). Parameterization of elastic stress sensitivity in shales. *Geophysics*, 76(3):WA147–WA155.

Prasad, M. and Manghnani, M. H. (1997). Effects of pore and differential pressure on compressional wave velocity and quality factor in berea and michigan sandstones. *Geophysics*, 62(4):1163–1176.

Preisach, F. (1935). Über die magnetische nachwirkung. *Zeitschrift für physik*, 94(5-6):277–302.

Pride, S. R., Berryman, J. G., Commer, M., Nakagawa, S., Newman, G. A., and Vasco, D. W. (2017). Changes in geophysical properties caused by fluid injection into porous rocks: analytical models. *Geophysical Prospecting*, 65(3):766–790.

Prioul, R., Bakulin, A., and Bakulin, V. (2004). Nonlinear rock physics model for estimation of 3d subsurface stress in anisotropic formations: Theory and laboratory verification. *Geophysics*, 69(2):415–425.

Rasolofosaon, P. (1998). Stress-induced seismic anisotropy revisited. *Revue de l'Institut Français du pétrole*, 53(5):679–692.

Rasolofosaon, P. N. (2010). Generalized anisotropy parameters and approximations of attenuations and velocities in viscoelastic media of arbitrary anisotropy type–theoretical and experimental aspects. *Geophysical Prospecting*, 58(4):637–655.

Rasolofosaon, P. N. (2011). Toward phenomenological universality of the mechanical behavior of arbitrarily anisotropic porous rocks. *Geophysics*, 76(3):WA167–WA183.

Rasolofosaon, P. N. and Yin, H. (1996). Simultaneous characterization of anisotropy and nonlinearity in arbitrary elastic media-reflections on experimental data. In *Seismic anisotropy*, pages 141–179. Society of Exploration Geophysicists.

Ryan-Grigor, S. (1998). *Empirical relationships between anellipticity and Vp/Vs in shales: Potential applications toAVO studies and anisotropic seismic processing*. SEG Expanded Abstracts, Schlumberger Cambridge Research.

Sarout, J., Delle Piane, C., Nadri, D., Esteban, L., and Dewhurst, D. N. (2015). A robust experimental determination of thomsen's δ parameterrobust experimental determination of δ. *Geophysics*, 80(1):A19–A24.

Sarout, J., Molez, L., Guéguen, Y., and Hoteit, N. (2007). Shale dynamic properties and anisotropy under triaxial loading: Experimental and theoretical investigations. *Physics and Chemistry of the Earth, Parts A/B/C*, 32(8-14):896–906.

Sayers, C. M. (1999). Stress-dependent seismic anisotropy of shales. *Geophysics*, 64(1):93–98.

Sayers, C. M. (2006). Sensitivity of time-lapse seismic to reservoir stress path. *Geophysical Prospecting*, 54(3):369–380.

Shapiro, S. (2017). Stress impact on elastic anisotropy of triclinic porous and fractured rocks. *Journal of Geophysical Research: Solid Earth*, 122(3):2034–2053.

Shapiro, S. A. (2003). Elastic piezosensitivity of porous and fractured rocks. *Geophysics*, 68(2):482–486.

Shapiro, S. A. and Kaselow, A. (2005). Porosity and elastic anisotropy of rocks under tectonic stress and pore-pressure changes. *Geophysics*, 70(5):N27–N38.

Sviridov, V. A., Mayr, S. I., and Shapiro, S. A. (2017). Elastic properties of two vti shale samples as a function of uniaxial stress: Experimental results and application of the porosity-deformation approach. *Geophysics*, 82(6):C201–C210.

Thomsen, L. (1986). Weak elastic anisotropy. *Geophysics*, 51(10):1954–1966.

Truesdell, C. (1965). *Problems of non-linear elasticity*, volume 8. Gordon and Breach.

Tsvankin, I. (1996). P-wave signatures and notation for transversely isotropic media: An overview. *Geophysics*, 61(2):467–483.

Tsvankin, I. (1997). Anisotropic parameters and p-wave velocity for orthorhombic media. *Geophysics*, 62(4):1292–1309.

Verdon, J. P., Angus, D. A., Michael Kendall, J., and Hall, S. A. (2008). The effect of microstructure and nonlinear stress on anisotropic seismic velocities. *Geophysics*, 73(4):D41–D51.

Vernik, L. and Liu, X. (1997). Velocity anisotropy in shales: A petrophysical study. *Geophysics*, 62(2):521–532.

Vernik, L. and Nur, A. (1992). Ultrasonic velocity and anisotropy of hydrocarbon source rocks. *Geophysics*, 57(5):727–735.

Walsh, J. (1965a). The effect of cracks on the compressibility of rock. *Journal of Geophysical Research*, 70(2):381–389.

Walsh, J. (1965b). The effect of cracks on the uniaxial elastic compression of rocks. *Journal of Geophysical Research*, 70(2):399–411.

Wang, Z. (2002a). Seismic anisotropy in sedimentary rocks, part 1: A single-plug laboratory method. *Geophysics*, 67(5):1415–1422.

Wang, Z. (2002b). Seismic anisotropy in sedimentary rocks, part 2: Laboratory data. *Geophysics*, 67(5):1423–1440.

Winkler, K. W. and McGowan, L. (2004). Nonlinear acoustoelastic constants of dry and saturated rocks. *Journal of Geophysical Research: Solid Earth*, 109(B10).

Winterstein, D. and Paulsson, B. (1990). Velocity anisotropy in shale determined from crosshole seismic and vertical seismic profile data. *Geophysics*, 55(4):470–479.

Wolfe, J. P. (2005). *Imaging phonons: acoustic wave propagation in solids*. Cambridge University Press.

Curriculum Vitae

For reasons of data protection, the curriculum vitae is not published in the electronic version.

List of publications

Journal publications

- Sviridov V. A., Mayr S. I. and Shapiro S. A. (2018). Rock elasticity as a function of the uniaxial stress: laboratory measurements and theoretical modelling of vertical transversely isotropic and orthorhombic shales. Geophysical Prospecting (under review).
- Sviridov V. A., Mayr S. I. and Shapiro S. A. (2017). Elastic properties of two VTI shale samples as a function of uniaxial stress: experimental results and application of porosity deformation approach. Geophysics, 82, C201-C210.

Extended abstracts

- Mayr S.I. Sviridov V. A. and Shapiro S. A. (2017). Some Constrains for Velocity Prediction by Means of the Porosity Deformation Approach. Conference: 79th EAGE Conference and Exhibition 2017
- Mayr S.I., Sviridov V.A., and Shapiro S.A. (2017). Uniaxial Stress vs Elastic Properties. Experimental Measurements and Theoretical Predictions for three VTI and one HTI Samples. In DGMK/ÖGEW-Frühjahrstagung, " Perspektiven für Erdöl und Erdgas - Sicher und innovativ aus Deutschland", Celle, 5./6. April 2017, DGMK-Tagungsbericht 2017-1, ISBN 978-3-941721-73-9, pages 1–7.
- Sviridov V., Mayr S.I., and Shapiro S.A. (2016). Elastic properties of VTI and HTI shale samples as a function of stress: Laboratory measurements versus theoretical modeling. In SEG Technical Program Expanded Abstracts 2016, pages 3184–3189. doi: 10.1190/segam2016- 13857145.1. URL http://library.seg.org/doi/abs/10.1190/segam2016-13857145.1. SEG Conference in Dallas.
- Sviridov V. A., Mayr S. I. and Shapiro S. A. (2016) The Influence of Uniaxial Stress Conditions on the Elastic Properties of Vertical Transversely Isotropic Shale Fifth EAGE Shale Workshop in Catania, Italy. 2-4 May 2016
- Sviridov V., Mayr S.I., and Shapiro S.A. (2016). Stress dependency of elastic parameters in shales with different symmetries. VTI versus orthorhombic elastic medium. In DGMK/ÖGEW-Frühjahrstagung, "Digitalisierung der Öl-und Gasindustrie", Celle, 21./22. April 2016, DGMK-Tagungsbericht 2016-1, ISBN 978-3-941721-64-7, pages 1–7. [6]
- Sviridov V. A., Mayr S. I. and Shapiro S. A. (2016). Elastic properties of VTI and HTI shale samples as a function of stress: Laboratory measurements versus theoretical modeling. SEG Technical Program Expanded Abstracts 2016: pp. 3184-3189. doi: 10.1190/segam2016-13857145.1
- Sviridov V. A., Mayr S. I. and Shapiro S. A. (2015). Comparison of experimentally determined and theoretically predicted elastic properties of VTI shale under uniaxial loading, 75. Jahrestagung der Deutschen Geophysikalischen Gesellschaft, 96
- Mayr S.I., Sviridov V.A., and Shapiro S.A. (2014). Comparison of p- and s-wave velocities in a transversal isotropic sandstone and a shale under uniaxial loading conditions, 76th EAGE Conference & Exhibition 2014, Amsterdam RAI, The Netherlands, 16-19 June 2014, extended Abstract No. 21204, 1-5